134
24

The Effect of a Fillet on a Wing/Body Junction Flow

by

Michael B. Dewitz

Thesis submitted to the Faculty of the

Virginia Polytechnic Institute and State University

in partial fulfillment of the requirements for the degree of

Master of Science

in

Aerospace Engineering

APPROVED:

Roger L. Simpson, Chairman

Dana Walker

William J. Devenport

December, 1988

Blacksburg, Virginia

LD
5655
V855
1988

D493
c.2

The Effect of a Fillet on a Wing/Body Junction Flow

by

Michael B. Dewitz

Roger L. Simpson, Chairman

Aerospace Engineering

(ABSTRACT)

Time-averaged properties of a wing-body-junction flow surrounding a cylindrical wing with a 1.5:1 elliptical nose and a NACA 0020 tail have been compared to those for the above wing with a 1.5 inch radius fillet normal to the wing's surface. An attempt was made to determine the effectiveness of the fillet in improving the uniformity of the wing-body junction flow downstream of the wing, and in attenuating the junction vortex. Measurements included oil-flow visualizations and surface-static-pressure measurements of the flat test floor surrounding the wings, and hot-wire anemometer measurements made in the flow downstream of the wing. Calculations of the drag and the volumetric entrainment of free-stream fluid due to the presence of the baseline wing and wing with fillet were performed. The results of these calculations are important criteria used to determine the effectiveness of the fillet as a flow control device.

Results show that the vortex is present in each case, and its size is slightly larger for the wing with fillet as compared to the baseline wing. For each test case, the drag and volumetric entrainment of free-stream fluid were the nearly same for the wing with fillet as compared to the baseline wing. It was also found that increases in the boundary-layer thickness cause only small increases in the

size of the junction vortex. The 1.5 inch radius fillet does not appear to be a viable flow control device.

Acknowledgements

The author would like to thank his advisor, Dr. Roger L. Simpson, for the opportunity to work under his guidance. He would also like to thank Dr. William J. Devenport for his constant support and patience. The author has learned a great deal about the world of experimental aerodynamics from Dr. Devenport. He would also like to thank Dr. Dana Walker for serving on his committee.

He wishes to thank all the graduate students at VPI&SU who have helped with this research in any way.

Finally, a very special thanks to his wife, Kerri, for her constant support and patience throughout the past few hectic months.

This study was supported by the Office of Naval Research under contract no. N00014-88-C-0291.

Table of Contents

List of Illustrations

List of Tables

List of Symbols

A .....coefficient describing offset in King's Law

B.....coefficient describing slope in King's Law

b .....span of the wing

c.....chord of the wing

C_d .....drag coefficient

C_f.....skin-friction coefficient

C_p .....pressure coefficient

E.....voltage

F_d.....force due to drag

H .....height of control volume

$\dot{m}$ .....mass flow

$\dot{m}_{turb}$ ..... mass flow of turbulent fluid

$\dot{m}_e$ ..... entrainment of turbulent fluid

n .....exponent in King's Law

p .....surface static pressure

P_o .....local total pressure

P_∞ .....free-stream static pressure

$P_{o\infty}$ .....free-stream total pressure

Re_θ.....Reynolds number based on momentum thickness

Re_x.....Reynolds number based on streamwise location

t.....temperature in degrees Centigrade

T.....wing thickness

U .....local mean velocity

U_e .....velocity at the edge of the boundary layer

U_∞.....free-stream velocity at reference pitot static

u^*.....friction velocity

$\overline{u'^2}$.....square of longitudinal velocity fluctuation

W .....width of the control volume used in drag and entrainment calculations

Greek Symbols

δ .....boundary-layer thickness defined where $U/U_e = 0.99$

δ^*.....displacement thickness

ν .....kinematic viscosity

ρ .....density

θ .....momentum thickness

I. Introduction

A wing-body-junction flow is formed whenever a boundary layer on a surface comes upon some strut that projects from that surface. The presence of the strut causes the spanwise vorticity present in the oncoming boundary layer to turn about the leading edge of the strut. Thus, a horseshoe vortex with its legs directed in the streamwise direction is created, much like in Figure 1. Each of the legs of the vortex rotates in opposite directions, so the net zero average streamwise vorticity is preserved for the flow about a symmetric strut at zero degrees angle of attack. This type of flow occurs in many real world situations such as the junction of an airplane wing with the fuselage, turbine blades with the rotor hub, and the sail of a submarine with the hull.

As the flow nears the strut, normally some type of airfoil, it encounters a strong adverse streamwise pressure gradient that further complicates the flow. This pressure gradient produces a separation region with backflow near the centerline of the flow ahead of the leading edge. The flow around the strut

experiences an acceleration due to a favorable streamwise pressure gradient up to the maximum thickness of the strut. This is followed downstream of the maximum thickness by deceleration and possible separation due to an adverse streamwise pressure gradient. The horseshoe vortex is by no means a steady phenomena. The vortex is turbulent and is characterized by intense bistable unsteadiness that originates upstream of the leading edge, as described by Devenport and Simpson (1987c). In one mode, there are high backflow velocities near the test floor. In the other mode, the velocities near the test floor are small. The presence of the vortex is presumed to cause pressure fluctuations on the surface that the strut projects from, as well as increase the magnitude of the drag due to the strut.

Much research has been performed detailing the flow around various struts. Shabaka and Bradshaw (1981) have perfomed turbulence measurements in front of and next to a 3:1 semi-elliptical nose with a constant thickness tail. Devenport and Simpson (1986, 1987a,b,c) have performed extensive tests on the wing used in this paper. They have done surface-oil-flow visualizations, hot-wire anemometer measurements, and laser-doppler anemometer measurements in order to detail the time-mean characteristics of the flow, and to capture the time dependent features of the reversing flow regions. In these works, the presence of the junction vortex is well documented.

Mehta (1984) presented hot-wire anemometer measurements 175 millimeters downstream of a strut to determine that the leading edge of the strut has a

significant effect on the size and strength of the vortex. He used three struts with different leading edges. The three nose shapes were determined by the equation

$$(\frac{x}{a'})^m + (\frac{z}{b'})^m = 1 \qquad (1)$$

with m equal to 1.5, 2.0, and 3.0. He related the depth that the velocity contours are drawn into the boundary layer to the strength of the junction vortex. He determined that the strength of the vortex increases as the bluntness of the leading edge increases, as defined above. He also found that the circulation increases with increases in bluntness. This is another indication that the vortex increases in strength with increases in bluntness. Finally, he related the size of the vortex to the the area over which the turbulence levels were significantly enhanced. Mehta determined that the size of the vortex also increases as the bluntness of the leading edge increases.

Altering the leading edge of the strut can thus alter the size and strength of the vortex. The addition of a fillet to the wing, which changes the wing leading edge, could then influence the formation of the vortex associated with the traditional wing-body-junction flow. Many benefits would be obtained through dissipating the vortex. Among them would be to reduce the drag, and to alleviate the pressure fluctuations which cause noise. These fluctuations are presumed to be associated with the unsteadiness of the vortex.

Kubendran *et al.* (1988) have done some work with leading edge fillets similar to a wedge placed at the leading edge of the wing. The shapes of the fillets were determined by stretching the cross-sectional area of the wing nose in the

streamwise direction. The wing they used had a NACA 0012 cross-section and a chord, c, of 6 inches. The distance from the leading edge of the wing to the leading edge of the fillet was different for each fillet. In one case it was 0.167c, and in the other it was 0.33c. Their measurements were made with a laminar approach boundary layer which is not the case for the present flow. They used a smoke wire placed at various heights to qualitatively discern the improvements in the flow resulting from the leading edge fillet. They also performed surface pressure measurements on the line of symmetry ahead of the wing, and velocity measurements two chord lengths downstream of the wing leading edge. They found that the leading edge fillet eliminated the leading edge separation, increased the extent of laminar flow around the juncture, and reduced the overall drag.

Pierce *et al.* (1988) compared three types of wing-with-fillet combinations to the wing with no fillet using hot-wire anemometry. They used a tear-drop strut with a chord of 298mm, a span of 229mm, and a maximum thickness of 127mm as their baseline model. The effects of a 0.17c and a 0.0426c radius wrap-around fillet, and an elliptical wrap-around fillet with a major axis of 0.0852c and a minor axis of 0.0426c were studied. They examined the turbulence kinetic energy of the flow upstream of the strut. They found that the turbulence kinetic energy increased for both wing with circular cross-section fillet cases, as compared to the baseline wing.

This report will utilize surface-oil-flow visualization and surface-static pressure measurements of the test floor surrounding the wings to qualitatively

compare the merits of the wing with a 1.5 inch radius fillet to the baseline 1.5:1 elliptic nose, NACA 0020 tail wing. Improvements in the flow are judged by an attenuation of the junction vortex and reduction of the drag, entrainment of free-stream fluid, and non-uniformity of the flow downstream of the wing. Hot-wire measurements of the mean velocity made downstream of the wing were used to calculate the drag and entrainment of free-stream fluid. Measurements of the mean velocity and square of turbulence intensity were used to examine the non-uniformity of the flow.

II. Experimental Apparatus and Techniques

Wind Tunnels

Tests were conducted in both the Virginia Tech Low-Speed Boundary-Layer Tunnel and The Virginia Tech Stability Wind Tunnel. The Stability Wind Tunnel was needed to perform those measurements with the wing models at non-zero angles of attack because the blockage in the Boundary-Layer Tunnel test section would have been too great with the wing at an angle of attack.

The Virginia Tech Low-Speed Boundary-Layer Tunnel is the same facility used in previous work at Southern Methodist University (Simpson *et al.* 1981; Shiloh *et al.* 1981; and Simpson *et al.* 1983). The mainstream flow of this blown open-circuit wind tunnel is introduced into the test section after passing through an air filter, heat exchanger, blower, fixed-setting flow damper, a section of honeycomb to remove the mean swirl of the flow, seven screens to remove much

of the turbulence intensity, and finally through a two-dimensional four-to-one contraction-ratio nozzle to further reduce the longitudinal turbulence intensity while accelerating the flow to test speed. Figure 2 shows the side view schematic of the 8 meter long, 0.91 meter wide, and 0.26 meter high test section. The side walls of the this tunnel have 1/4 inch thick removable plexiglas sections adjacent to the wing. The removal of these sections with a wing model in the test section adds 1/2 inch to the width of the test section in the vicinity of the wing. Thus, the flow displaced by the wing has a wider test section through which to pass. This minimizes the blockage-induced pressure gradient due to the presence of the wing.

The Stability Wind Tunnel at VPI&SU was used in order to perform measurements made with the wings at an angle of attack. The Stability Wind Tunnel has a 6 x 6 x 28 foot test section that is part of a closed circuit tunnel (Figure 3). The air is circulated by a fourteen foot fan powered by a 600 horsepower motor. A low free-stream turbulence level of 0.02%, as measured by Marchman *et al.* (1986) is achieved as the flow passes through seven sets of stainless-steel anti-turbulence screens. The test section is made primarily of 1/8 inch thick steel panels with a plexiglass panel in order to view the experiments. The test section is reinforced with cast iron I-beams spaced approximately every thirty inches.

Wings

The baseline wing was symmetrical, had a maximum thickness of 2.824 inches, a chord of 12 inches, and a span of 9 inches. The cross-section of the wing, which was constant along its span, consisted of a 1.5:1 elliptical nose and a NACA 0020 tail. The baseline wing was manufactured on a numerically-controlled milling machine at VPI&SU. It consisted of twelve 3/4 inch thick aluminum airfoil sections that were mounted together and finished by sanding to the desired coordinates. Three baseline wings were constructed. A 120 grit sandpaper trip 1/4 inch wide was placed 0.6 wing thicknesses downstream of the wing leading edge to ensure an even transition of the boundary layer in the Boundary-Layer Tunnel. The trip was not used in the Stability Wind Tunnel measurements. The effects of the trip on the asymmetric flow with the wings at angle of attack were presumed to be different on either side of the wing, and therefore not easily accounted for.

The fillet was also aluminum and made on a numerically-controlled milling machine. It consisted of a 1.5 inch radius arc normal to the above mentioned wing at all locations, and tangent to the wing at a height of 1.5 inches. The wing/fillet combination was created by removing two of the airfoil sections from one of the baseline wing models and mounting the wing on top of the fillet. The combination is shown in Figure 4.

For measurements made in the Stability Wind Tunnel, a cap was attached to the top of the wing. The addition of the cap served the purpose of more

accurately simulating the flow about a submarine sail tower. The cap was not used in the Boundary-Layer Tunnel due to the height restriction of the test section. The cap was manufactured by turning a body of revolution with the same cross-section as the wing from two blocks attached together along a plane of symmetry. The body of revolution was then separated in the longitudinal direction to form two wing caps. However, this procedure produced caps that did not have the exact same cross-section as the wing. A 1/8 inch plexiglass plate was therefore placed between the cap and the top of the wing. The plexiglass was finished by sanding so that a smooth transition from wing to cap was achieved.

Coordinate Systems and Reference Conditions

The wind-tunnel fixed coordinate system (X,Y,Z), shown in Figure 5, will be used in presenting the hot-wire measurements. X is measured downstream from the wing leading edge, parallel to the chord of the wing at zero degrees angle of attack. Y is measured normal to the test floor, and Z normal to X and Y to form a right-handed system. For the oil-flow visualizations and surface-static pressure measurements, a similar wing-fixed coordinate system (X_1, Y_1, Z_1) was used in which X_1 and Z_1 rotate with the wing. This coordinate system is shown in Figure 6.

In the Boundary-Layer Tunnel, the free-stream velocity, U_∞, and the free-stream total and static pressures, $P_{o\infty}$ and P_∞ , were measured by a

pitot-static tube located at X/T=-9.2 and Z/T=3.54. In the Stability Wind Tunnel, these same reference conditions were measured by a pitot-static tube located at X/T=-2 and Z/T=8.64.

Test Conditions

In the Boundary-Layer Tunnel, measurements were conducted with an approach boundary layer of both 1.4 and 0.695 inches thick measured at X/T=-2.15. The free-stream velocity for the thick boundary layer was 27 m/s with a nominal Re_θ of 6700. The nominal free-stream velocity for the thin boundary layer was 32.5 m/s with a nominal Re_θ of 4500. In the Stability Wind Tunnel, tests were conducted with flow conditions nearly the same as the Re_θ=4500 case in the Boundary-Layer Tunnel. Throughout this paper, these different flow conditions will be referred to as the thick and thin approach boundary-layer conditions.

"False Floors"

In order to achieve the thin-boundary layer condition, it was necessary to design a "false floor" for the Boundary-Layer and Stability Wind Tunnels, i.e. a flat plate outside the wind tunnel boundary layer to produce a new boundary

layer. The leading edge of the "false floor" was at X/T=-16.29. This distance resulted from using a relationship in Schetz (1984), p. 178, eq. 7-44, where

$$\frac{\delta}{x} = \frac{0.375}{Re_x^{(1/5)}} \tag{2}$$

and a desired boundary-layer thickness at X/T=-2.15 of 0.67 inches.

In the Boundary-Layer Tunnel, the "false floor" consisted of 4 sections of 3/4 inch thick "finform" plywood. The "false floor" rested on 0.01651 meter high aluminum channel. A sketch of the configuration is shown in Figure 7. A 3 inch wide, 1/4 inch thick aluminum strip was mounted to the "finform" plywood, and formed the leading edge of the "false floor". The leading edge of the aluminum was rounded to avoid separation. A 1/4 inch wide 120 grit sandpaper trip that spanned the wind tunnel was placed at X/T=-15.23 to ensure boundary-layer transition. A 6 inch wide slot was cut in the original test floor that spanned the wind tunnel. This formed an exit for the boundary layer upstream of the slot. The edges of the slot were at X/T=-17.35 and X/T=-15.23. A strip of 1/32 inch thick aluminum that spanned the test section was attached to the underside of the "false floor" leading edge. Another 1/32 inch thick strip was attached to the upstream edge of the slot. The two aluminum sheets were then curved so that a channel was formed to induce the boundary layer upstream of the slot to exit the wind tunnel. A new boundary layer was then formed on the leading edge of the "false floor".

The wing was mounted on a circular aluminum plate which in turn was clamped to a 25 inch square plate. This configuration was then mounted to the

"finform" plywood. The position of the wings in the tunnel were fixed from below through the use of metal dowel pins. The alignment of the wings for the case with a thick approach boundary layer was also determined through the use of the metal dowel pins. For the thick boundary-layer case, the wing was mounted to a rectangular plexiglas plate which was then mounted to the original test floor.

Several tests were conducted in order to establish the quality of the flow after the installation of the "false floor". A spanwise traverse of a Preston tube at X/T = -7.52 was made. This measures the total pressure near the test floor, and is directly related to the skin friction on the floor. The skin friction is highly sensitive to variations in velocity near the surface, and is therefore a good indication of the spanwise uniformity of the flow. The pressure coefficient measured by the Preston tube varied $\pm$ 0.75 percent across the span of the tunnel.

A single-wire boundary-layer-type hot-wire probe was used to measure the mean-velocity, U, and the square of the turbulence intensity, $\overline{u'^2}$, profiles at X/T = -2.15 (Figures 4 and 5). The boundary layer thickness measured 0.695 inches at X/T = -2.15 and Z/T = 0. The hot wire was also used to check the spanwise uniformity of the flow. Boundary-layer profiles of U and $\overline{u'^2}$ (Figures 10 and 11) were measured at X/T = -9.47 and Z/T = 0, 1.68, 3.63, and 5.23. The mean-velocity profiles agree except at very small Y. These differences are largely due to the uncertainties in measuring the Y location. The measurements were made with different hot-wire calibrations which also contributed to the uncertainty. The boundary-layer thickness measured 0.462 inches at X/T = -9.47

and Z/T = 0. A Clauser plot of these mean-velocity profiles is shown in Figure 12. The dotted line upon which the semi-logarithmic region of a mean-velocity profile lies is the value of the surface-skin-friction coefficient for that profile. The surface skin-friction coefficient for these profiles is 0.0026.

In an attempt to achieve the same boundary-layer thickness as in the Boundary-Layer Tunnel with the thin approach boundary layer, a "false floor" was designed for the Stability Wind Tunnel test section. It consisted of five sections of 3/4 inch thick "finform" plywood reinforced from below with 3 inch wide aluminum channel. The "false floor" was mounted on a 2 x 2 x .25 inch steel wall angle bolted to the side walls of the test section at about their mid-height. The height of the test section in the Stability Wind Tunnel is significantly greater than the height of the test section in the Boundary-Layer Tunnel. A sketch of the "false floor" in the Stability Wind Tunnel is shown in Figure 13. A 3 inch wide, 1/4 inch thick aluminum strip that spanned the test section was mounted to the "finform" plywood and formed the leading edge. The streamwise location of the leading edge is the same as for the "false floor" in the Boundary-Layer Tunnel. The leading edge of the aluminum strip was rounded in an attempt to avoid separation.

The "false floor" was equipped with static pressure ports spaced every foot along Z/T = 0 to record any pressure variation. The pressure ports had 1 millimeter diameter holes to measure the static pressure. The inclination of the floor could be changed ± 0.2 degrees so that a zero streamwise pressure gradient

could be achieved throughout the test section. At several streamwise locations, pressure ports were placed across the span to examine the uniformity of the flow.

The wing was mounted to the "finform" plywood in the same manner as in the Boundary-Layer Tunnel with a thin approach boundary layer. The previously described circular plate arrangement allowed for the wing to be rotated to any desired angle of attack. Angles of attack were referenced from the position of the wing at the zero degrees angle of attack.

Only the thin boundary-layer case was studied in the Stability Wind Tunnel. Measurements of the approach boundary layer in the Stability Wind Tunnel were made using a hot wire and are shown in Figures 14 and 15. The boundary-layer thickness measured 0.502 inches at $X/T = -9.56$ and $Z/T = 0$. This is slightly larger than the boundary layer thickness of 0.462 measured at $X/T = -9.47$ and $Z/T = 0$ in the Boundary-Layer Tunnel.

Instrumentation and Experimental Technique

Surface-Oil-Flow Visualizations

The technique for attaining the oil-flow visualizations was devised by Peter Sutton at Cambridge University and is described by Devenport and Simpson (1987b). Sutton's system consists of applying an opaque black self-adhesive plastic sheet to the surface of which the oil-flow visualization is to be performed.

A mixture of titanium dioxide, kerosene, and oleic acid is needed for application to the plastic sheet. The relative volumetric quantities of each change slightly , but it was found that 49 parts titanium dioxide, 14 parts kerosene, and 5 parts oleic acid worked very well. A thin layer of the mixture is then spread on the area of the oil-flow visualization. To avoid most brush marks, this is best done by using a brush made of sponge. The mixture should be applied with spanwise strokes so that any brush marks will not be mistaken for skin-friction lines. After the mixture is applied, the wind tunnel is started and allowed to settle at the desired flow conditions. When the mixture is completely dry, the plastic sheet can be removed from the test floor with the oil-flow visualization intact. The oil-flow visualization can then be preserved by spraying on a coat of fixer, similar to that used to prevent smudging of charcoal or chalk drawings. The oil-flow visualizations can now be handled with out any risk of smudging. Photocopies of the oil-flow visualizations can then be made.

As the flow passes over the plastic sheet, the mixture flows along skin-friction lines. Since skin friction is related to the velocity gradient normal to the wall, the skin-friction lines also give some indication of the near-wall velocity field. Thus, it can be presumed that regions of higher shear stresses, which appear as darker regions on the oil-flow visualizations, are also regions of higher near-wall velocities. A detailed discussion of the interpretation of oil-flow visualizations can be found in Peake and Tobak (1982).

Time-Mean Surface-Static-Pressure Measurements

Pressure taps with 1 millimeter diameter holes were placed primarily on the positive Z_1 side of the test floor surrounding the wing. The pressure ports were concentrated in areas where the pressure gradients were expected to be large. The uncertainty in port location is ± 0.3 millimeters.

A scanivalve system made by Scanivalve Corporation and two SETRA model 239 differential pressure transducers were used to measure the static pressures at different port locations. These values were recorded by an IBM-PC microcomputer. The scanivalve system consisted of a 48J9-1 scanivalve, a JOETM-48 position transmitter, a JS4-48 Solenoid drive, a CTLR2/S2-S6 scanivalve controller, and a 48CF-1 female pneumatic connector. The IBM-PC and the scanivalve system were linked through a data translation DT2801-A analog-to-digital converter. The scanivalve system had the capability to step through 48 port locations in sequence. The stepping and homing of the scanivalve system was controlled by the IBM-PC through reed relays from a digital output port of the DT2801-A analog-to-digital converter linked to the CTLR2/S2-S6 controller. The port parity was determined by the position transmitter, read through a digital input port of the DT2801-A analog-to-digital converter. The position transmitter enabled the computer to determine if the scanivalve had stepped to a new location. The voltage outputs of two SETRA model 239 differential pressure transducers were read through the DT2801-A analog-to-digital converter. One of the transducers had a voltage range of 0 to 5

volts and was used to monitor the difference in free-stream total and static pressures. The other transducer had a range of ± 2.5 volts and measured the difference between the measured local and free-stream static pressures. A pressure coefficient, C_p, may be formed by the ratio of the pressure measured by the bipolar transducer to that measured by the unipolar transducer.

Sets of 48 pressure ports were joined to model 48CM-1 male pneumatic connectors manufactured by Scanivalve Corporation through plastic tubes. In turn, these connectors were joined to the 48CF-1 connector of the scanivalve system. The locations of the different ports were stored in a computer data file and could easily be assigned to the acquired data by logging the connector used.

Since the pressure ports were located primarily on the test floor to the positive Z_1 side of the wing, the asymmetric pressure distributions of the wings at angles of attack could not be obtained with one measurement. Measurements with the wings at both positive, and corresponding negative angles of attack were used to obtain the pressure distribution on the test floor surrounding the pressure and suction sides of the wings, respectively.

Upon data reduction, pressure values were deleted if it could be determined that there was a problem either with the port, the plastic tubing, or other malfunction. Due to the volume of data acquired, tabulated data are not presented in this paper, but are available on diskette upon request.

Hot-Wire Measurements

Measurements of U and $\overline{u'^2}$ profiles in the boundary layer and the freestream were made at numerous spanwise locations at X/C = 3. The collection of these spanwise profiles is termed the spanwise plane at X/C = 3.

In the Boundary-Layer Tunnel, hot-wire measurements in the spanwise plane at X/C = 3 were obtained by using a small 16 wire hot-wire rake custom made by DANTEC. The wires were gold plated Platinum with a 5 micron diameter. The spacing between the wires was 1 millimeter up to the fifth wire, 1.5 millimeters from the fifth to the eigth wire, and 2 millimeters from the eigth to the top wire. The total distance from the bottom wire to the top wire was 25.4 millimeters. This wire arrangement allowed for a very detailed profile to be measured near the wall, and a coarser profile in the outer boundary layer and freestream. Only the bottom seven wires were used due to the limited number of anemometers available for use.

In the Stability Wind Tunnel, measurements in the spanwise plane at X/C = 3 were made using the small custom-made hot-wire rake to get a fine detail of the U and $\overline{u'^2}$ profiles in the boundary layer. A large custom-made 16 wire hot-wire rake was then used in the freestream and vertical wake of the wing to obtain the values of U and $\overline{u'^2}$. The large rake was also made by DANTEC, and the wires were the same type as those for the small rake. The wires of the big rake were uniformly spaced 1/4 inch apart. The total distance from bottom wire to top wire was 3.75 inches. Photographs of both hot-wire rakes are shown in Figure 16.

The traverse system used in the Boundary-Layer Tunnel measurements consisted of separate motorized horizontal and vertical probe traverse mechanisms. The vertical traverse was calibrated in steps of 1/1000th of an inch. The traverse system was located above the test section. The traverse system used in the Stability Wind Tunnel measurements was a digitally-controlled closed-loop motorized system. It had a resolution of 1/100th inch in the horizontal direction, and a 1/25th inch resolution in the vertical direction. This traverse system was located in the test section downstream of the spanwise plane at X/C = 3.

Constant temperature anemometer bridges of the type designed by Miller (1976) and modified by Simpson *et al.* (1979) were used for all measurements. In the Boundary-Layer Tunnel, a set of custom-made amplifiers was used between the bridge output of the anemometers and the input to the DT2801-A analog-to-digital converter. The amplifiers were not used in the Stability Wind Tunnel measurements.

The hot-wire rakes were calibrated in the potential core of each test section. The non-linearized output of the DT2801-A analog-to-digital converter was linearized by an IBM-PCAT microcomputer using King's Law. The law states that

$$E^2 = A + BU^n \tag{3}$$

where A, B, and n, are constants determined by calibration. E is the voltage read by the anemometer, and U is the mean velocity. The ambient temperature of the flow was recorded and Bearman's (1971) correction for temperature was used to

correct the calibration for differences from the calibration temperature. This correction alters the value of the constants A and B to account for the temperature difference.

Measurements of U and $\overline{u'^2}$ were made to a height of 4.25 and 13.5 inches above the test floor in the Boundary-Layer and Stability Wind Tunnels, respectively.

For all measurements made in the Boundary-Layer Tunnel, only the spanwise wake plane to the negative Z side of the wing was traversed. This was also the case for measurements made in the Stability Wind Tunnel with the wings at zero degrees angle of attack. For measurements made in the Stability Wind Tunnel with the wings at six degrees angle of attack and with no wing model, the entire spanwise plane was traversed.

There were several problems in performing the hot-wire anemometry in the Stability Wind Tunnel. Most significantly, the Stability Wind Tunnel is exposed to the outside temperature. This causes the temperature inside the test section to vary on the order of ten degrees Centigrade during the course of a day. To combat this problem, a procedure was incorporated into the data acquisition system whereby the hot-wire calibration could be adjusted to account for the change in flow temperature. The voltage measured by the hot-wire, and the velocity measured by a pitot-static tube located in the freestream at X/C = 3 were used to determine a constant by which the coefficients A and B needed to be multiplied in order to reestablish a proper calibration. There were instances when the temperature was allowed to vary too much before the recalibration procedure

was initiated. In those instances, the correction of the calibration was performed upon data reduction instead of on-line.

Due to the volume of data acquired, tabulated data are not included in this paper, but are available on diskette upon request.

III. Experimental Results and Discussion

Surface-Oil-Flow Visualizations

The results for the surface-oil-flow visualizations on the test floor surrounding the baseline wing are shown in Figures 17 through 21. The oil-flow visualizations on the test floor surrounding the baseline wing in the Stability Wind Tunnel were obtained through the use of two sheets of the black adhesive plastic. The overlap of the two sheets shows up as a horizontal line in the oil-flow visualizations (Figures 19 through 21). This line should not be mistaken as a feature of the oil-flow visualization. The oil-flow visualizations for the thick and thin approach boundary layers in the Boundary-Layer Tunnel with the baseline wing at zero degrees angle of attack are nearly the same (Figures 17 and 18).

At $X_1/T = -0.47$ and $Z_1/T = 0$ there is a point where the titanium dioxide in the mixture amasses for the wing at zero degrees angle of attack (Figures 17

through 19). The wall shear stress is zero at this point, and the flow has separated from the test floor. The pattern of the skin-friction lines near this point define it as a saddle point as described by Peake and Tobak (1982). The distance of the saddle point from the wing surface (0.47T) is not affected by angle of attack (Figures 20 and 21).

Emerging from the saddle point in each of the oil-flow visualizations (Figures 17 through 21) is a leading edge separation line, as defined by Peake and Tobak (1982). The skin-friction lines converge to this line, the limiting streamlines presumably rising away from the surface. At angles of attack, the convergence of the skin-friction lines towards the leading edge separation line appears to be greater on the test floor on the suction side of the wing than on the pressure side (Figures 20 and 21).

In each of the oil-flow visualizations (Figures 17 through 21) there is a region of high wall shear stress and presumed high near-wall velocity in the nose region near the wing surface. This is believed to be caused by a junction vortex that has formed immediately ahead of the nose of the wing. This junction vortex draws higher velocity (and energy) fluid from the outer part of the boundary layer and the freestream toward the wall. The pattern of the skin-friction lines in this region suggest that the near-wall flow is in the upstream direction.

It is presumed that as the near-wall flow proceeds upstream, its momentum decreases. The wall shear stress also decreases, causing the titanium dioxide removed from the test floor near the nose of the wing to amass and form a layer of the mixture upstream of the wing nose (Figures 17 through 21). The thickness

of this layer is large enough so that the near-wall spanwise pressure gradients to either side of the flow centerline cause the layer to move in the spanwise direction. This layer is characterized by low wall shear stresses, as measured by Devenport and Simpson (1987c), and is termed the line of low shear. A point on the line of low shear is at $X_1/T = -0.28$ and $Z_1/T = 0$ with the wing at zero degrees angle of attack (Figures 17 through 19). The line of low shear is also 0.28T from the wing surface measured along the direction of the incoming flow with the wing at six degrees (Figure 20) and twelve degrees (Figure 21) angle of attack.

Further downstream, the line of low shear merges with the leading edge separation line. For the cases with the baseline wing at zero degrees angle of attack (Figures 17 through 19), this merger occurs at about $X_1/T = 1.6$ on the test floor to either side of the wing. With the wing at six degrees angle of attack (Figure 20), the merger occurs at about $X_1/T = 1.2$ and $X_1/T = 2.1$ on the test floor to the suction and pressure sides of the wing, respectively. At twelve degrees angle of attack (Figure 21), the merger of the line of low shear with the leading edge separation line occurs at $X_1/T = 0.7$ and $X_1/T = 2.3$ on the test floor to the suction and pressure sides of the wing, respectively.

The flow separates in the corner between the wing and the floor at $X_1/T = 3.9$ for each case with the wing at zero degrees angle of attack (Figures 17 through 19). With the wing at six degrees angle of attack (Figure 20), the flow separates at $X_1/T = 3.8$ and $X_1/T = 4.0$ in the corner to the suction and pressure sides of the wing, respectively. When the angle of attack of the wing is increased to twelve

degrees (Figure 21), the flow separates at $X_1/T = 3.7$ and $X_1/T = 4.1$ in the corner to the suction and pressure sides of the wing, respectively.

There is a divergence of the skin-friction lines downstream of the trailing edge for all oil-flow visualizations made of the test floor surrounding the baseline wing. Bradshaw (1987) attributes this divergence to the junction vortex. He states that the divergence of the skin-friction lines is confined to the near-wall region where the momentum of the fluid is low. Aft of the trailing edge, the wing no longer imposes a resistance to the rotation of the vortex. Thus, the spanwise component of wall shear stress, presumably due to the vortex, is greater aft of the trailing edge. This causes the divergence of the skin-friction lines.

The spanwise (Z_1) distance between the two sides of the leading edge separation line measured at the trailing edge is 1.7T for all cases with the wing at zero degrees angle of attack (Figures 17 through 19). This distance is 1.9T and 2.1T for the wing at six (Figure 20), and twelve (Figure 21) degrees angle of attack, respectively.

The results for the oil-flow visualization of the test floor surrounding the wing with fillet are shown in Figures 22 through 26. As in Figures 17 and 18, the thickness of the boundary layer does not appear to affect the surface-oil-flow visualization. As for the baseline wing, the horizontal line, or gap, in the oil-flow visualizations (Figures 24 through 26) is due to the overlap of the two plastic sheets and should not be mistaken as a feature of the flow. The location of the saddle point is $X_1/T = -0.8$ and $Z_1/T = 0$ for all cases with the wing with fillet at zero degrees angle of attack (Figures 22 through 24). The distance from the wing

surface to the saddle point (0.8T) is not affected by increases in angle of attack, and is greater than for the baseline wing (Figures 17 through 21).

The location the line of low shear at $Z_1/T = 0$ is $X_1/T = -0.6$ for all cases of the wing with fillet at zero degrees angle of attack (Figures 22 through 24). When the wing with fillet is placed at an angle of attack (Figures 25 and 26), the line of low shear is also 0.6T from the wing surface measured along the direction of the incoming flow. The distance of the line of low shear from the wing surface is greater for the wing with fillet as compared to the baseline wing.

The region of high wall shear stresses and presumed high near-wall velocities in the nose region is small in all cases for the wing with fillet. Since this region is present but small, it is presumed that the vortex may reside above the fillet. The research of Pierce, *et al.*, (1988) exhibits that this is indeed the situation.

In each case (Figures 22 through 26), the skin-friction lines converge toward the leading edge separation line on the test floor to either side of the wing with fillet. With the wing at an angle of attack (Figures 25 and 26), the convergence appears to be greater on the test floor to the suction side of the wing as compared to the pressure side.

The merger of the line of low shear with the leading edge separation line occurs at $X_1/T = 1.6$ for all cases with the wing at zero degrees angle of attack (Figures 22 through 24). This is the same location as in each of the cases with the baseline wing at zero degrees angle of attack (Figures 17 through 19). The merger to the suction side of the wing occurs at $X_1/T = 0.7$ and $X_1/T = 0.5$ with the wing at six (Figure 25) and twelve (Figure 26) degrees angle of attack,

respectively. This location is further upstream than the corresponding baseline cases in Figures 20 and 21, respectively. On the floor to the pressure side, the merger occurs at $X_1/T = 2.3$ and $X_1/T = 2.5$ with the wing at six and twelve degrees angle of attack, respectively. These locations are further downstream than the corresponding cases with the baseline wing at angles of attack.

Since the oil-flow visualizations of the test floor surrounding the wing with fillet do not show the skin-friction line patterns any closer to the wing surface than the radius of the fillet, it is difficult to determine the exact location of the separation in the trailing edge region. However, the photograph of the wing with fillet at zero degrees with a thick approach boundary layer (Figure 27) indicates that the flow separation occurs at the wing trailing edge. This was the same for all wing with fillet cases.

The spanwise (Z_1) distance between the two sides of the leading edge separation line measured at the trailing edge is 2.2T for all cases with the wing with fillet at zero degrees angle of attack. This distance is greater than for the baseline wing at zero degrees in Figures 17 through 19. With the wing at six and twelve degrees angle of attack, this distance is 2.3T and 2.6T, respectively. Each of these distances is greater than the corresponding baseline wing case in Figures 20 and 21.

The divergence of the skin-friction lines aft of the trailing edge is present in each of the wing with fillet cases, and is slightly greater than the divergence of the skin-friction lines in each of the baseline wing cases.

Figures 28 through 30 are oil-flow visualizations on the baseline wing surface at 0, 6, and 12 degrees angle of attack, respectively. These oil-flow visualizations were attained by wrapping the plastic sheet about the wing. The trailing edge is at the far left-hand and right-hand sides, and the leading edge is in the center of the figures. The test floor is at the bottom. It should be noted that for oil-flow visualizations taken on a vertical surface, gravity tends to turn the skin-friction lines downward. In each of the oil-flow visualizations there is a stagnation line near the centerline, through which the skin-friction lines do not pass. A laminar separation and turbulent reattachment bubble is present to the pressure and suction sides of the stagnation line at zero and six degrees angle of attack. With the wing at twelve degrees angle of attck, the separation bubble is no longer present to the pressure side of the stagnation line. In this region, the flow has separated from the surface leaving no distinct skin-friction line patterns. There is also separation near the trailing edge in each of the oil-flow visualizations. A key thing to note is that there is no massive separation from the wing up to twelve degrees angle of attack.

As the angle of attack of the baseline wing is increased, the separation bubble on the pressure side of the wing becomes smaller whereas on the suction side, the structure remains the same width. This is because the adverse streamwise pressure gradient on the pressure side is becoming weaker as the angle of attack is increasing, and therefore the flow is able to remain attached for a longer distance. This is not true on the suction side where the adverse streamwise pressure gradient increases with increases in angle of attack.

The skin-friction lines near the top of the wing turn upwards on the pressure side of the wing at 6 and 12 degrees angle of attack in Figures 29 and 30, respectively. The pressures of the decelerated flow to the pressure side of the wing are greater than the free-stream pressure above the wing, thus causing the flow to go over the top of the wing. This turns the skin-friction lines upward. The opposite effect is present on the suction side where the pressure of the accelerated flow to the side of the wing is less than above the wing . It is difficult to interpret how much of the downward slant of the skin-friction lines on the suction side is due to gravity and how much is due to the pressure difference. However, if the oil-flow visualizations for the wing at angles of attack (Figures 29 and 30) are compared to the one for the wing at zero degrees angle of attack (Figure 28), it can be seen that the magnitude of the downward slant increases with increases in angle of attack.

These same features can be seen on the oil-flow visualizations for the wing with fillet in Figures 31 through 33. A piece of the plastic sheet near the wing leading edge at the test floor needed to be removed in order to wrap the sheet around the fillet. Again, there is a stagnation line near the center of the oil-flow visualization. The laminar separation and turbulent reattachment bubble is present for zero degrees angle of attack on both sides of the wing and decreases in width on the pressure side as the angle of attack increases. There is no massive separation at any angle of attack. The upward and downward slants of the skin-friction lines on the pressure and suction sides of the wing, respectively, are present for each oil-flow visualization on the wing with fillet at angles of attack.

Surface-Static Pressure Measurements

Mean-static-pressure measurements were made on the test floor surrounding both the baseline wing and wing with fillet. The estimated uncertainties for these experiments are stated in Table 1. The method described in Kline and McClintock (1953) was used to calculate the uncertainties. All measurements were made with a thin approach boundary layer. The measurements made in the Boundary-Layer Tunnel were restricted to the wings at zero degrees angle of attack. In the Stability Wind Tunnel, measurements were made with the wings at 0, 6, and 12 degrees angle of attack.

The pressure distribution on the baseline wing at zero degrees angle of attack in the Boundary-Layer Tunnel is shown in Figure 34. Ahead of the maximum thickness of the wing, large pressure gradients make the surface pressure highly sensitive to uncertainties in port location, thus causing the differences in pressure coefficient for corresponding ports on opposite sides of the wing. The sandpaper trip also contributes to the differences in this region. Downstream of the maximum thickness, the pressure gradients are much smaller, so the agreement in pressure coefficient appears much better. The differences in this region are presumably caused by the separation bubble shown in the oil-flow for the baseline wing at zero degrees angle of attack (Figure 28). However, the differences are within the combined uncertainties of port location and pressure coefficent. The agreement with the unbounded potential-flow calculation of the pressure distribution on an infinitely long baseline wing is quite good. The

reasons described above presumably cause the discrepancies ahead of the maximum thickness.

The same pressure measurement was used in the Stability Wind Tunnel to determine the position of the baseline wing at zero degrees angle of attack. The results are shown in Figure 35. The differences in the values of pressure coefficient for corresponding ports on opposite sides of the wing are within the combined uncertainties of port location and pressure coefficient. As in the Boundary-Layer Tunnel, the agreement with the unbounded potential-flow calculation is quite good with the exception of the region affected by the separation bubble, as described above.

The results for the pressure coefficient distribution on the test floor surrounding the baseline wing are shown in Figures 36 through 39. The discontinuity of the pressure contours along $Z/T = 0$ for the distributions with the wing at angles of attack (Figures 38 and 39) exist because the measurements on either side of the wing were not taken at the same time. For the figures showing the pressure distribution with the baseline wing at zero degrees (Figures 36 and 37), an unbounded potential-flow calculation of the distribution on the test floor surrounding an infinitely long baseline wing is included. The distributions for both measured cases at zero degrees angle of attack are nearly the same as shown in Figures 36 and 37. The pressure rise ahead of the wing in the measured distributions is not as high as for the unbounded potential-flow calculation. The measured spanwise pressure gradient up to the maximum thickness of the wing is also not as great as the spanwise pressure gradient for the unbounded potential

flow calculation. The minimum pressure coefficient at the maximum thickness of the wing is -0.8 for the wing at zero degrees angle of attack in both the Boundary-Layer and Stability Wind Tunnels. Each of these values is substantially greater than the value of -1.3 for the unbounded potential-flow calculation.

The measured pressure contours are distorted as compared with those pressure contours of the potential-flow calculation. Near the wing, the measured pressure contours are distorted such that the pressures in this region are lower than they would be without distortion. On the 0.2 pressure contour, this distortion is centered at $X_1/T = -0.18$ and $Z_1/T = 0.33$. The distance from the wing surface of this distortion is not affected by increases in angle of attack as seen in Figures 38 and 39. This region of lower pressures suggests a region of higher near-wall velocities. The presumed higher near-wall velocities is presumably produced by the junction vortex. This proposed region of higher near-wall velocities lies in the region of higher surface shear stress shown in the oil-flow visualization of the test floor surrounding the baseline wing (Figures 17 through 21).

Slightly further away from the wing nose, there is another distortion in the measured pressure contours of the test floor surrounding the baseline wing at zero degrees angle of attack. The pressures in this region are higher than they would be if the contours were not distorted, suggesting a region of lower near-wall velocities. On the 0.2 pressure contour, this region is centered at $X_1/T = -0.25$ and $Z_1/T = 0.47$. The distance from the wing surface of the distortion is not affected

by increases in angle of attack (Figure 38 and 39). This distortion in the measured pressure contours lies in the region between the line of low shear and the leading edge separation line where the wall shear stresses and presumed near-wall velocities are low (Figures 17 through 21).

As shown in Figures 38 and 39, the distortions in the pressure contours on the test floor to the pressure side of the wing are greater than to the suction side. The pressure rise ahead of the wing is greater for each angle of attack than for the baseline wing at zero degrees angle of attack (Figures 36 and 37). The spanwise pressure gradient on the test floor near the maximum thickness of the wing increases on the suction side, and decreases on the pressure side with increases in angle of attack. The minimum pressure coefficient measured on the pressure side increases with angle of attack, and is -0.41 and -0.13 with the wing at six (Figure 38) and twelve (Figure 39) degress, respectively. The minimum pressure coefficient to the suction side of the wing decreases with increases in angle of attack, and is -1.21 and -1.6 with the wing at six and twelve degrees, respectively.

The pressure recovery near the trailing edge is the same for all measured distributions of the pressure on the test floor surrounding the baseline wing. The pressure recovery for the unbounded potential flow calculation is greater than that for each of the measured baseline wing cases.

The results for the pressure distribution on the test floor surrounding the wing with fillet are shown in Figures 40 through 43. Pressure measured on the fillet are included in these figures. Because the measurements on the suction and

pressure sides with the wing with fillet at angle of attack were not taken at the same time, there are discontinuities in the pressure contours along $Z/T = 0$ (Figures 42 and 43).

For the wing with fillet at zero degrees angle of attack (Figures 40 and 41), the unbounded potential flow calculation of the distribution on the test floor surrounding an infinitely long baseline wing was included. The distributions on the test floor surrounding the wing with fillet are nearly the same in both wind tunnels. The minimum pressure coefficients near the maximum thickness of the wing are -1.01 and -1.03 in the Boundary-Layer and Stability Wind Tunnels, respectively. These values are substantially lower than for the baseline wing at zero degrees angle of attack (Figures 36 and 37). This is probably because the pressure ports for these cases are well above the test floor in this region. The minimum pressure coefficient measured for the wing with fillet cases is higher than that for the unbounded potential flow calculation. The pressure rise ahead of the wing with fillet at zero degrees angle of attack is slightly higher than for the baseline wing at zero degrees angle of attack. Again, this is presumably because the pressure ports near the wing are no longer on the test floor. The spanwise pressure gradient near the maximum thickness is greater than for the baseline cases at zero degrees angle of attack, and is lower than the unbounded potential flow calculation of the spanwise pressure gradient.

The contour distortions present in the baseline cases at zero degrees angle of attack (Figures 36 and 37) are again present for the wing with fillet cases at zero degrees angle of attack (Figures 40 and 41). The region of lower pressures is

centered at $X_1/T = -0.02$ and $Z_1/T = 0.5$ on the 0.1 contour for the wing with fillet at zero degrees angle of attack. This is 0.35T from the wing surface which is less than the radius of the fillet, suggesting that part of the vortex has formed above the fillet. The distance from the wing of this distortion is not affected by increases in angle of attack (Figures 42 and 43). This region of lower surface pressure lies in the region of higher shear stresses seen in the oil-flow visualizations in Figures 22 through 26. The region of higher pressures for the wing with fillet at zero degrees angle of attack is centered at $X_1/T = -0.25$ and $Z_1/T = 0.72$ on the 0.1 contour. The distance from the wing surface of this distortion is also not affected by increases in angle of attack. The region of higher surface pressure lies in the region between the line of low shear and the leading edge separation line in the oil-flow visualizations. The distances from the wing with fillet of the regions of lower and higher pressures are greater than the corresponding distances in the cases for the baseline wing (Figures 36 through 39). This suggests that the wing with fillet has displaced the vortex further from the wing.

At non-zero angles of attack (Figures 42 and 43), the distortions in the pressure contours are greater on the test floor to the pressure side of the wing than on the suction side. The pressure rise ahead of the wing is slightly larger than for the zero degree angle of attack cases (Figures 40 and 41). As the angle of attack of the wing with fillet increases, so does the spanwise pressure gradient on the test floor to the suction side of the wing, as is the case for the baseline wing in Figures 38 and 39. The spanwise pressure gradient to the pressure side of the

wing with fillet decreases with increases in angle of attack as shown in Figures 42 and 43. The minimum pressure coefficients near the maximum thickness of the wing on the suction side are -1.43 and -1.71 with the wing at six and twelve degrees angle of attack, respectively. These values are much lower than for the baseline case at corresponding angles of attack, presumably due to the pressure ports that are no longer on the test floor. The minimum pressure coefficients to the pressure side of the wing with fillet near the maximum thickness of the wing are -0.6 and -0.28 for the wing with fillet at six and twelve degrees angle of attack, respectively.

The pressure recovery near the trailing edge is about the same for all cases for the wing with fillet. This pressure recovery is higher than for each of the baseline cases.

Hot-Wire Rake Measurements

Hot-wire measurements of U and $\overline{u'^2}$ were made in the spanwise plane at X/C = 3 for both the baseline wing and wing with fillet. These measurements were also made for the empty test section case in each wind tunnel. The empty test section in the Boundary-Layer Tunnel is defined as the test condition with no model in the test section, and the removable plexiglas sections in place. In the Stability Wind Tunnel, the empty test section is defined as the test condition with no model in the test section. Estimated uncertainties in mean-velocity, U, and the

square of the turbulence intensity, $\overline{u'^2}$, were calculated by the methods used in Kline and McClintock (1953) and are presented in Table 1. U was normalized on the edge velocity, U_e, and $\overline{u'^2}$ was normalized on U_e^2 for all measurements. The uncertainty in U_e was found to be less than that in U.

Measurements made in the spanwise plane at X/C=3 for the empty test section are shown in Figures 44 through 49. These measurements are a direct indication of the spanwise uniformity of the flow. For each case in Figures 44 through 49, the contour plots of U/U_e and $\overline{u'^2}/U_e^2$ are nearly two-dimensional. The boundary-layer thickness measured by the height of the 0.99 contour from the wall is slightly greater for the thin boundary-layer case in the Boundary-Layer Tunnel (Figure 44) than for the Stability Wind Tunnel (Figure 48). For measurements made in the Boundary-Layer Tunnel, there is a slight decrease in the height of the U/U_e and $\overline{u'^2}/U_e^2$ contours from the test floor at Z/T greater than 4. This is presumably due to the influence of the side wall boundary layer. In Figures 45 and 47, the values of $\overline{u'^2}/U_e^2$ rise above 0.0001 in the upper right-hand corner of the plots. This feature is present in each of the $\overline{u'^2}/U_e^2$ contour plots for measurements made in the Boundary-Layer Tunnel (Figures 45, 47, 51, 53, 59, and 61). This rise in the value of $\overline{u'^2}/U_e^2$ could be due to some projection from the side wall that interferes with the flow, or the influence of the side wall boundary layer, although neither was confirmed.

The contouring routine used to generate the U/U_e and $\overline{u'^2}/U_e^2$ contours is as follows. The routine creates a curvilinear grid using all data points. Triangles consisting of three adjacent data points are then constructed. The routine then

searches along the sides of the triangles for values that match the desired contour by linearly interpolating between the data points that form the vertices of the triangle. The complete contours are then formed drawing straight lines connecting all points on the sides of all triangles that have the specific contour value. By using a linear interpolation scheme, the output contours will not be smooth. Zig-zags in the contours are a direct indication of the uncertainty in the data, and should not be mistaken for significant features of the flow. Since the velocities in the freestream are fairly constant, the 0.99 free-stream velocity contour is most influenced by uncertainties in the data, and is the least reliable of the U/U_e contours. The same logic holds for the $\overline{u'^2}/U_e^2$ contours near the wall where the gradient of $\overline{U'^2}$ normal to the wall is small, and causes the contours to be very erratic.

The results of the hot-wire measurements made with the baseline wing installed are shown in Figures 50 through 57. The U/U_e and $\overline{u'^2}/U_e^2$ contour plots with the baseline wing at zero degrees angle of attack in the Stability Wind Tunnel were obtained by reflecting the measured values at negative Z/T locations about Z/T = 0 to generate the points at positive Z/T locations. The centerline of the flow for these cases was determined by plotting spanwise profiles of U/U_e at a given distance from the test floor and then adjusting the Z datum so that the velocity profiles were symmetric about Z/T = 0. Slight differences in the contours to either side of Z/T = 0 are due to the contouring routine. The presence of the vortex is clearly indicated by the distortions in the U/U_e and $\overline{u'^2}/U_e^2$ contours in Figure 50 through 57. The vortex draws high energy and velocity fluid from the

outer boundary layer and free stream towards the wall, causing the contours of both U/U_e and $\overline{u'^2}/U_e^2$ in the outer boundary layer to be drawn near the wall. In each of the $\overline{u'^2}/U_e^2$ contour plots, the size of the vortex is associated with a region over which the $\overline{u'^2}/U_e^2$ values are significantly enhanced. This region is nearly the same size for the thin approach boundary-layer condition in the Boundary-Layer (Figure 51) and the Stability Wind (Figure 55) Tunnels.

The peak value of $\overline{u'^2}/U_e^2$ in the core of the vortex for the baseline case at zero degrees angle of attack is 0.0056 and 0.0061 for the thin and thick boundary layer cases in the Boundary-Layer Tunnel (Figures 53 and 55), respectively. This value is 0.0066 for measurements made in the Stability Wind Tunnel (Figure 55). For each case with the baseline wing at zero degrees angle of attack, the spanwise location of the peak value of $\overline{u'^2}/U_e^2$ is Z/T = 1.4.

In the $\overline{u'^2}/U_e^2$ contour plot for the baseline wing at six degrees angle of attack (Figure 57), the peak $\overline{u'^2}/U_e^2$ value in the core of the vortex to the suction side of the wing is 0.0081, and is located at Z/T = -0.5. To the pressure side of the wing, the peak value of $\overline{u'^2}/U_e^2$ in the core of the vortex is 0.0055, and is located at Z/T = 2.4. The spanwise distance between these peak values of $\overline{u'^2}/U_e^2$ is 2.9T. The region of enhanced $\overline{u'^2}/U_e^2$ values is slightly larger for the suction side vortex as compared to the pressure side vortex. As shown in Figures 56 and 57, the contours of both U/U_e and $\overline{u'^2}/U_e^2$ appear to be drawn deeper into the boundary layer by the suction side vortex than by the pressure side vortex. The wing tip vortex near the top of the suction side of the wing can also be seen in Figures 56 and 57.

If the edge of the vertical wake of the wing is defined as the 0.0001 $\overline{u'^2}/U_e^2$ contour, then the width of the vertical wake is about 0.9T for all measurements made with the baseline wing. For the Boundary-Layer Tunnel measurements, this width was obtained by doubling the spanwise distance between Z/T = 0 and the 0.0001 $\overline{u'^2}/U_e^2$ contour.

As shown in Figures 50 through 53, the boundary layer thickness had only small effects on the U/U_e and $\overline{u'^2}/U_e^2$ contours in the vicinity of the vortex. The U/U_e and $\overline{u'^2}/U_e^2$ contours in this region are slightly further from the test floor in the thick boundary-layer case than the corresponding contours in the thin boundary-layer case. Far from the vortex, there is a significant difference in the Y position of the contours due to the different boundary layer thicknesses. The shapes of the U/U_e and $\overline{u'^2}/U_e^2$ near the vortex are nearly the same for each boundary layer thickness.

Hot-wire measurements at X/C = 3 made with the wing with fillet installed are shown in Figures 58 through 65. As in the contour plots for the baseline wing cases (Figures 50 through 57), the U/U_e and $\overline{u'^2}/U_e^2$ contours of the outer boundary-layer region are drawn close to the wall by the vortex.

For each case, the U/U_e and $\overline{u'^2}/U_e^2$ contours are drawn closer to the wall than for the corresponding baseline wing case. In all cases, the region in the vicinity of the junction vortex over which the $\overline{u'^2}/U_e^2$ values are enhanced is larger for the wing with fillet (Figures 59, 61, 63, and 65) than for the baseline wing case (Figures 51, 53, 55, and 57).

In the Boundary-Layer Tunnel measurements, the peak value of $\overline{u'^2}/U_e^2$ in the core of the vortex is 0.0062 and 0.0061 for the cases with the wing with fillet at zero degrees angle of attack with a thin (Figure 59) and thick (Figure 61) approach boundary layer, respectively. This value is 0.0061 for the measurements made in the Stability Wind Tunnel (Figure 63). This peak value is located at Z/T = 1.6, which is further from Z/T = 0 than for each baseline wing case at zero degrees angle of attack (Figures 51, 53 and 55).

For the wing with fillet at six degrees angle of attack (Figure 65), the peak value of $\overline{u'^2}/U_e^2$ in the core of the suction side vortex is 0.00739 and is located at Z/T = -0.9. The same value for the pressure side vortex is 0.0055 and is located at Z/T = 2.4. The spanwise distance between these peak values is 3.3T which is greater than in the baseline case at six degrees in Figure 57. The region of enhanced $\overline{u'^2}/U_e^2$ values in the vicinity of the vortex is greater on the suction side as compared to the pressure side, as is the case for the baseline wing at six degrees angle of attack. The wing tip vortex seen in Figures 56 and 57 for the baseline wing is again present for the wing with fillet. The wing tip vortex is at the same location, and is about the same size for both the baseline wing and wing with fillet at six degrees angle of attack.

The width of the vertical wake of the wing with fillet, outlined by the 0.0001 $\overline{u'^2}/U_e^2$ contour, is 0.9T for all cases. This is the same value as for the baseline wing.

As in the U/U_e and $\overline{u'^2}/U_e^2$ contour plots for the baseline wing at zero degrees angle of attack in the Boundary-Layer Tunnel (Figures 50 through 53), the

boundary layer thickness had only small effects on the U/U_e and $\overline{u'^2}/U_e^2$ contours in the vicinity of the junction vortex for the wing with fillet at zero degrees angle of attack (Figures 58 through 61). In the vicinity of the vortex, the U/U_e and $\overline{u'^2}/U_e^2$ contours in Figures 58 and 59, respectively, are slightly closer to the wall than the corresponding U/U_e and $\overline{u'^2}/U_e^2$ contours in Figures 60 and 61. The shape of the U/U_e and $\overline{u'^2}/U_e^2$ contours in the vicinity of the vortex are about the same for each case.

Drag Calculations

The method used to calculate the drag coefficient, C_d, for the empty test section, the baseline wing, and the wing with fillet is similar to that used in Schlichting (1968). If the flow conditions at a spanwise plane upstream and downstream of the wing are known, a control volume can be constructed and the force due to drag, F_d, can be calculated. The control volume used in this calculation is shown in Figure 66. The width of the control volume, W, is 24 inches. The height of the control volume, H, is 4.25 and 13.5 inches for calculations made using the measurements in the Boundary-Layer and Stability Tunnels, respectively. The length of the control volume, L, is different for each test case. The equation for the momentum balance of the fluid, assuming only the forces F_d and the pressure, p, act on the control volume, and density is constant, is

$$\oint \rho \vec{V} \vec{V} dA = F_d + \oint p d\vec{A} \tag{4}$$

In this equation, ρ is the density, $\vec{V}$ is the velocity, and $d\vec{A}$ is a differential area. Applying this equation to all surfaces of the control volume and assuming the pressure is constant across planes 1 and 2, the contribution of $\overline{u'^2}$ to the equation is small, and the flow is uniform across plane 1, yields

$$(p_1 - p_2)(W)(H) - F_d = \underbrace{\int_{-W/2}^{W/2} \int_0^H \rho U(UdA)}_{2} - \underbrace{W \int_0^H \rho U(Udy)}_{1} + \underbrace{\int_{-W/2}^{W/2} \int_0^H \frac{\partial \dot{m}}{\partial A} UdA}_{3,4,5} \tag{5}$$

where p_1 is the pressure at the inlet plane (1), p_2 is the pressure at the exit plane (2), and $\dot{m}$ is the mass flow rate.

Conservation of mass states that

$$\oint \rho(\vec{V} d\vec{A}) = 0 \tag{6}$$

Applying this to all sides of the control volume yields

$$\int_2 \rho U dA - \int_1 \rho U dA = -\dot{m}_{3,4,5} \tag{7}$$

Substituting equation 7 into equation 5 and assuming that the mass flow out planes 3, 4, and 5 exits the control volume at the edge velocity, U_e, yields

$$F_d = (p_1 - p_2)(W)(H) - \int_{-W/2}^{W/2}\int_0^H \rho(U^2 - U(U_e))dA + W\int_0^H \rho(U^2 - U(U_e))dy \tag{8}$$

The value each integrand is zero for Y greater than the boundary-layer thickness, δ , therefore the upper limit of the Y integration can be replaced by δ. Thus, substituting in the definition of momentum thickness, θ, where

$$\theta = \int_0^\delta \frac{U}{U_e}(1 - \frac{U}{U_e})dy \tag{9}$$

and non-dimensionalizing the force due to drag by $1/2\rho U_e^2 cb$, where c is the chord of the wing and b is the span, yields

$$C_d = \frac{2WH}{\rho U_e^2 cb}(p_1 - p_2) + \frac{2}{cb}\int_{-W/2}^{W/2} \theta dz - \frac{2W\theta}{cb} 1 \qquad (10)$$

where C_d is the drag coefficient, and δ is the height of the boundary layer measured where $\overline{u'^2}/U_e^2 = 0.0001$.

A theoretical boundary-layer profile for the mean velocity was assumed from the test floor to the first data point. The law of the wall was used for values of y^+ less than 7, where y^+ is defined as $u^* Y/\nu$. The kinematic viscosity is ν, and u^* is the friction velocity ($U_e \sqrt{C_f/2}$). For values of y^+ between 7 and 50, the van Driest model for du^+/dy^+ was used, where u^+ is defined as U/u^*. For y^+ greater than 50, the equation

$$u^+ = 2.5 \log y^+ + 5.2 \qquad (11)$$

was used. The values of C_f needed to calculate u^* were found by iteration until the measured and above mentioned theoretical mean-velocity profiles were the same in the semi-logarithmic region. This iteration procedure consisted of plotting the theoretical and measured mean-velocity profiles, and adjusting C_f until the two profiles lied on top of each other in the semi-logarithmic region. This procedure assumes the flow is in equilibrium. The spanwise C_f distributions at X/C = 3 in the Stability Tunnel are shown in Figures 67 through 69 for the empty test section, and for the wings at zero and six degrees angle of attack, respectively. The distribution for the empty test section (Figure 67) is nearly uniform. The C_f distribution for the wings at zero degrees angle of attack is

shown in Figure 68. The assumption that the flow is in equilibrium is no longer valid in the vicinity of the vortex. Thus, the uncertainty in C_f in this region is high. However, a qualitative indication of the effect of the vortex on C_f can be inferred. The skin-friction coefficient reaches a minimum near the Z/T location where $\overline{u'^2}/U_e^2$ in the core of the vortex attains its peak (Figures 55 and 63). attains its peak. In the region where the U/U_e and $\overline{u'^2}/U_e^2$ contours of the hot-wire measurements (Figures 54, 55, 62, and 63) are drawn near the wall by the vortex, the C_f values are high. The C_f distribution is nearly the same for the baseline wing and wing with fillet. With the wings at six degrees angle of attack (Figure 69), the C_f distibutions exhibit the same features as in Figure 68. The values of C_f near the Z/T location of the peak $\overline{u'^2}/U_e^2$ value in the core of the vortex for the baseline wing and wing with fillet (Figures 57 and 65, respectively) are low. In the region where the contours of U/U_e and $\overline{u'^2}/U_e^2$ are drawn near the test floor, the C_f values are high.

The spanwise distribution of θ for each case is shown in Figures 70 through 74. The uncertainty in θ was estimated numerically by performing the integration in equation 9 with the measured data, and then recalculating the integral with the uncertainty in mean velocity randomly introduced into the calculation. The uncertainty is stated in Table 1. For the empty test section (Figure 70) in the Stability Wind Tunnel, the distribution is nearly uniform. In the Boundary-Layer Tunnel, the variance of θ is within the uncertainty, with the exception of the region influenced by the side wall boundary layer. The values of θ in the Stability Wind Tunnel and in the Boundary-Layer Tunnel with thin

approach boundary layer are nearly the same. The effects of the junction vortex on the θ distribution for the wings at zero degrees angle of attack are shown in Figures 71 through 73 for the thin and thick approach boundary layer in the Boundary-Layer Tunnel, and for the Stability Wind Tunnel, respectively. In each figure, θ is largest near the Z/T location of the peak $\overline{u'^2}/U_e^2$ value in the core. The values of θ in each figure are low in the region where the contours of $\overline{u'^2}/U_e^2$ are drawn near the wall by the vortex. In each case, the θ associated with the wing with fillet case reaches a higher value than for the baseline wing. The distributions for the thin approach boundary layer in the Boundary-Layer and Stability Wind Tunnels are nearly the same. With the wings at six degrees angle of attack (Figure 74), the same features are present. The value of θ reaches its maximum near the location of the peak $\overline{u'^2}/U_e^2$ value in Figures 57 and 65 for the baseline wing and wing with fillet, respectively. The values of θ are low in the region where the U/U_e and $\overline{u'^2}/U_e^2$ contours are drawn close to the wall.

The corresponding distributions of the displacement thickness, δ^*, are shown in Figures 75 through 79, respectively. Each of the figures exhibit the same features at the same locations as the corresponding momentum thickness distributions. The uncertainty in δ^* was estimated using the same numerical procedure as above, and is stated in Table 1.

The integration of the above non-dimensionalized momentum thickness distribution across plane 2 is the non-dimensionalized momentum deficit. For all calculations, plane 2 is at X/C=3. The values for the momentum deficit are shown in Table 2. The statistical uncertainty for this integration is minimal, but

the uncertainties in Z/T location and the trapezoidal rule used to integrate are significant. The uncertainty for the non-dimensionalized momentum deficit is ±5 percent. The values for the momentum deficit of the empty test section with the thin approach boundary layer in the Boundary-Layer and Stability Wind Tunnels are nearly the same. With the baseline wing or the wing with fillet installed, the momentum deficit for the Stability Tunnel calculation is greater than for the thin boundary-layer case in the Boundary-Layer Tunnel. This is caused by ignoring the vertical wake of the wing above Y = 4.25 inches in the Boundary-Layer Tunnel. The values for the thick approach boundary layer are significantly larger than for the thin boundary layer in each wind tunnel. The difference between the momentum deficit for the baseline wing and wing with fillet is less than the uncertainty in the value for each test case.

To calculate the drag coefficient, it was necessary to define the streamwise location of plane 1. It is important that plane 1 be far enough upstream of the wing so that the flow is uniform across the span. In the Stability Wind Tunnel, plane 1 was at X/T = -9.56 and the mean-velocity profile in Figure 14 was used in the calculation. In the Boundary-Layer Tunnel with the thin approach boundary layer, the mean-velocity profile at X/T = -9.47 and Z/T = 0 in Figure 10 was used for the inlet condition. Finally, for the Boundary-Layer Tunnel with the thick approach boundary layer, the mean-velocity profile at X/T = -18.2 and Z/T = 0 in Figure 80 was used for the inlet conditions.

The contribution to the drag of the pressure difference between planes 1 and 2 was found to be less than 2 percent. The contributions were 0.0015 in the

Stability Wind Tunnel, -0.0001 in the Boundary-Layer Tunnel with the thin approach boundary layer, and -0.000047 in the Boundary-Layer Tunnel with the thick approach boundary layer. The final results for C_d are shown in Table 3. The uncertainty in C_d is stated in Table 1. Comparisons between calculated values of C_d for the different wind tunnels and boundary-layer thicknesses cannot be made because the inlet conditions are not the same. However, in each case, the difference in C_d between the baseline wing and wing with fillet is within the incertainty in C_d.

Calculation of the Entrainment Rate of Free-Stream Fluid

The non-dimensionalized volumetric flow rate of turbulent fluid in a boundary layer is defined as

$$\frac{\dot{m}_{turb}}{\rho U_e b W} = \int_{-W/2}^{W/2} \int_{0}^{\delta} \frac{U}{U_e} dA \tag{12}$$

where W, δ, and ρ are defined the same as in the drag calulation. The values of the non-dimensionalized volumetric flow rate of turbulent fluid in the spanwise plane at X/C=3 are shown in Table 4. The uncertainty in this value was calculated in the same manner as for the uncertainty in θ, and is $\pm$5 percent. The

values for the flow rate are nearly the same for the empty test section in the Boundary-Layer Tunnel with thin approach boundary layer, and in the Stability Wind Tunnel. The flow rate is greater for the wings at zero degrees angle of attack in the Stability Wind Tunnel than for the thin approach boundary layer in the Boundary-Layer Tunnel because of the different value of H in each case. For each case, the volumetric flow rate of turbulent fluid is greater for the wing with fillet than for the baseline wing. However, the difference is within the uncertainty in the value.

The difference between the volumetric flow rate of turbulent fluid at planes 1 and 2 of the control volume is the rate of entrainment of free-stream fluid. This is a measure of the amount of non-turbulent fluid that has become turbulent between planes 1 and 2. The same control volumes used in the drag calculation were used in the calculation of the entrainment rate. The uncertainty in the value for the rate of entrainment of free-stream fluid, $\dot{m}_e$, is shown in Table 1.

The non-dimensionalized expression for the rate of entrainment of free-stream fluid is defined as

$$\frac{\dot{m}_e}{\rho U_e b W} = \frac{1}{Wb} \int_{2}^{-W/2} \int_{0}^{\delta} \frac{U}{U_e} dA - \frac{1}{b} \int_{1}^{0} \frac{U}{U_e} dy \qquad (13)$$

The values for the non-dimensionalized rate of entrainment of free-stream fluid are shown in Tables 4. As with the drag calculation, the use of different inlet planes for each boundary-layer thickness, and wind tunnel prevent comparison

between the different test cases. The values for the rate of entrainment are greater for the wing with fillet than for the baseline wing for each case. However, in each case the difference is within the uncertainty.

IV. Conclusions and Recommendations

Measurements were made to determine the effectiveness of a fillet as a flow control device. The results of measurements made for the baseline 1.5:1 elliptic nose, NACA 0020 tail wing and the same wing with a 1.5 inch radius fillet were compared. Hot-wire measurements in the spanwise plane at X/C=3 of each model were made to determine the uniformity of the flow, and to calculate the drag and entrainment rate of free-stream fluid. Oil-flow visualizations and surface-static-pressure measurements were made on the test floor surrounding each wing to establish the presence of the junction vortex.

The fillet does not appear to be a viable flow control device. For each measurement made, there are indications that the vortex is present for both the baseline wing and wing with fillet. In the oil-flow visualizations of the test floor surrounding each wing, the high shear stresses and presumed high near-wall velocities in the nose region near the wing are believed to be caused by the junction vortex. The divergence of the skin-friction lines near the trailing edge

was seen for each baseline wing and wing with fillet case, also suggesting the presence of a junction vortex. A region of lower surface pressure, and presumed higher near-wall velocity is present for each case in the nose region of the wing. These higher near-wall velocities are believed to be caused by the junction vortex which draws higher velocity flow from the outer boundary layer towards the wall. Hot-wire measurements at X/C = 3 also indicate the presence of a vortex in each case. The contours of U/U_e and $\overline{u'^2}/U_e^2$ are drawn towards the wall by the vortex. The wing with fillet draws the contours nearer to the wall in each case, which is an indication that the junction vortex may be slightly stronger for the wing with fillet case. The region over which the $\overline{u'^2}/U_e^2$ values are significantly enhanced is slightly larger for the wing with fillet than for the baseline wing. The peak value of $\overline{u'^2}/U_e^2$ in the core of the vortex is nearly the same for the baseline wing and wing with fillet.

The wing with fillet appears to displace the vortex further from the wing than the baseline wing. The distance of the leading edge separation line, and saddle point, from the wing is greater for the wing with fillet than for the baseline wing. The region of lower pressures in the surface pressure measurements is also further from the wing for the wing with fillet cases. The peak $\overline{u'^2}/U_e^2$ value in the core of the vortex is further from Z/T = 0 than for the baseline wing, which also indicates that the wing with fillet displaces the vortex further from the wing than the basline wing.

The drag and the entrainment rate of free-stream fluid are nearly the same for the wing with fillet and the baseline wing.

The effect of angle of attack on the junction vortex appears to be minimal. Although there is some asymmetry in the oil-flow visualizations with the wings at angle of attack, the overall symmetry is quite good. Apparently, the change in the curvature of the leading edge aligned with the approach flow did not significantly change with the changes in angle of attack. The location of the distortions in the measured pressure contours is not affected by the changes in angle of attack, but the magnitude of the distortions is. For each case at angle of attack, the U/U_e and $\overline{u'^2}/U_e^2$ contours are drawn toward the floor by the vortex. The amount that the contours are drawn to the wall is greater for the suction side vortex, indicating that it may be slightly stronger than the pressure side vortex.

The effects of boundary-layer thickness are also minimal. The oil-flow visualizations for each boundary-layer condition appear nearly the same. The height of the U/U_e and $\overline{u'^2}/U_e^2$ contours from the wall in the vicinity of the vortex is nearly the same for each boundary-layer thickness. The shape of these contours are also nearly the same in this region, as is the region over which the $\overline{u'^2}/U_e^2$ values are significantly enhanced.

This research has shown that the junction vortex present in the baseline wing test case is again present in the wing with fillet case. Each of the tests performed indicate that the vortex is nearly the same size and strength in both cases. With the purpose of the fillet being to alleviate the junction vortex and to reduce the drag and entrainment rate of free-stream fluid, it is not a successful flow control device. From the location of the region of lower pressures in the surface pressure measurements, and the small region of higher wall shear stresses near the wing in

the oil-flow visualizations, it appears that the vortex actually forms above the fillet itself. The fillet provides little obstruction to the formation of the vortex. In fact, it is possible that the curved surface imposes less resistance to the formation of the vortex than does the corner formed by the baseline wing and the test floor.

The area of leading edge flow control devices does have great potential in alleviating the wing-body-junction vortex, as shown by Kubendran (1988). A proper device that presents an appreciable obstacle to the formation of the wing-body-junction vortex can significantly improve the flow.

In this report, only the streamwise component of mean-velocity and square of turbulence intensity were investigated. A more detailed look into the other components of the flow would provide a great deal more information that could be used to quantify the strength and size of the vortex. This would be helpful in determining the extent to which this or some other leading edge flow control device is successful in improving the problems due to the presence of the junction vortex in the wing-body-junction flow.

References

Bearman, P.W.,"Correction for the Effect of Ambient Temperature Drift on Hot-Wire Measurements in Incpmpressible Flow," *DISA Information*, No. 11, May, 1971.

Beers, Y., *Introduction to the Theory of Error*, Addison-Wesley, Massachusetts, 1957.

Bradshaw, P.,"Turbulent Secondary Flows," *Annual Review of Fluid Mechanics*, Vol. 19, pp.53-74, 1987.

Bragg, G.M.,"The Turbulent Boundary Layer in a Corner," *Journal of Fluid Mechanics*, Vol. 36, pp.485-503, 1969.

Devenport, W.J., and Simpson R.L.,"Some Time-Dependent Features of Turbulent Appendage-Body Juncture Flows," *16th Symposium on Naval Hydrodynamics*, Berkeley, CA, 1986.

Devenport W.J., and Simpson R.L.,"Turbulence Structure Near the Nose of a Wing-Body Junction," *AIAA Paper 87-1310, AIAA 19th Fluid Dynamics, Plasma Dynamics and Lasers Conference*, Honolulu, Hawaii, 1987a.

Devenport, W.J., and Simpson R.L.,"An Experimental Investigation of the Flow Past an Idealized Wing-Body Junction: Preliminary Data Report," *Dept. of Aerospace and Ocean Eng., VPI&SU*, Blacksburg, VA, 1987b.

Devenport, W.J., and Simpson, R.L.,"Time-Dependent Structure in Wing-Body Junction Flows," *6th Symposium on Turbulent Shear Flows*, Toulouse, France, 1987c.

Devenport, W.J., and Simpson, R.L.,"LDV Measurements in the Flow Past a Wing Body Junction," *4th Symposium on Applications of Laser Anemometry to Fluid Mechanics*, Blacksburg, VA, 1988.

Hoerner, S.F.,"Practical Information on AERODYNAMIC DRAG and HYDRODYNAMIC RESISTANCE," *Fluid-Dynamic Drag*,1965.

Kline, J.J., and McClintock, F.A.,"Describing Uncertainties in Single Sample Experiments," *Mechanical Engineering (ASME)*, Vol. 75, pp.3-8, 1953.

Kubendran, L.R., Bar-Sever, A., and Harvey, W.D.,"Flow Control in a Wing/Fuselage-Type Juncture," *AIAA Paper 88-0614, AIAA 26th Aerospace Sciences Meeting*, Reno, Nevada, 1988.

Marchman, J.F., III, Abhati, A.A., and Sumantran, V.,"Acoustic Turbulence Influences on Stall Hysteresis," *AIAA Paper 86-0170*, Blacksburg, VA, 1986.

Mehta, R.D.,"Effect of Wing Nose Shape on the Flow in a Wing/Body Junction," *The Aeronautical Journal of the Royal Aeronautical Society*, pp.456-460, December, 1984.

Miller, J.A.,"A Simple Linearized Hot-Wire Anemometer," *Journal of Fluids Engineering*, Vol. 98, p.550, 1976.

Peake, D.J., and Tobak, M.,"Topology of Three-Dimensional Separated Flows," *Annual Review of Fluid Mechanics*, Vol. 14, pp. 61-85, 1982.

Pierce, F.J., Frangistas, G., and Nelson, D.J.,"Geometry Modification Effects on a Junction Vortex Flow," *Dept. of Mech. Eng., VPI&SU*, Blacksburg, VA, 1988.

Schetz, J.A., *Fundamentals of Boundary Layer Theory for Momentum, Heat, and Mass Transfer*, Prentice-Hall, Inc., Englewood Cliffs, NJ, 1984.

Schlichting, H., *Boundary Layer Theory*, McGraw-Hill, New York, 1968.

Shabaka, I.M.M.A. and Bradshaw, P.,"Turbulent Flow Measurements in an Idealized Wing/Body Junction," *AIAA Journal*, 19, pp. 131-132, 1981.

Shiloh, K., Shivaprasad, B.G., and Simpson, R.L., "The Structure of a Separating Turbulent Boundary Layer. Part 3. Transverse Velocity Measurements," *Journal of Fluid Mechanics*, Vol. 113, pp. 75-90, 1981.

Simpson, R.L., Heizer, K.W., and Nasburg, R.E.,"Performance Caharacteristics of a Simple Linearized Hot-Wire Anemometer," *Journal of Fluids Engineering*, Vol. 101, p.381, 1979.

Simpson, R.L., Chew, Y.T., and Shivaprasad, B.G., "The Structure of a Separating Turbulent Boundary Layer. Part 1. Mean Flow and Reynolds Stresses," *Journal of Fluid Mechanics*, Vol. 113, pp. 23-51, 1981.

Simpson, R.L., Shivaprasad, B.G., and Chew, Y.T., "The Structure of a Separating Turbulent Boundary Layer. Part 4. Effects of Periodic Free-Stream Unsteadiness," *Journal of Fluid Mechanics*, Vol. 127, pp. 219-261, 1983.

Figures

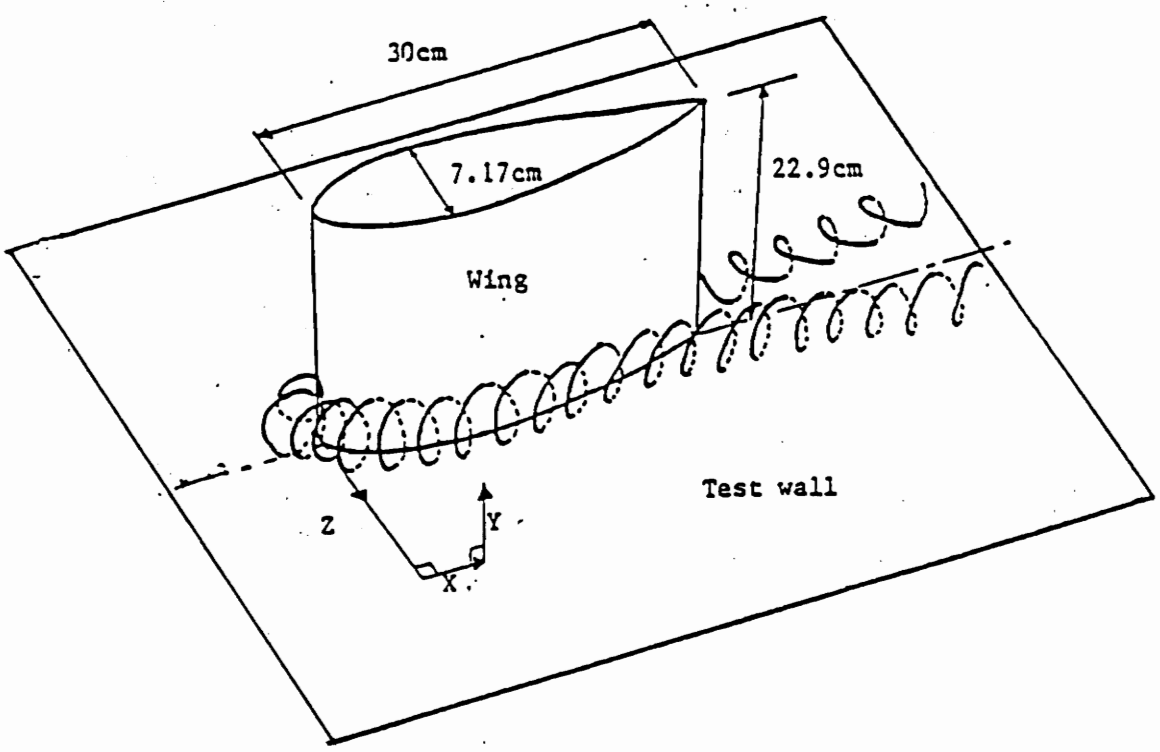

Figure 1. Illustration of the Horseshoe Vortex Formed in Wing / Body Junction Flows.

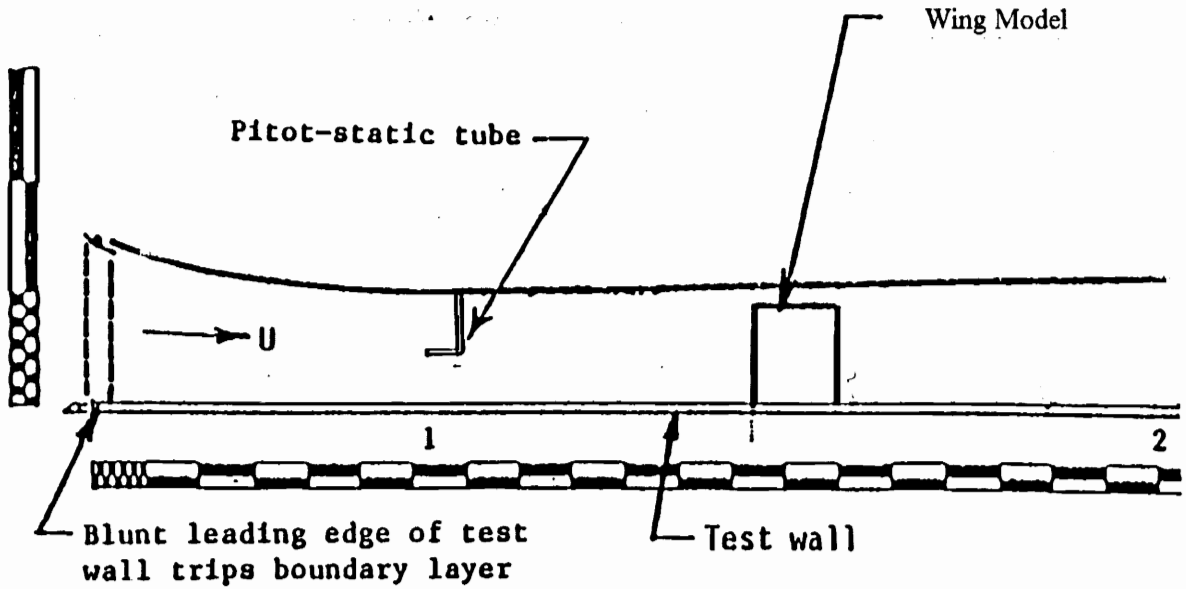

Figure 2. Side View of the Boundary Layer Tunnel and Test Section.

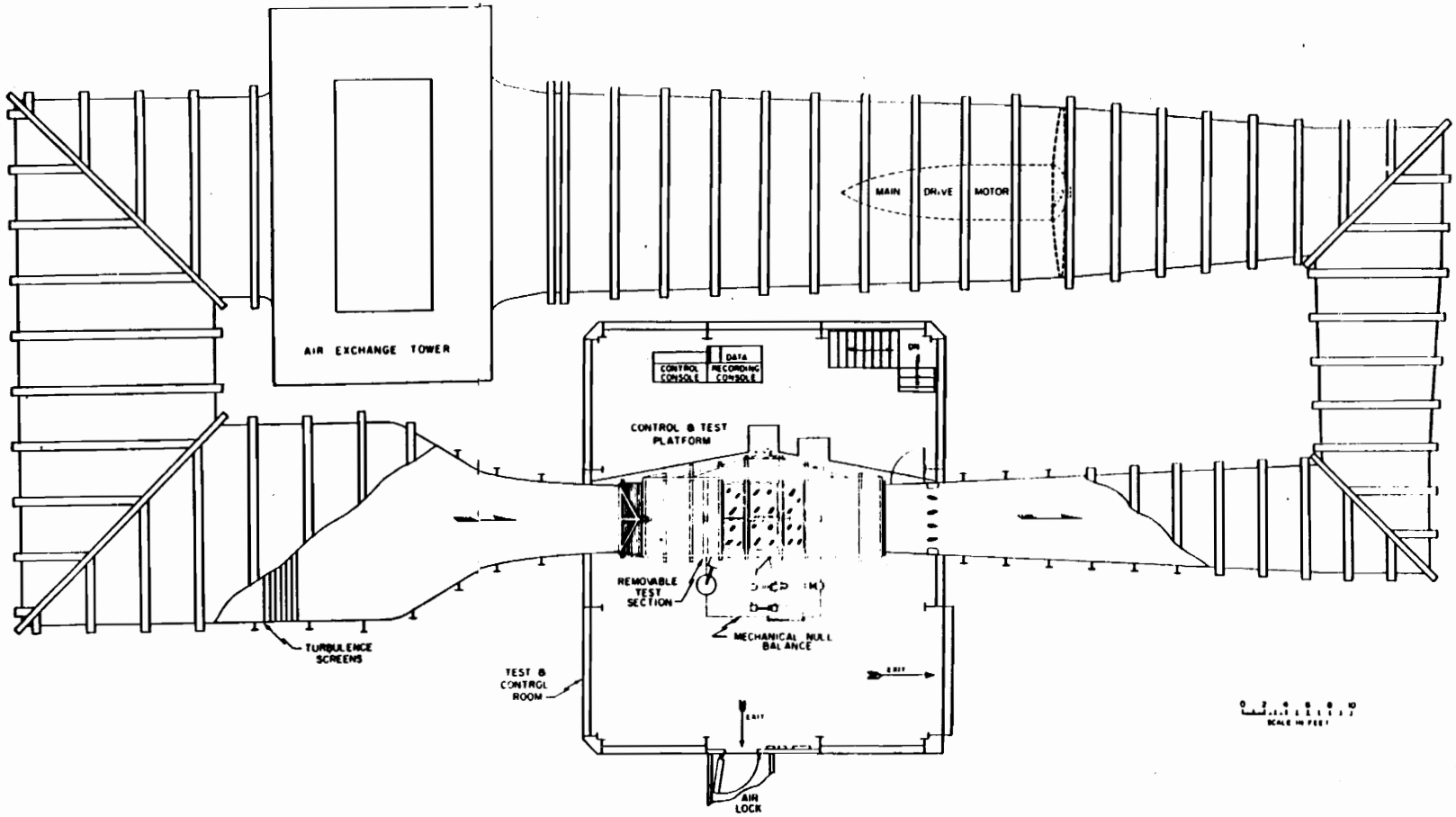

Figure 3. Diagram of the Stability Wind Tunnel.

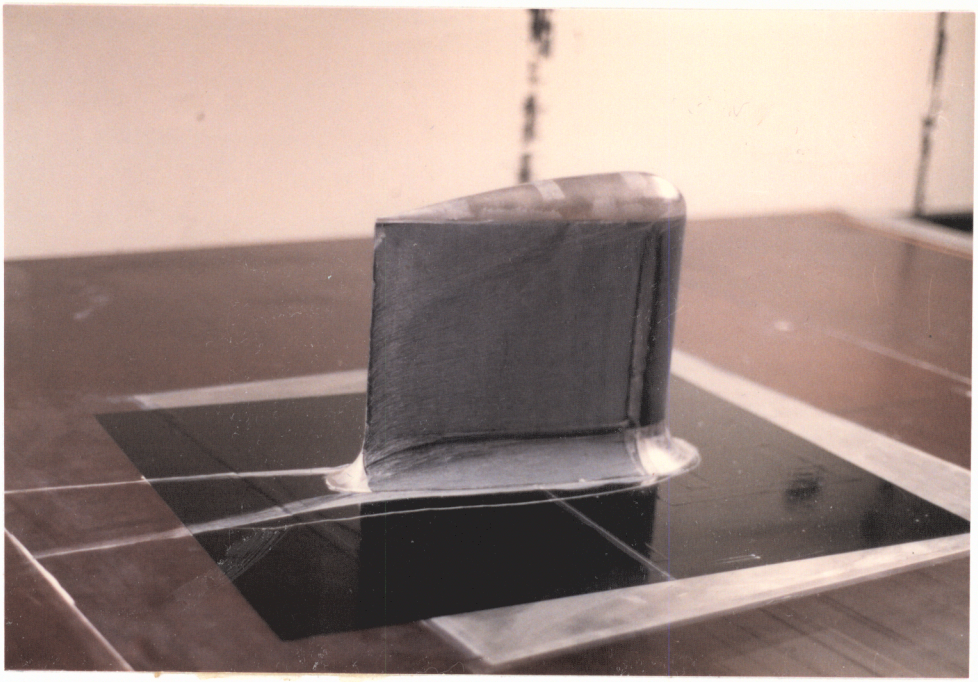

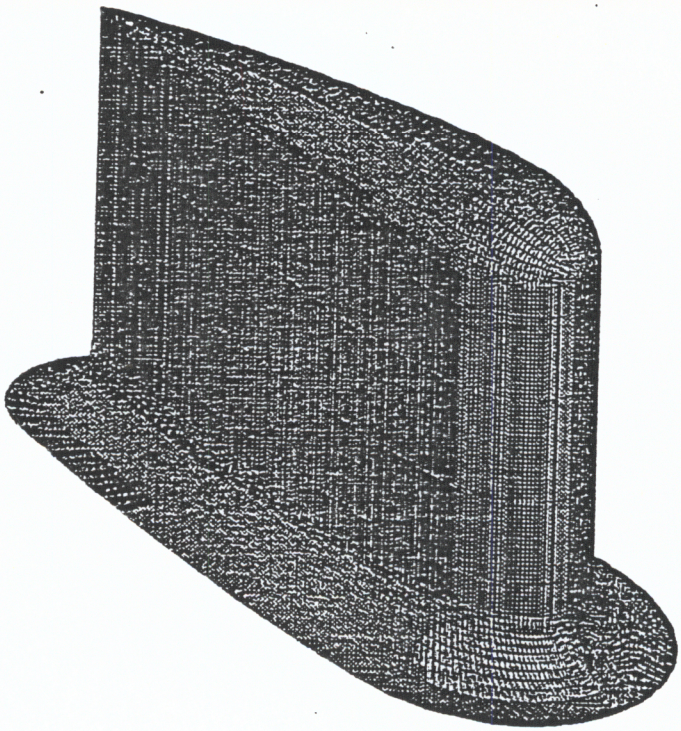

Figure 4. Wing with Fillet Model.

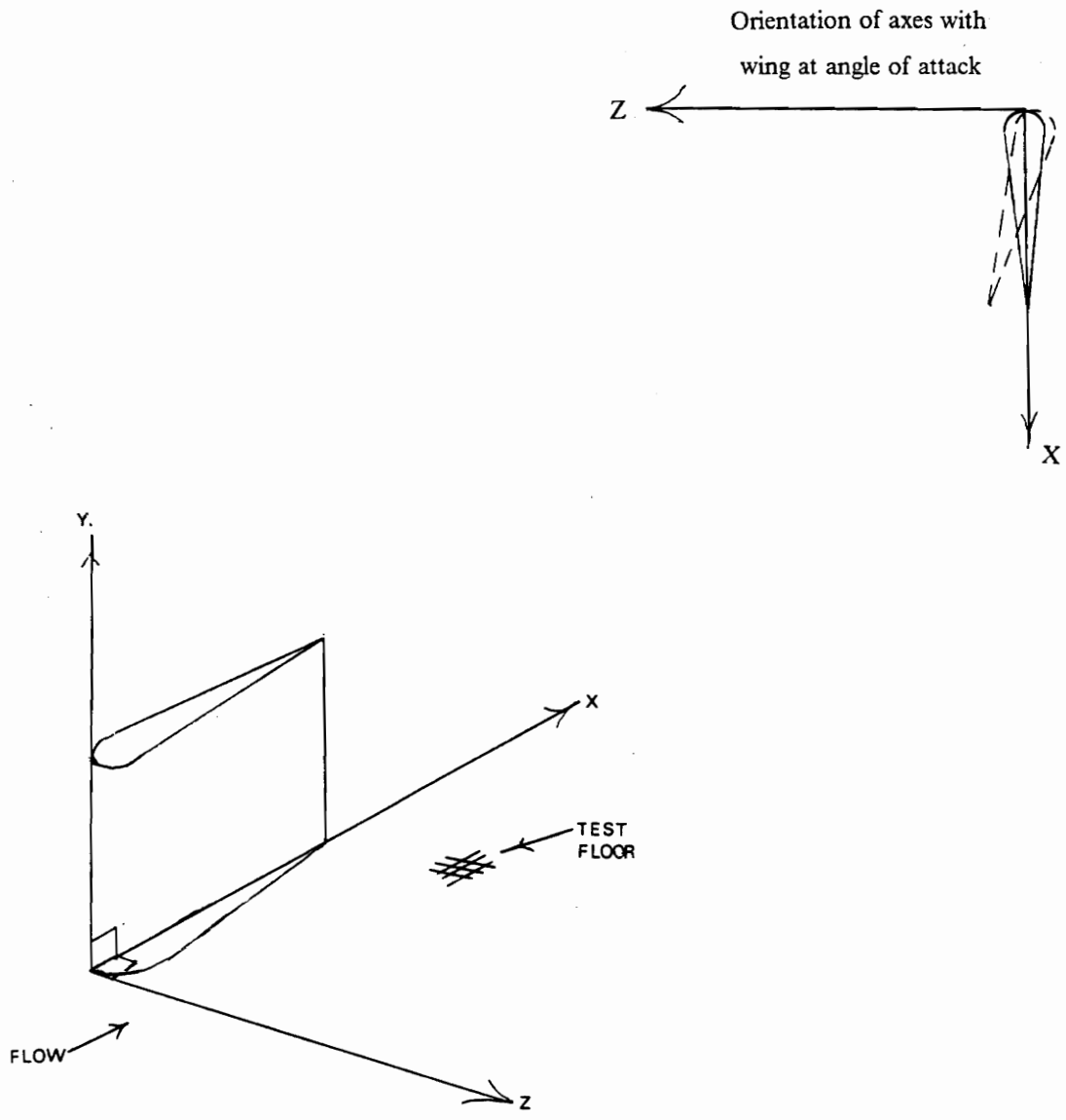

Figure 5. (X, Y, Z) Coordinate System.

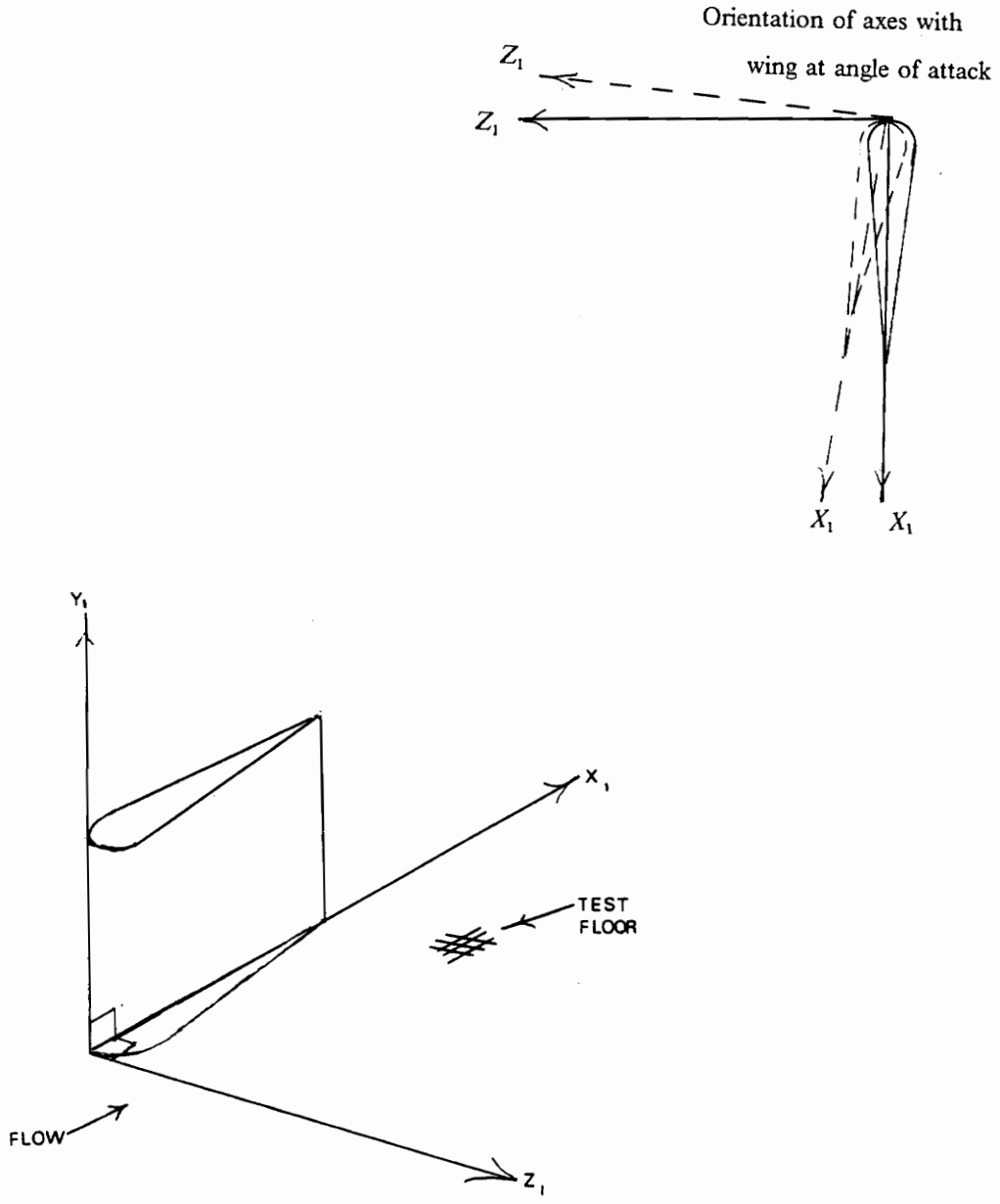

Figure 6. (X_1 , Y_1, Z_1) Coordinate System.

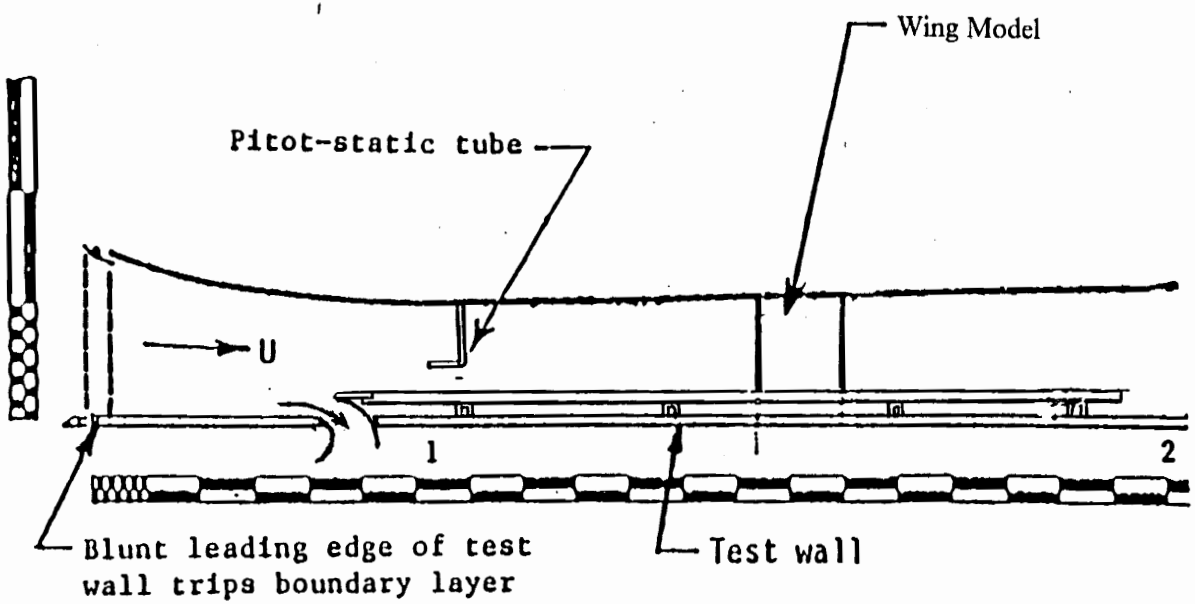

Figure 7. Side View of the Boundary-Layer Tunnel and Test Section with "False Floor" Installed.

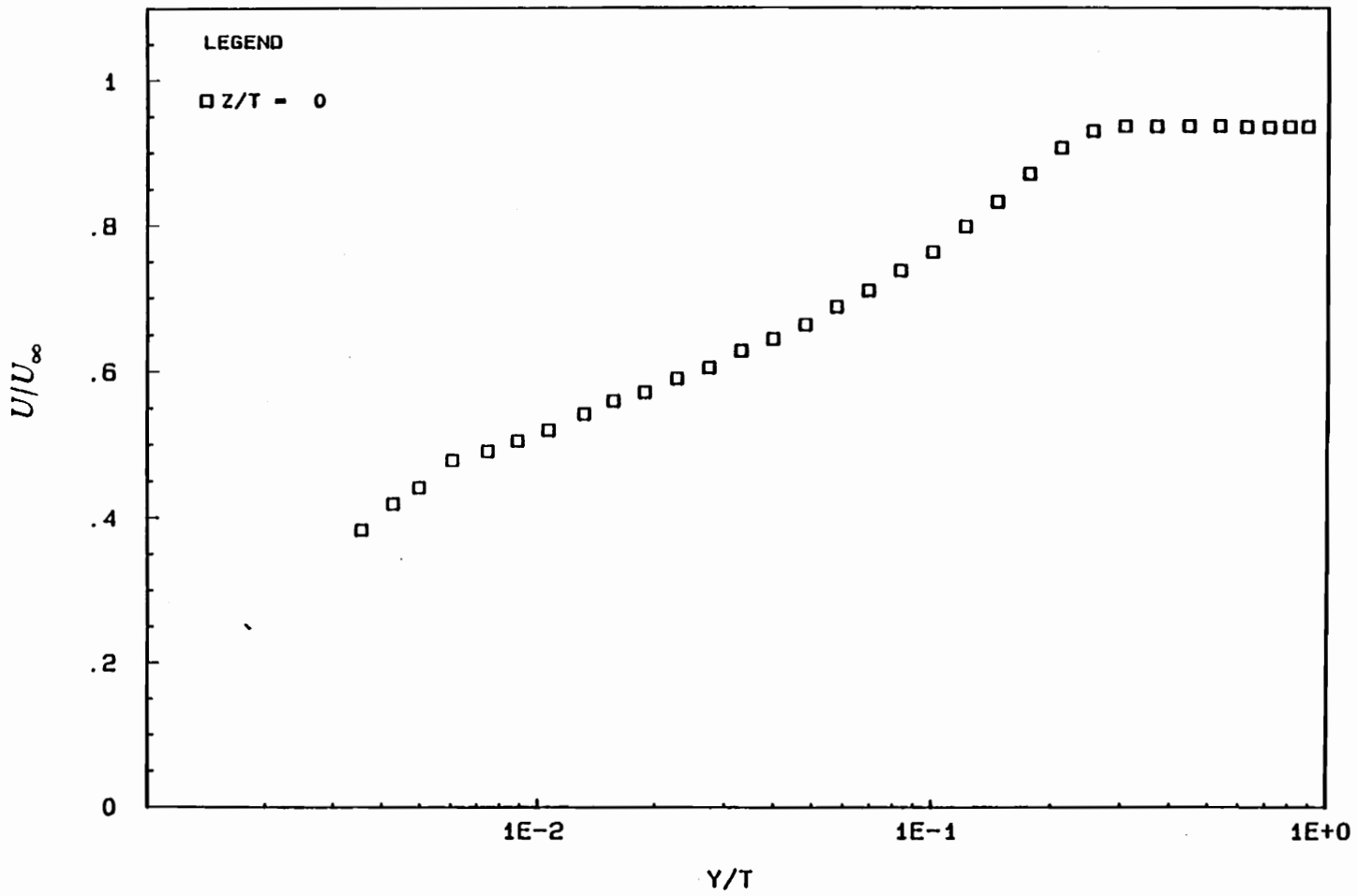

Figure 8. U/U_∞ Profile, Thin Boundary Layer, X/T = -2.15, Boundary-Layer Tunnel.

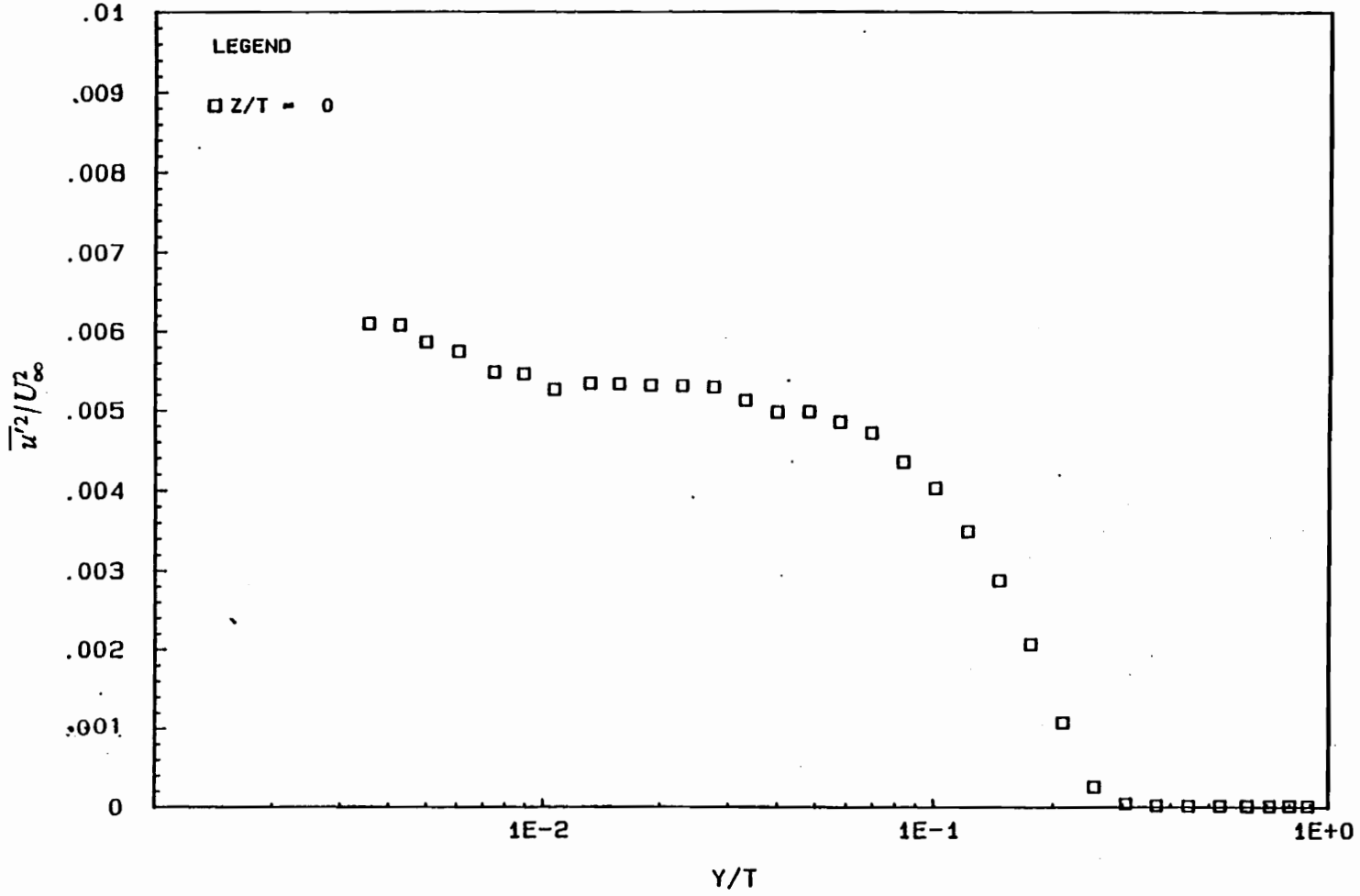

Figure 9. $\overline{u'^2}/U_\infty^2$ Profile, Thin Boundary Layer Case, X/T=-2.15, Boundary-Layer Tunnel.

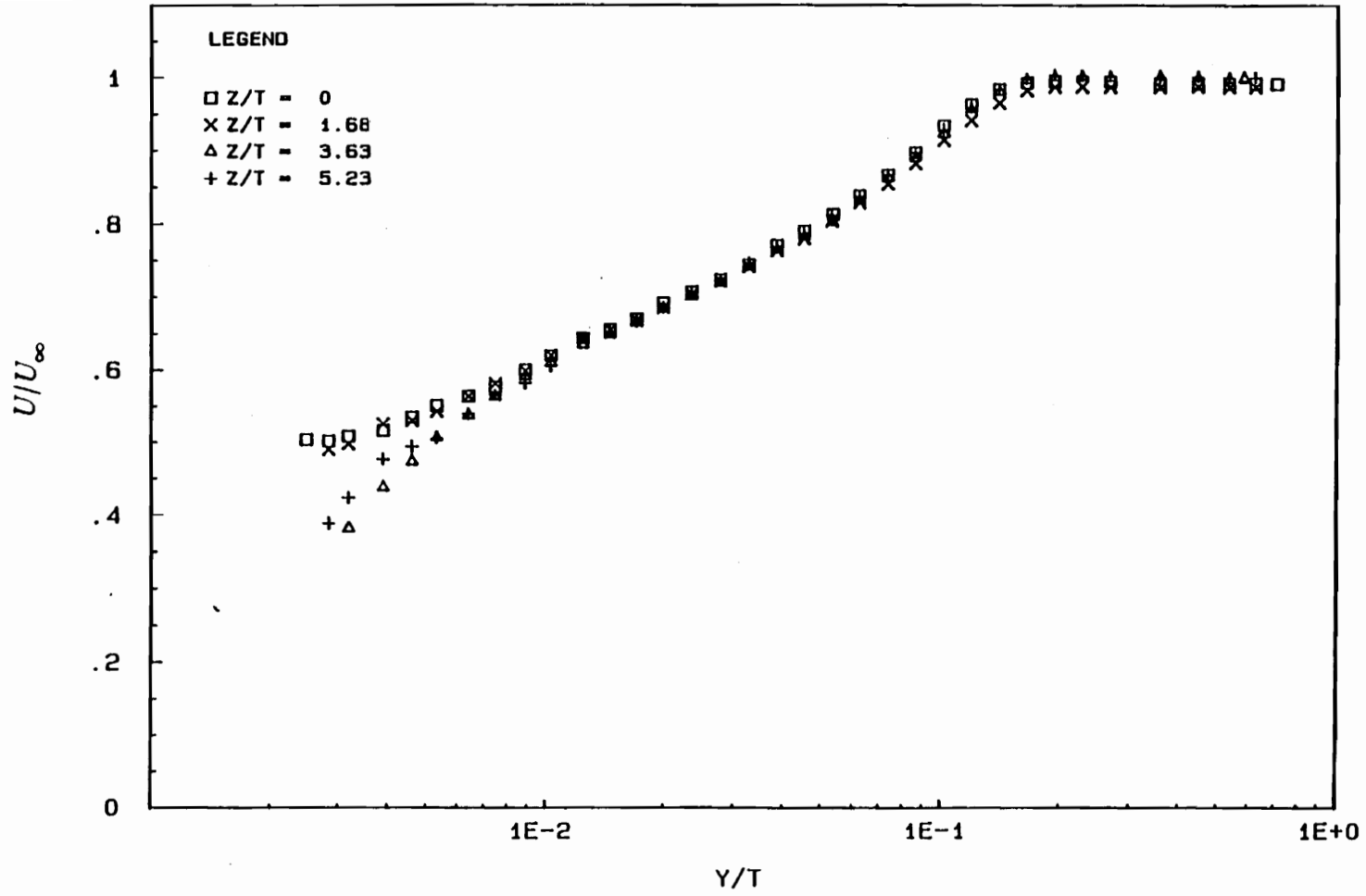

Figure 10. U/U_∞ Profiles at X/T = -9.47, Z/T = 0, 1.68, 3.63, and 5.23, Thin Boundary Layer, Boundary-Layer Tunnel.

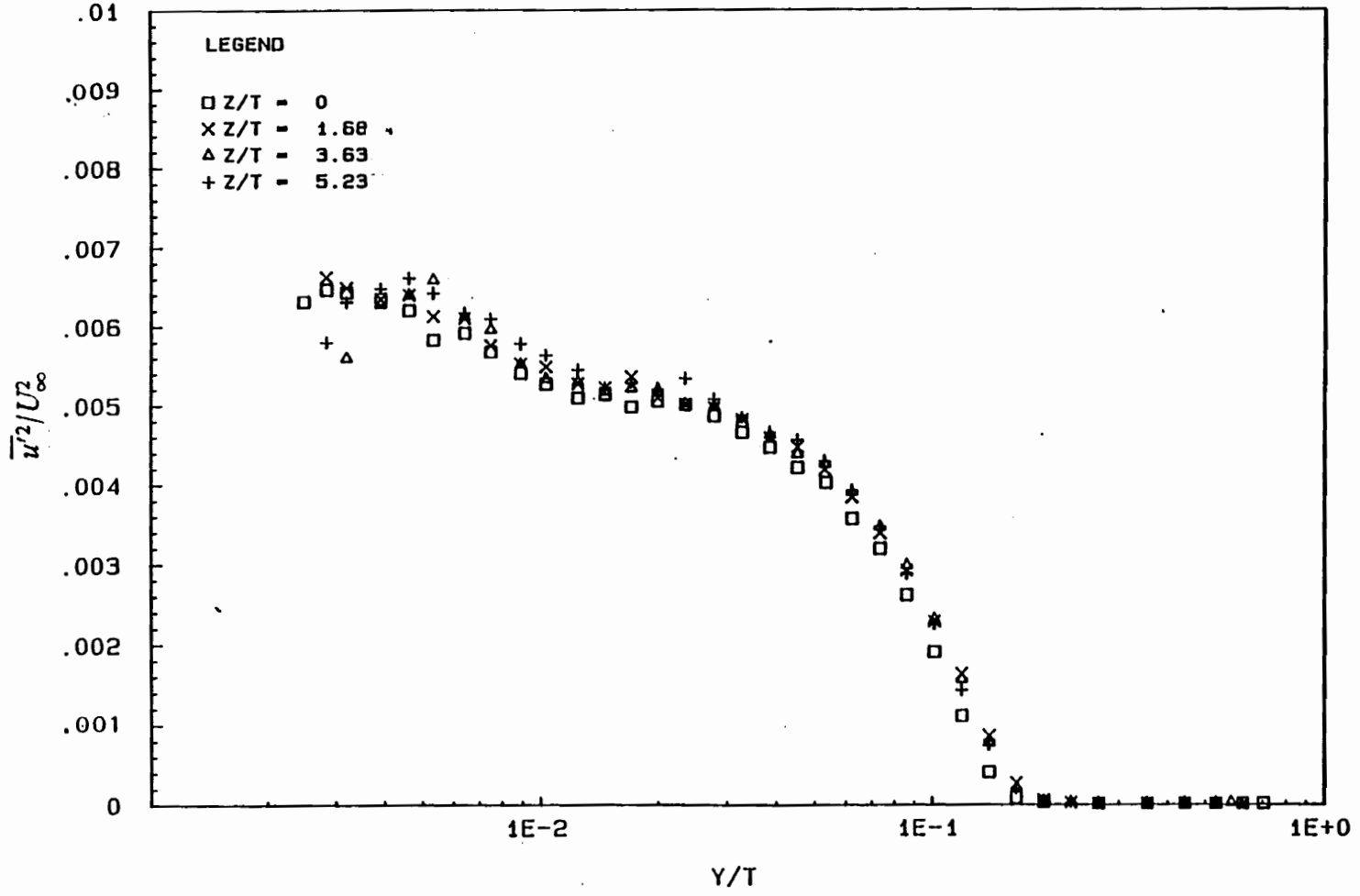

Figure 11. $\overline{u'^2}/U_\infty^2$ Profiles at X/T = -9.47, Z/T = 0, 1.68, 3.63, 5.23, Thin Boundary Layer, Boundary-Layer Tunnel.

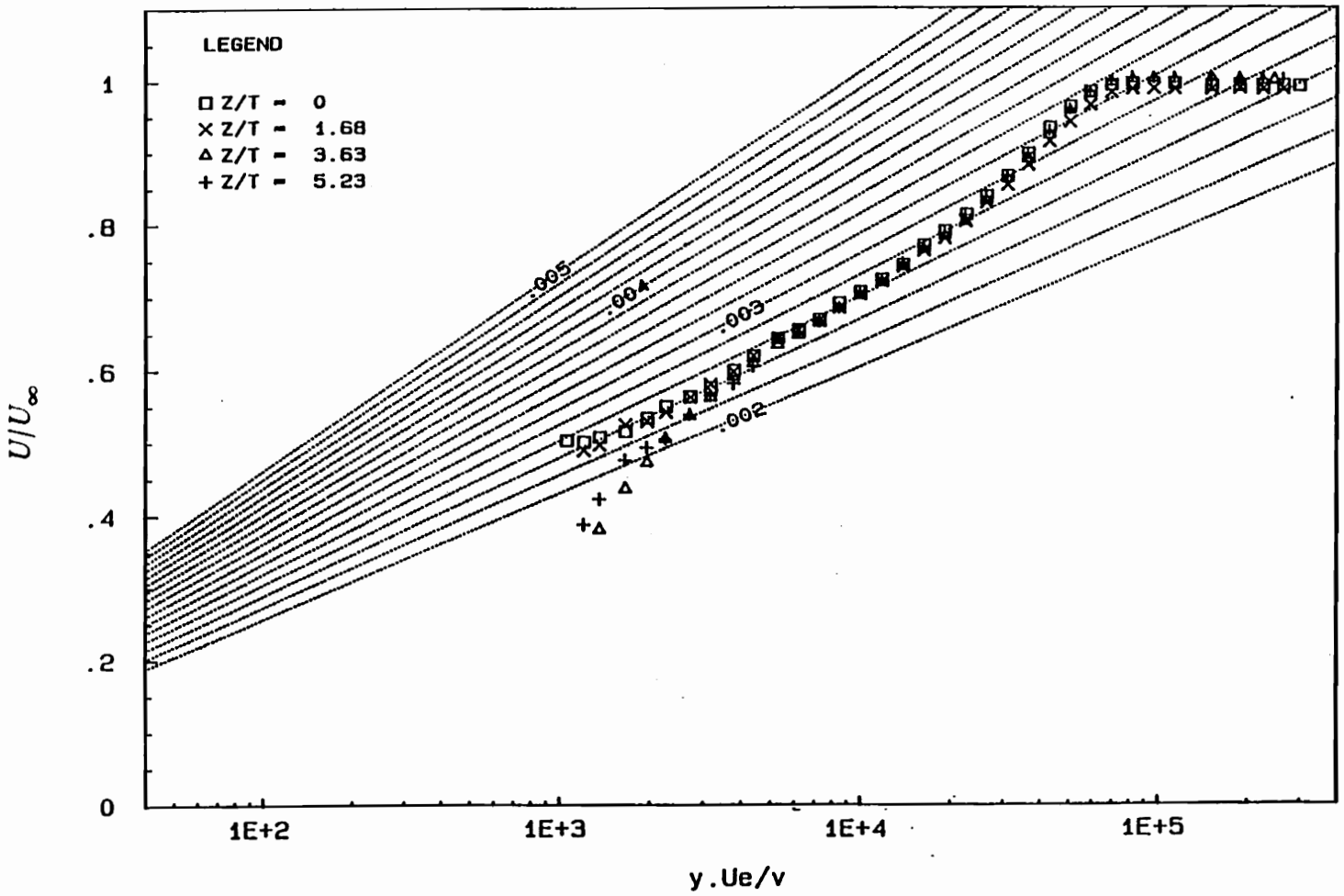

Figure 12. Clauser Plot of the U/U_∞ Profiles at X/T = -9.47, Z/T = 0, 1.68, 3.63, and 5.23, Thin Boundary Layer, Boundary-Layer Tunnel.

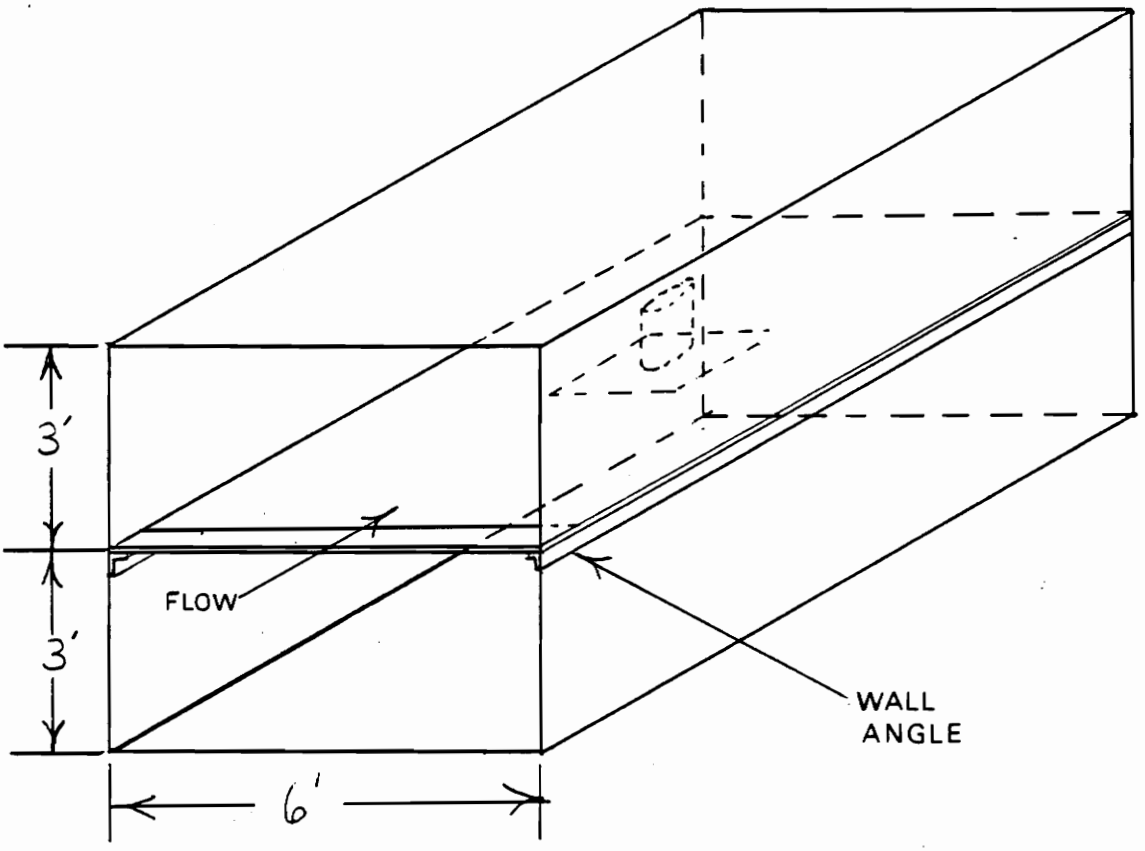

Figure 13. Perspective View of Stability Wind Tunnel Test Section with "False Floor" Installed.

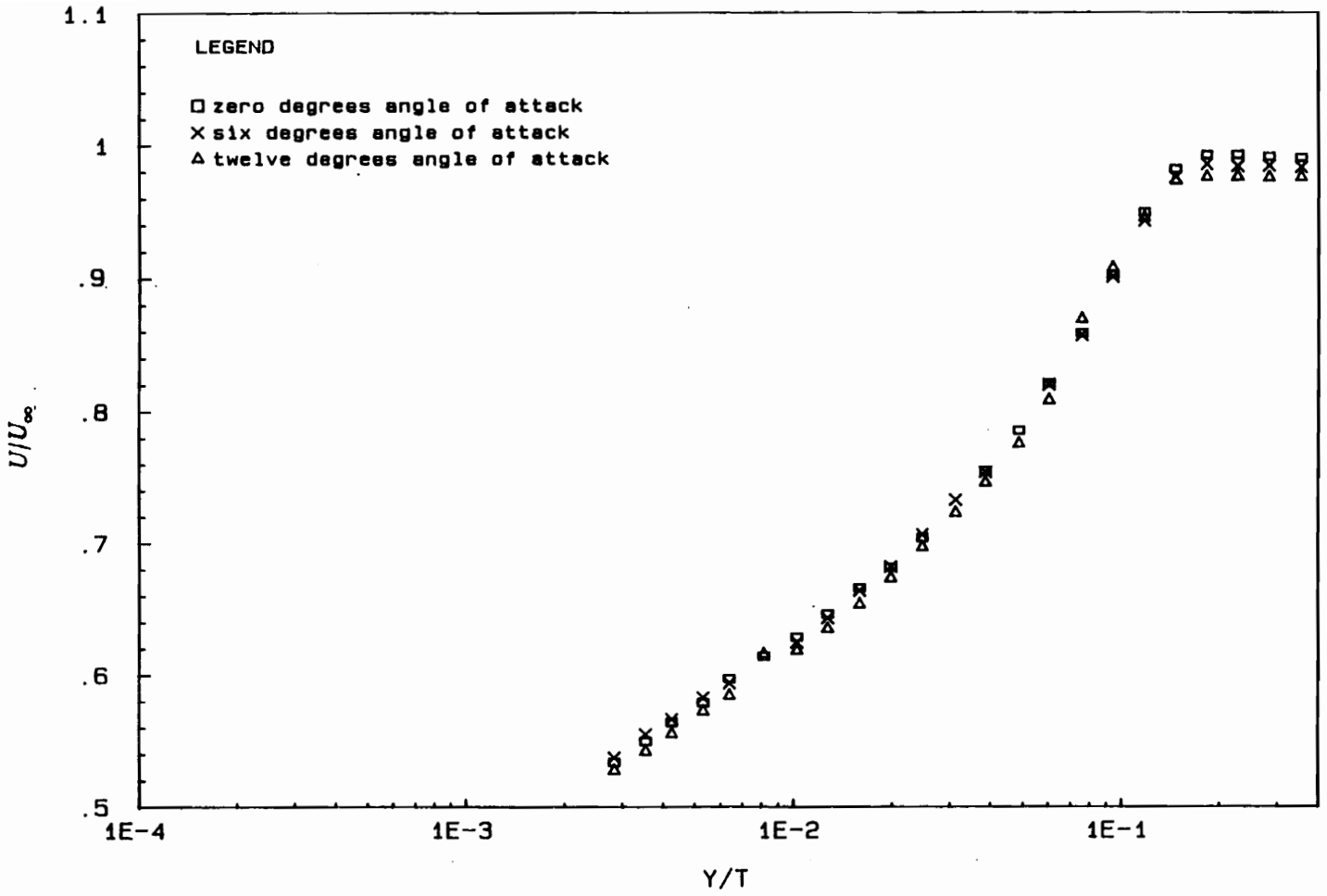

Figure 14. U/U_∞ Profiles, Baseline Wing, Thin Boundary Layer, X/T=-9.56, Stability Wind Tunnel.

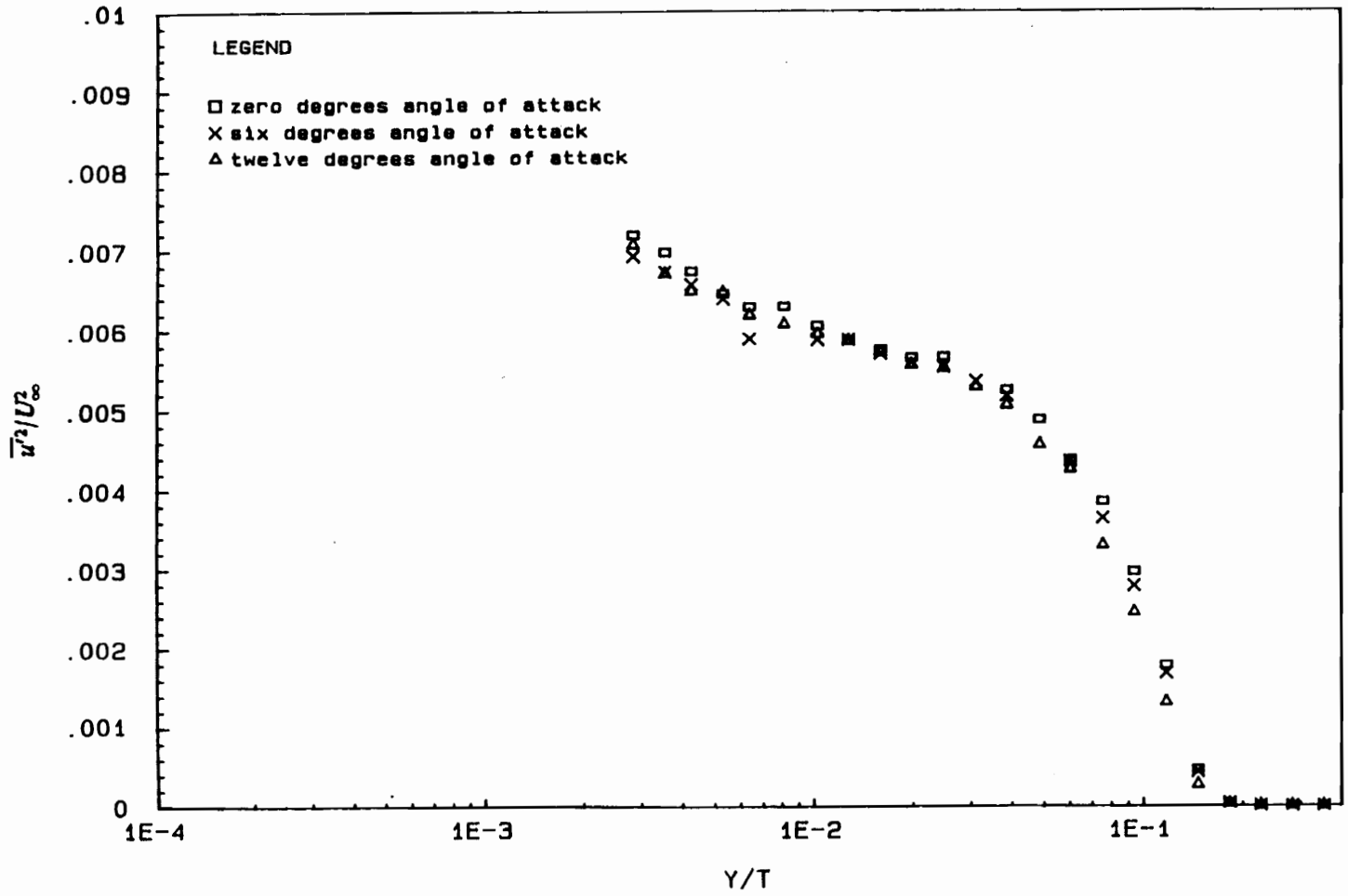

Figure 15. $\overline{u'^2}/U_\infty^2$ Profiles, Baseline Wing, Thin Boundary Layer, X/T = -9.56, Stability Wind Tunnel.

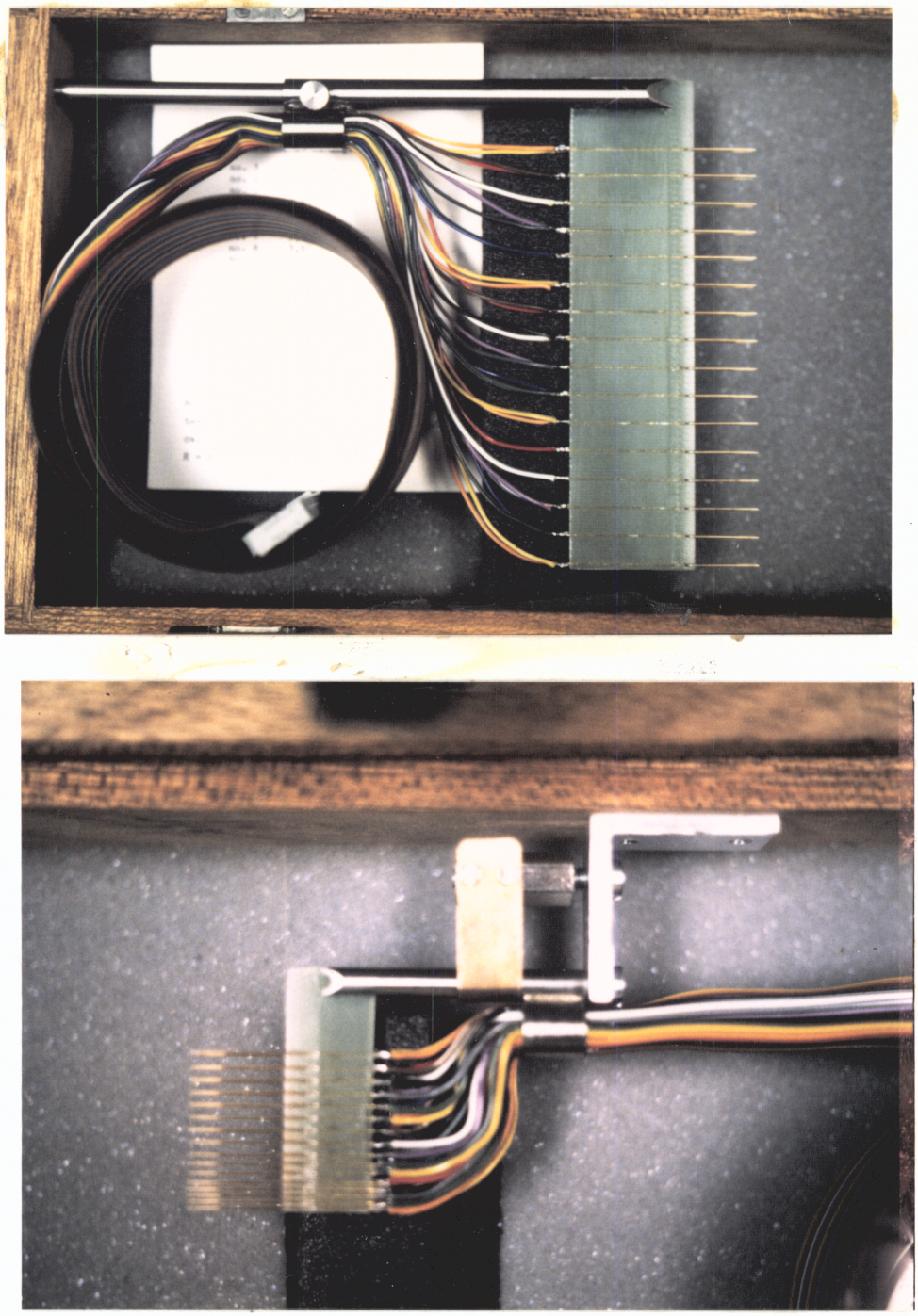

Figure 16. Photographs of the Big Hot-Wire Rake (top), and the Small Hot-Wire Rake (bottom).

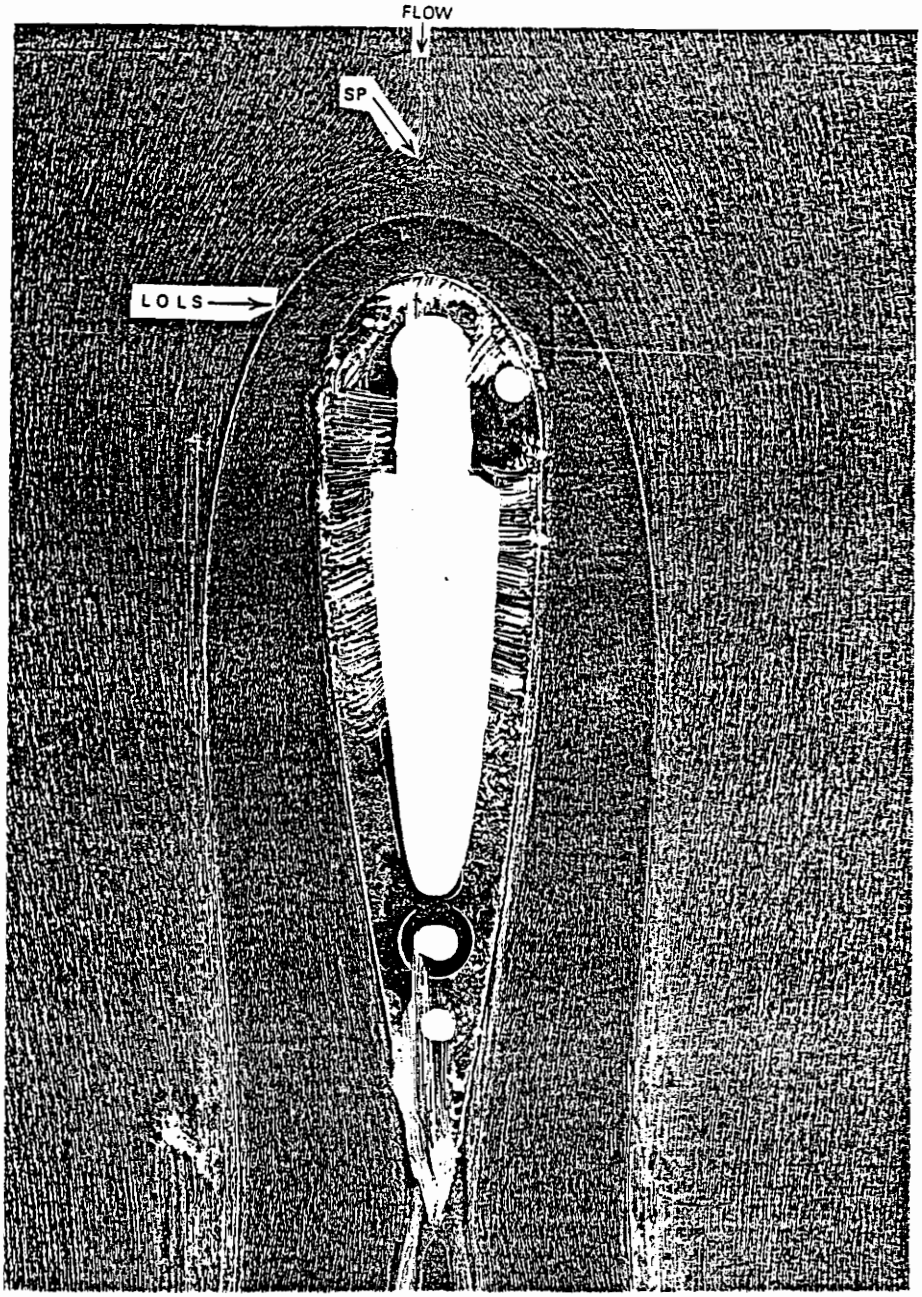

Figure 17. Oil-Flow Visualization of Floor Surrounding Baseline Wing at 0 Degrees Angle of Attack, Thin Boundary Layer, Boundary-Layer Tunnel, LOLS = Line of Low Shear, SP = Saddle Point.

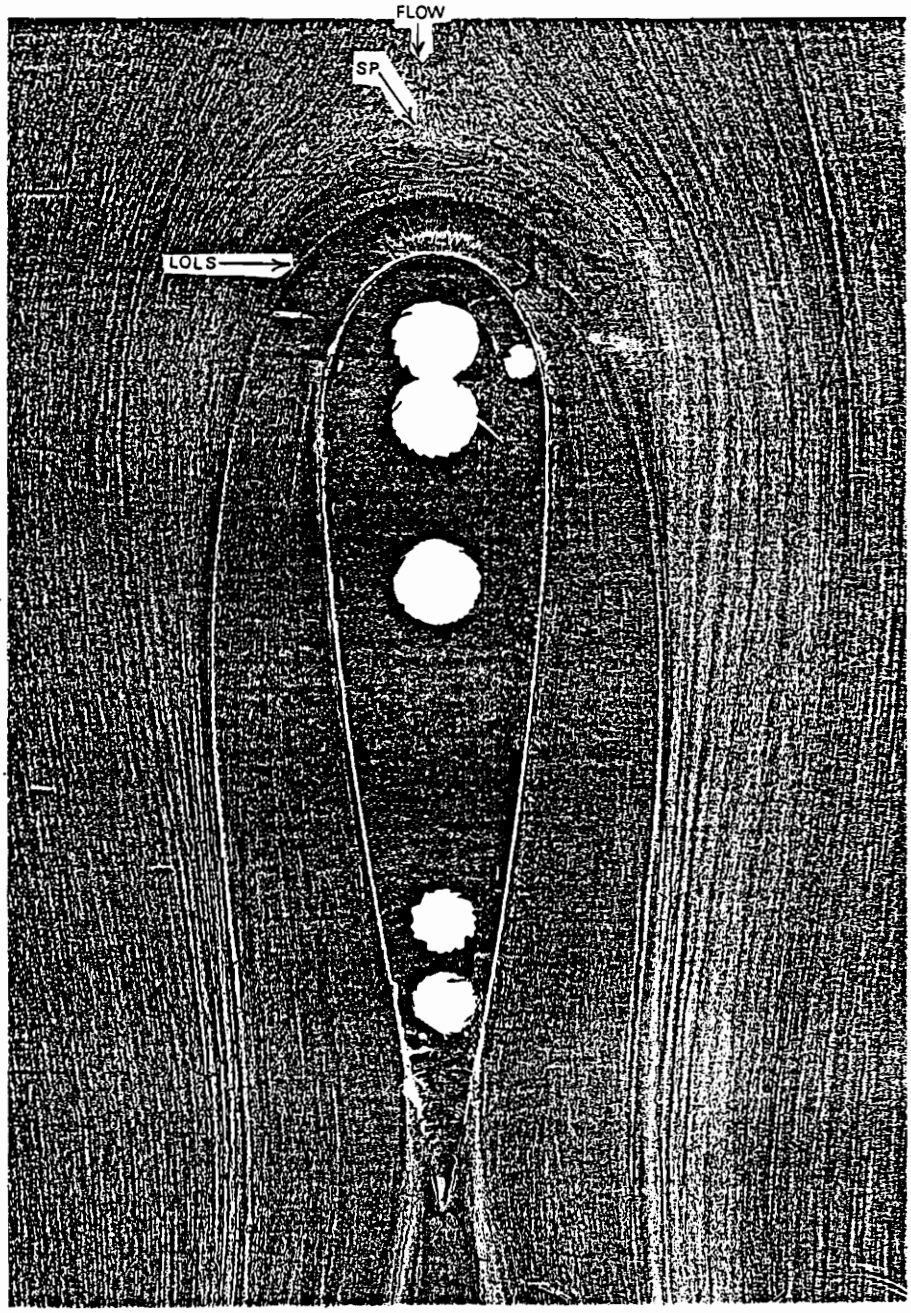

Figure 18. Oil-Flow Visualization of Floor Surrounding Baseline Wing at 0 Degrees Angle of Attack, Thick Boundary Layer, Boundary-Layer Tunnel, LOLS = Line of Low Shear, SP = Saddle Point.

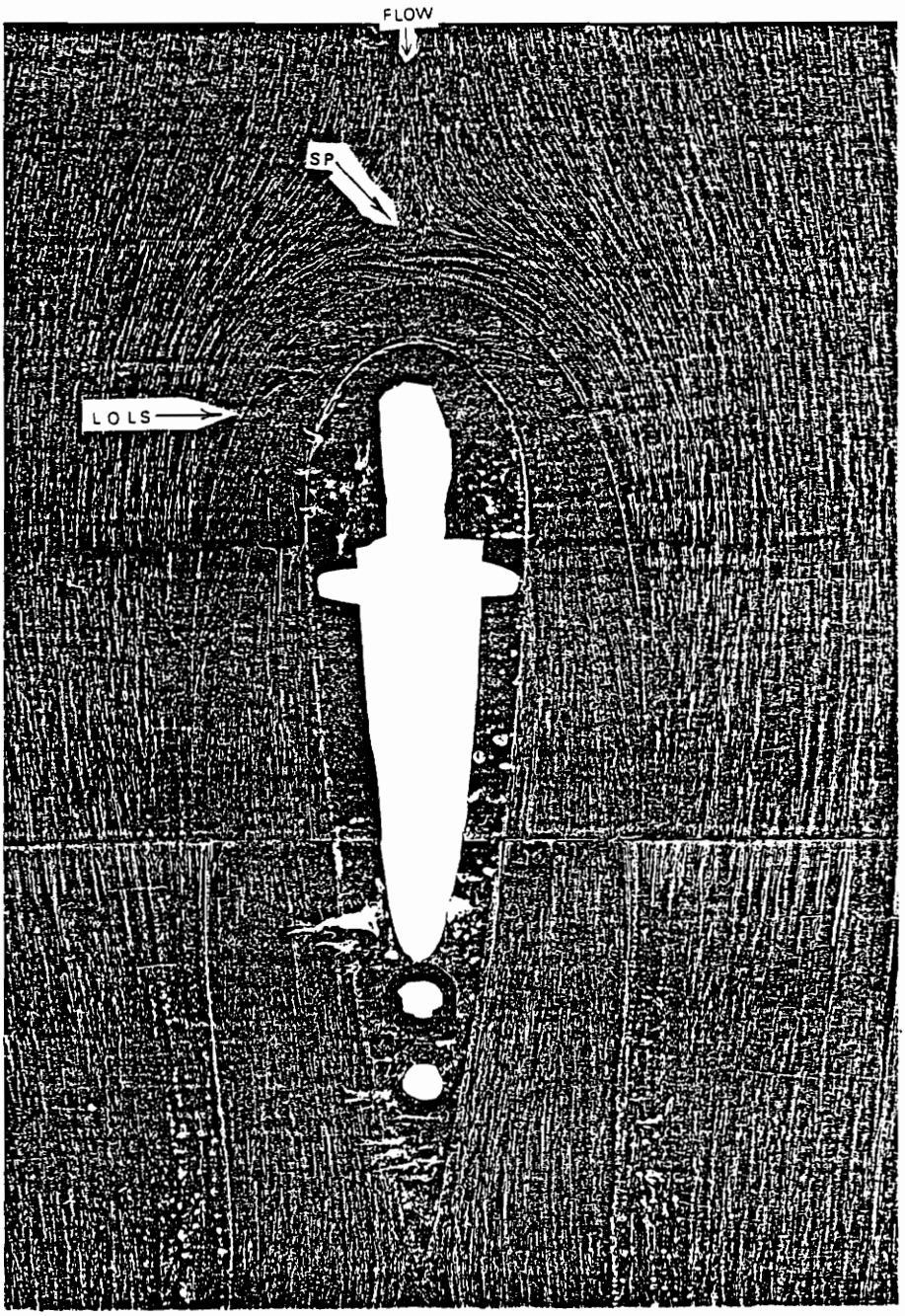

Figure 19. Oil-Flow Visualization of Floor Surrounding Baseline Wing at 0 Degrees Angle of Attack, Thin Boundary Layer, Stability Wind Tunnel, LOLS = Line of Low Shear, SP = Saddle Point.

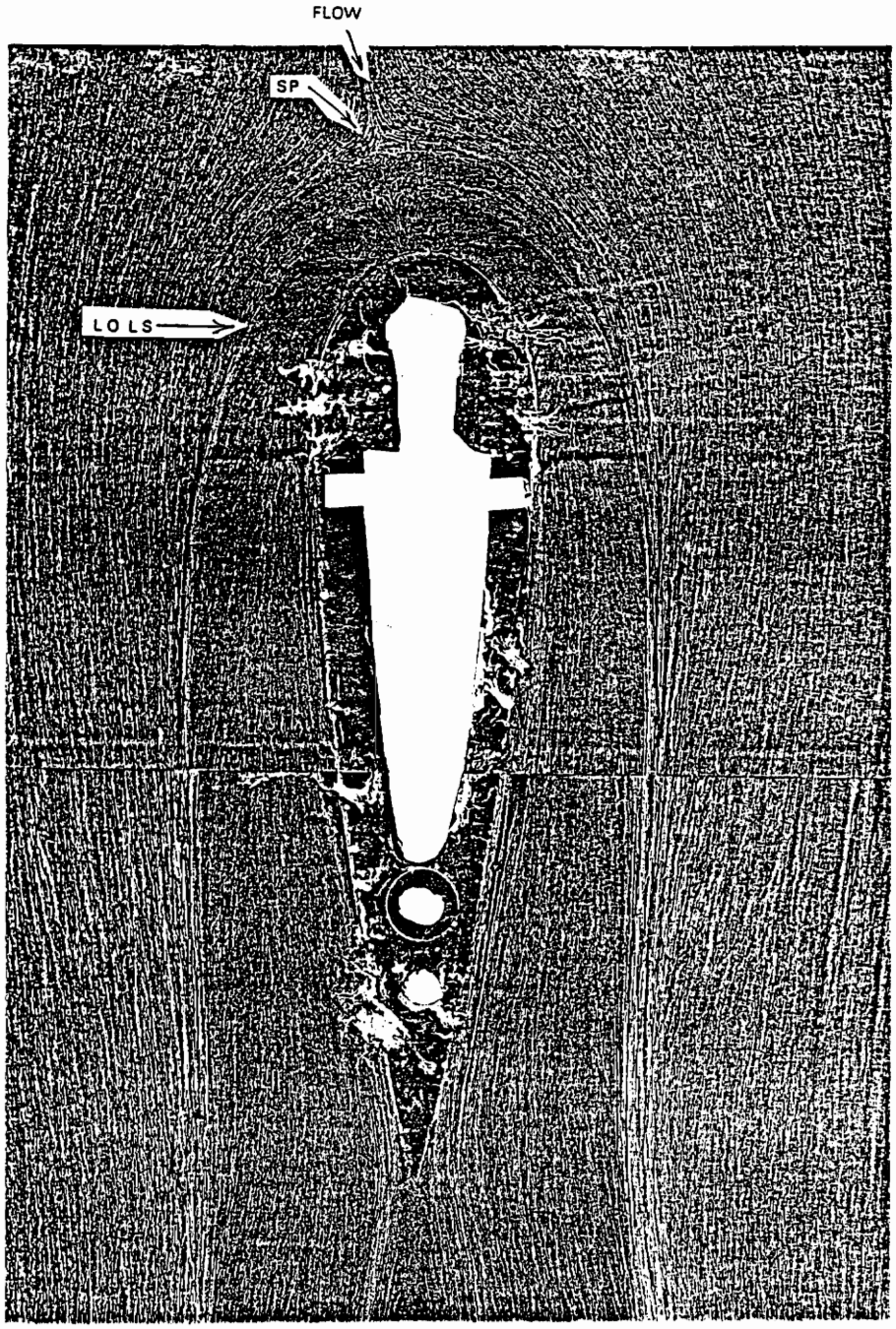

Figure 20. Oil-Flow Visualization of Floor Surrounding Baseline Wing at 6 Degrees Angle of Attack, Thin Boundary Layer, Stability Wind Tunnel, LOLS = Line of Low Shear, SP = Saddle Point.

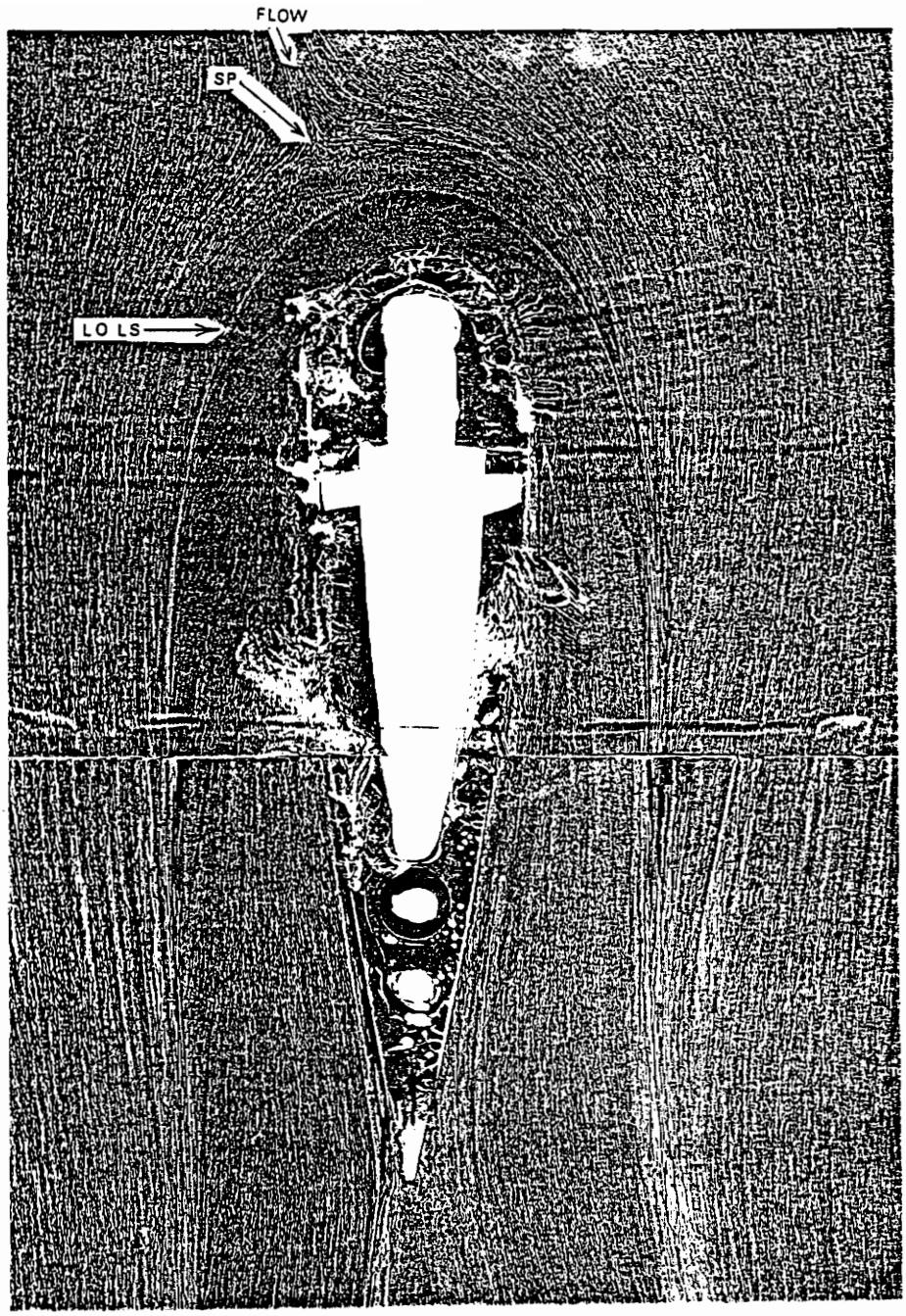

Figure 21. Oil-Flow Visualization of Floor Surrounding Baseline Wing at 12 Degrees Angle of Attack, Thin Boundary Layer, Stability Wind Tunnel, LOLS = Line of Low Shear, SP = Saddle Point.

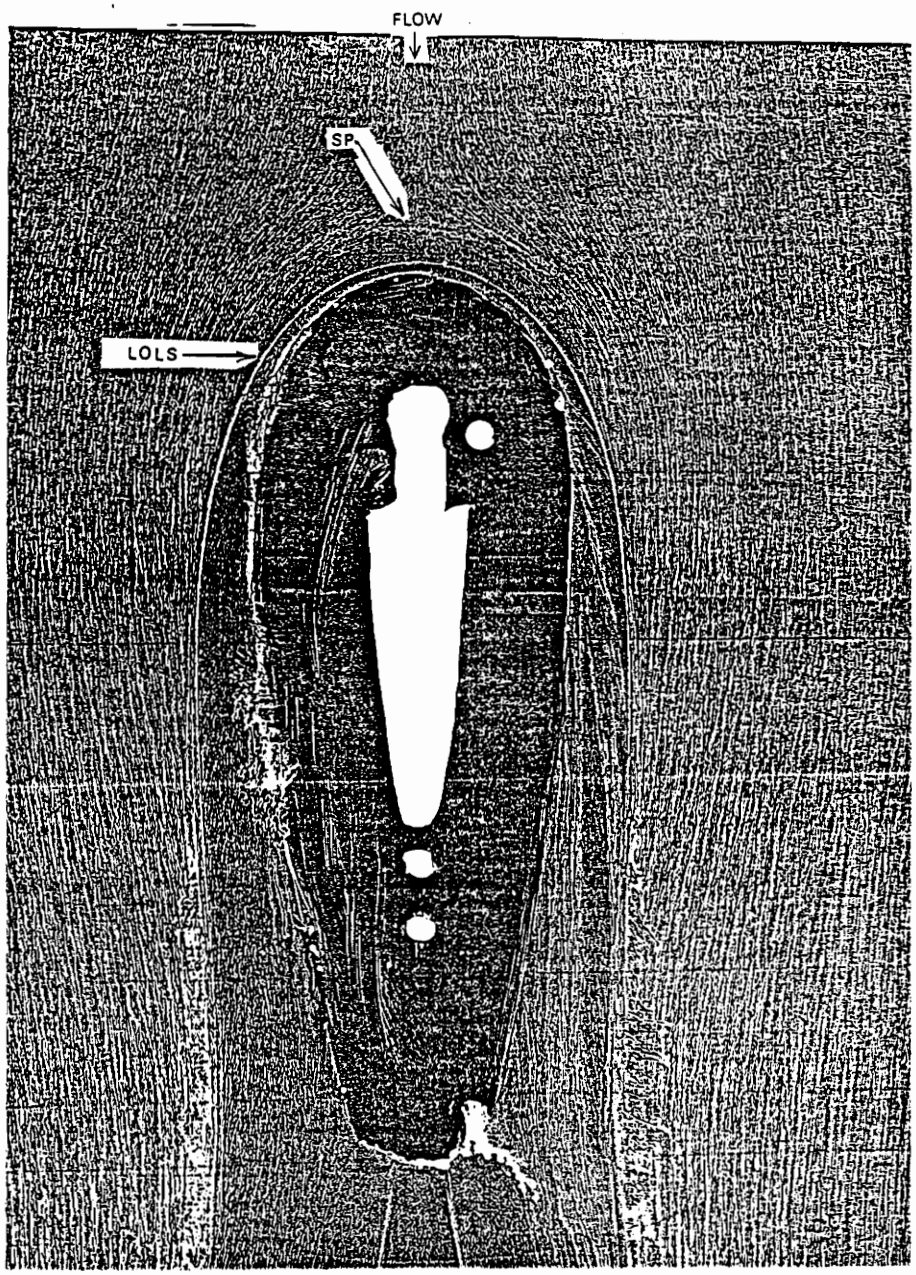

Figure 22. Oil-Flow Visualization of Floor Surrounding Wing with Fillet at 0 Degrees Angle of Attack, Thin Boundary Layer, Boundary-Layer Tunnel, LOLS = Line of Low Shear, SP = Saddle Point.

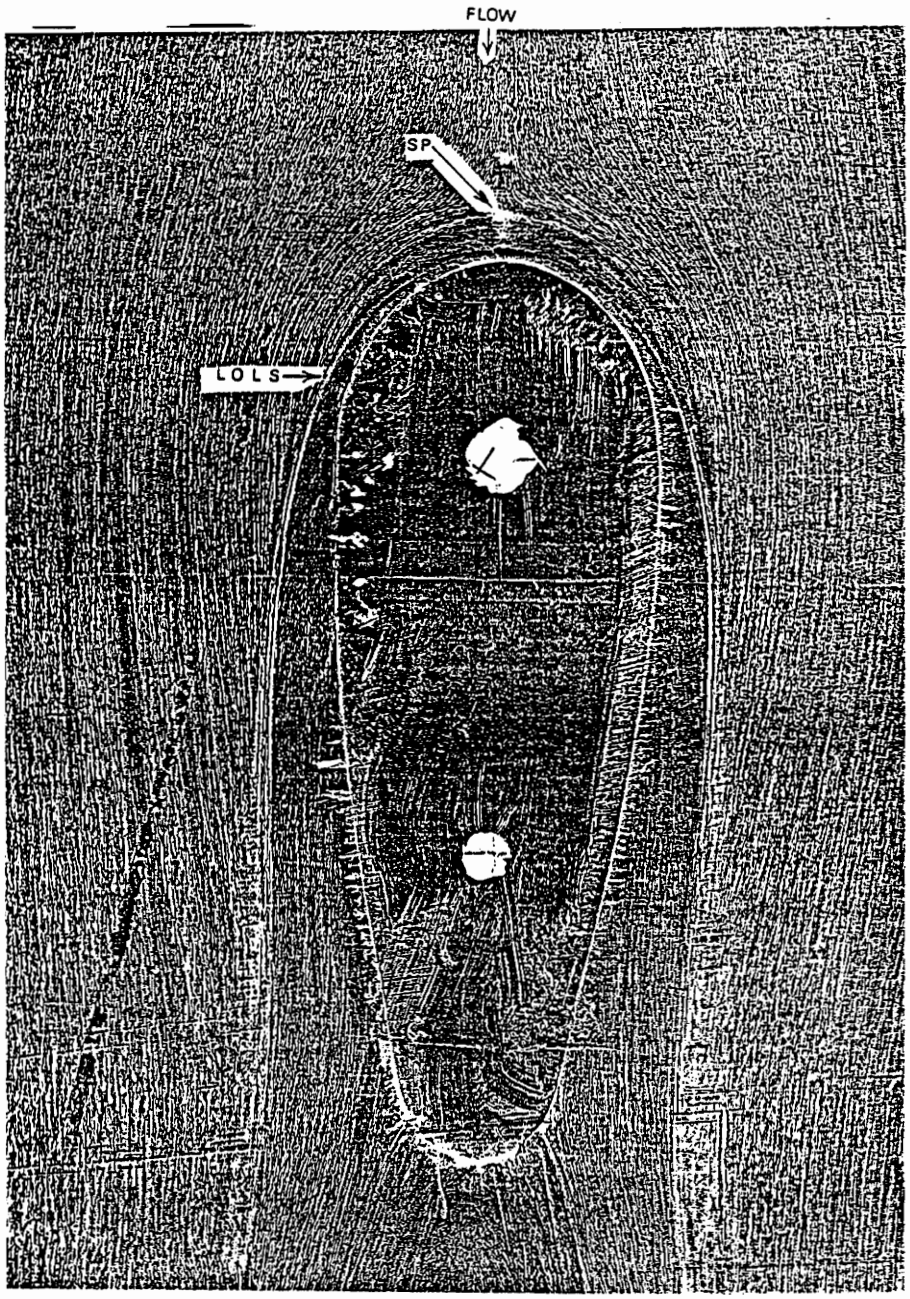

Figure 23. Oil-Flow Visualization of Floor Surrounding Wing with Fillet at 0 Degrees Angle of Attack, Thick Boundary Layer, Boundary-Layer Tunnel, LOLS = Line of Low Shear, SP = Saddle Point.

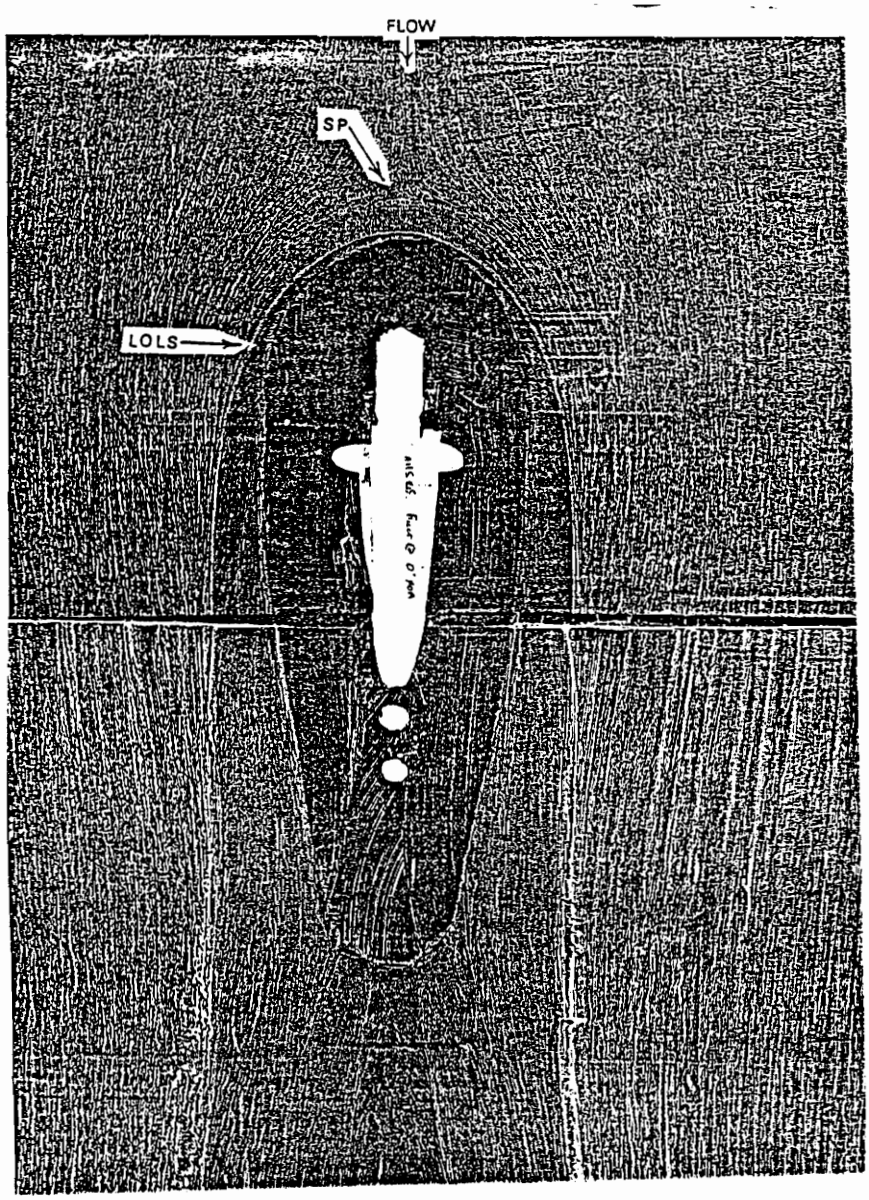

Figure 24. Oil-Flow Visualization of Floor Surrounding Wing with Fillet at 0 Degrees Angle of Attack, Thin Boundary Layer, Stability Wind Tunnel, LOLS = Line of Low Shear, SP = Saddle Point.

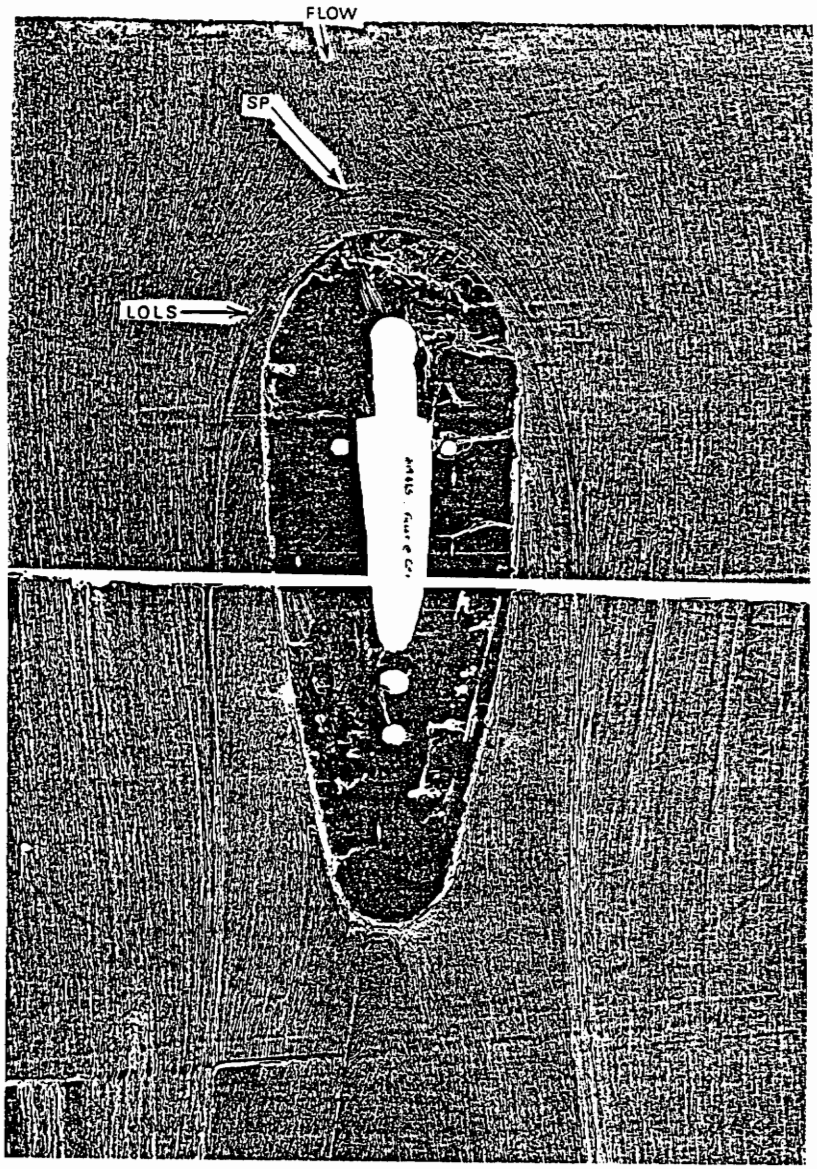

Figure 25. Oil-Flow Visualization of Floor Surrounding Wing with Fillet at 6 Degrees Angle of Attack, Thin Boundary Layer, Stability Wind Tunnel, LOLS = Line of Low Shear, SP = Saddle Point.

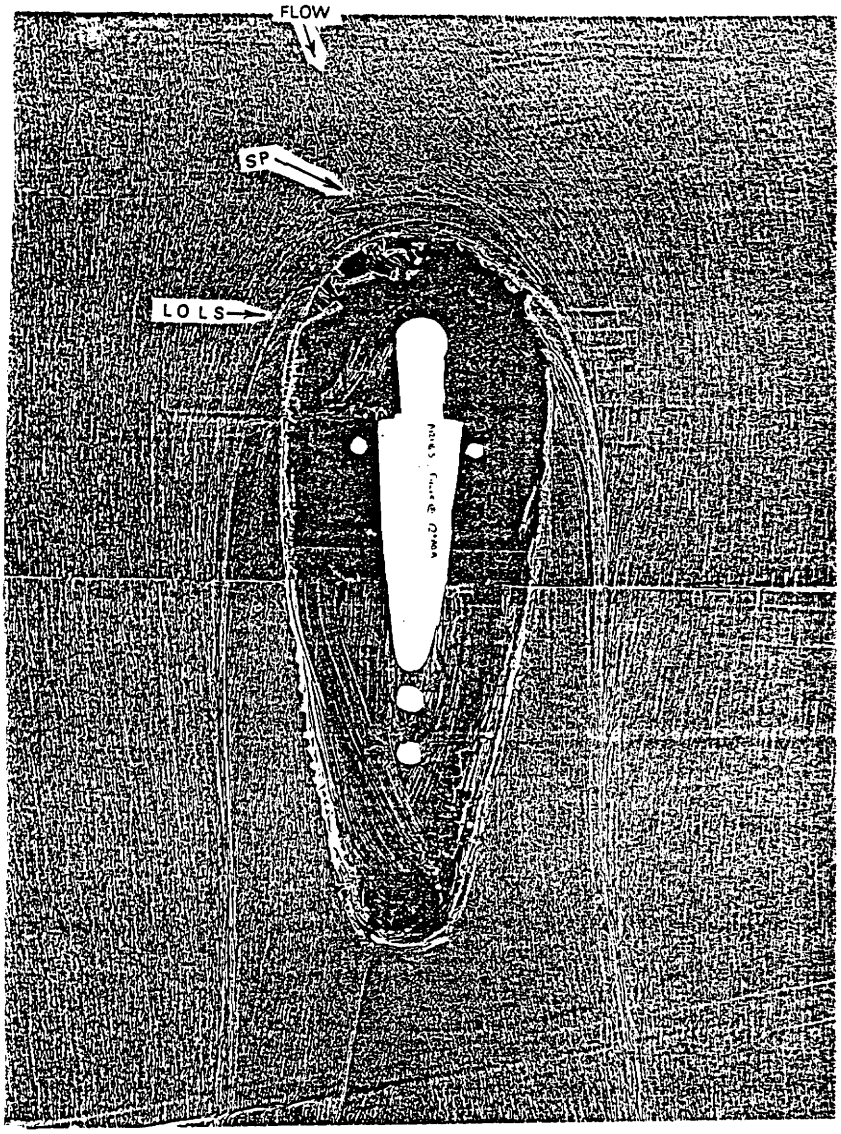

Figure 26. Oil-Flow Visualization of Floor Surrounding Wing with Fillet at 12 Degrees Angle of Attack, Thin Boundary Layer, Stability Wind Tunnel, LOLS = Line of Low Shear, SP = Saddle Point.

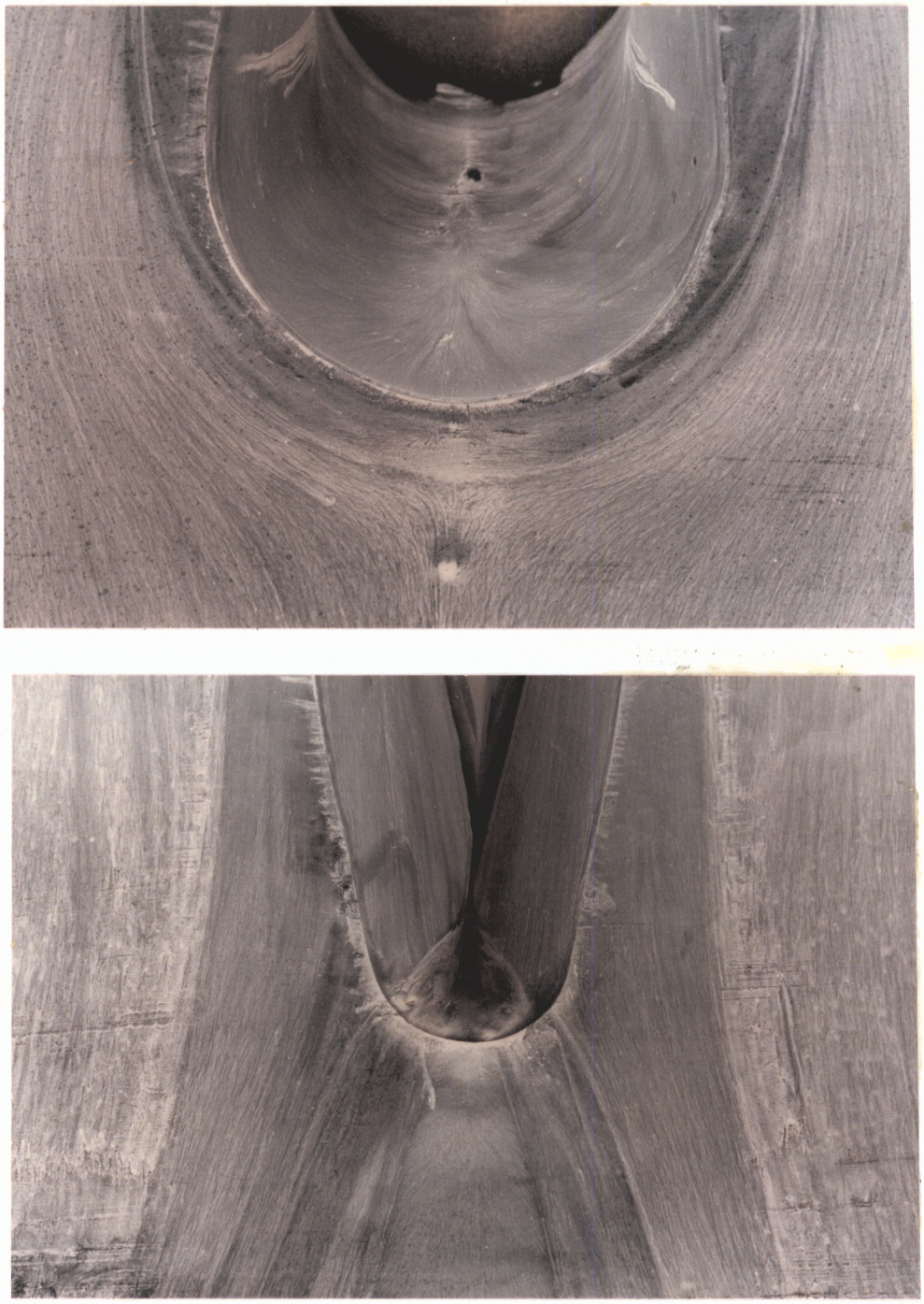

Figure 27. Photographs of the Nose Region (top), and Trailing Edge Region (bottom), Wing with Fillet at 0 Degrees Angle of Attack, Thick Boundary Layer, Boundary-Layer Tunnel.

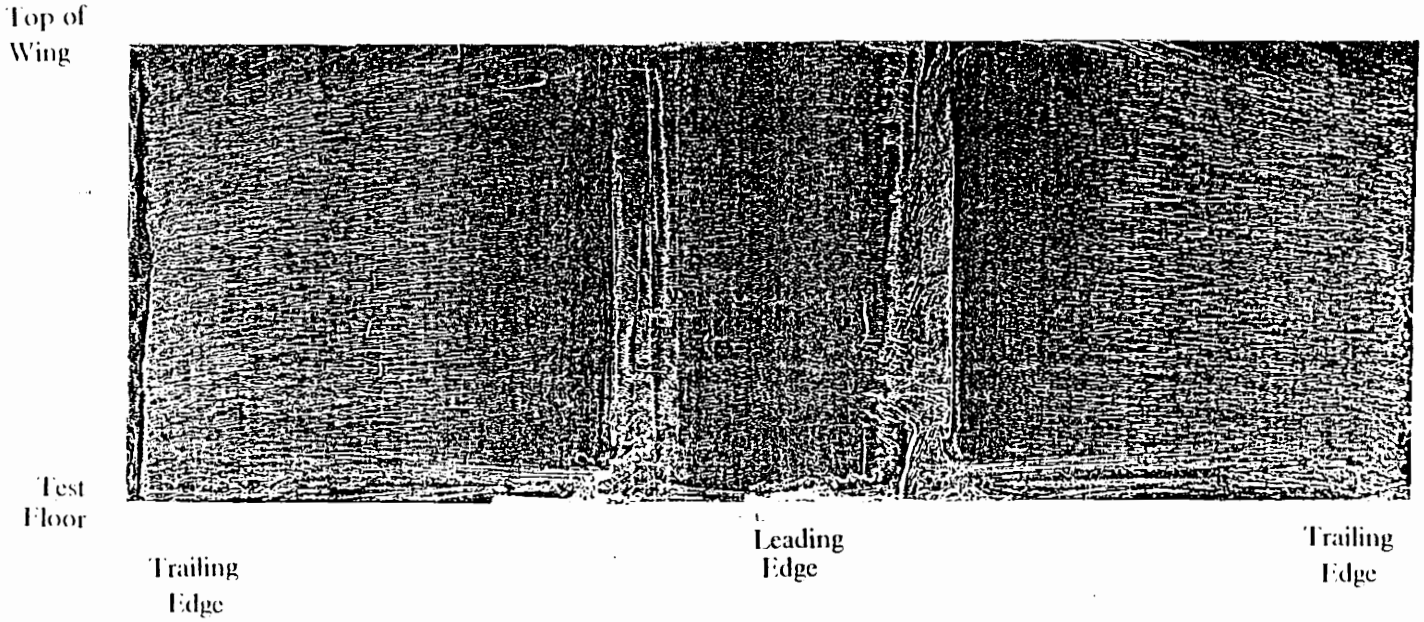

Figure 28. Oil-Flow Visualization on the Baseline Wing at 0 Degrees Angle of Attack, Thin Boundary Layer, Stability Wind Tunnel.

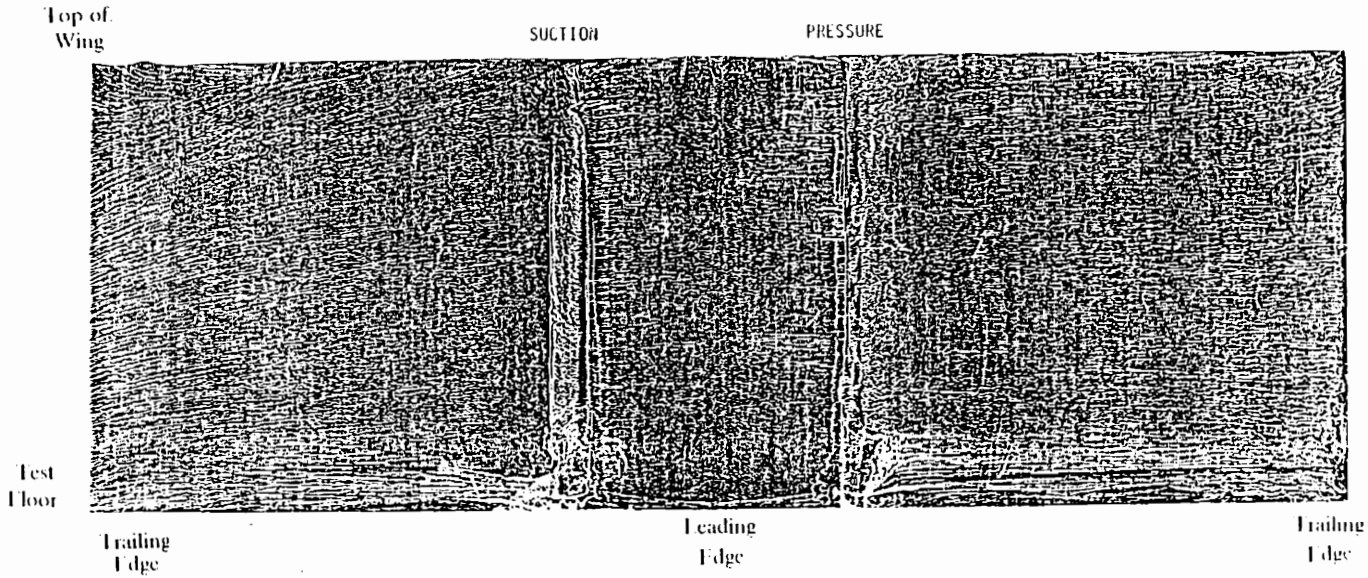

Figure 29. Oil-Flow Visualization on the Baseline Wing at 6 Degrees Angle of Attack, Thin Boundary Layer, Stability Wind Tunnel.

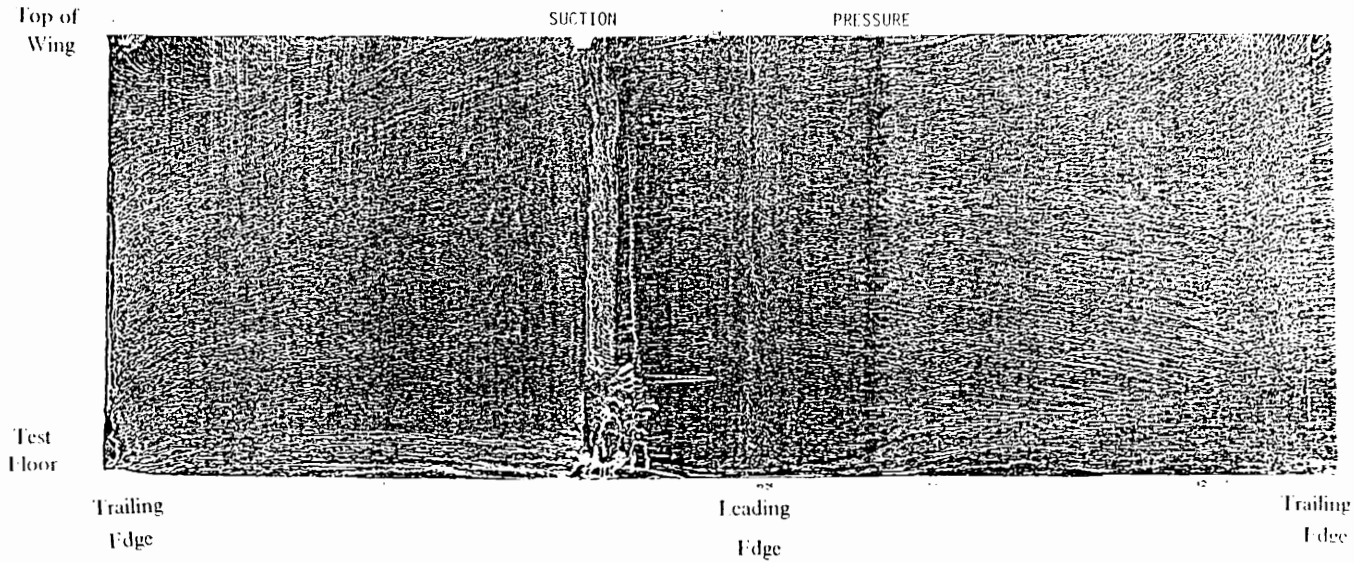

Figure 30. Oil-Flow Visualization on the Baseline Wing at 12 Degrees Angle of Attack, Thin Boundary Layer, Stability Wind Tunnel.

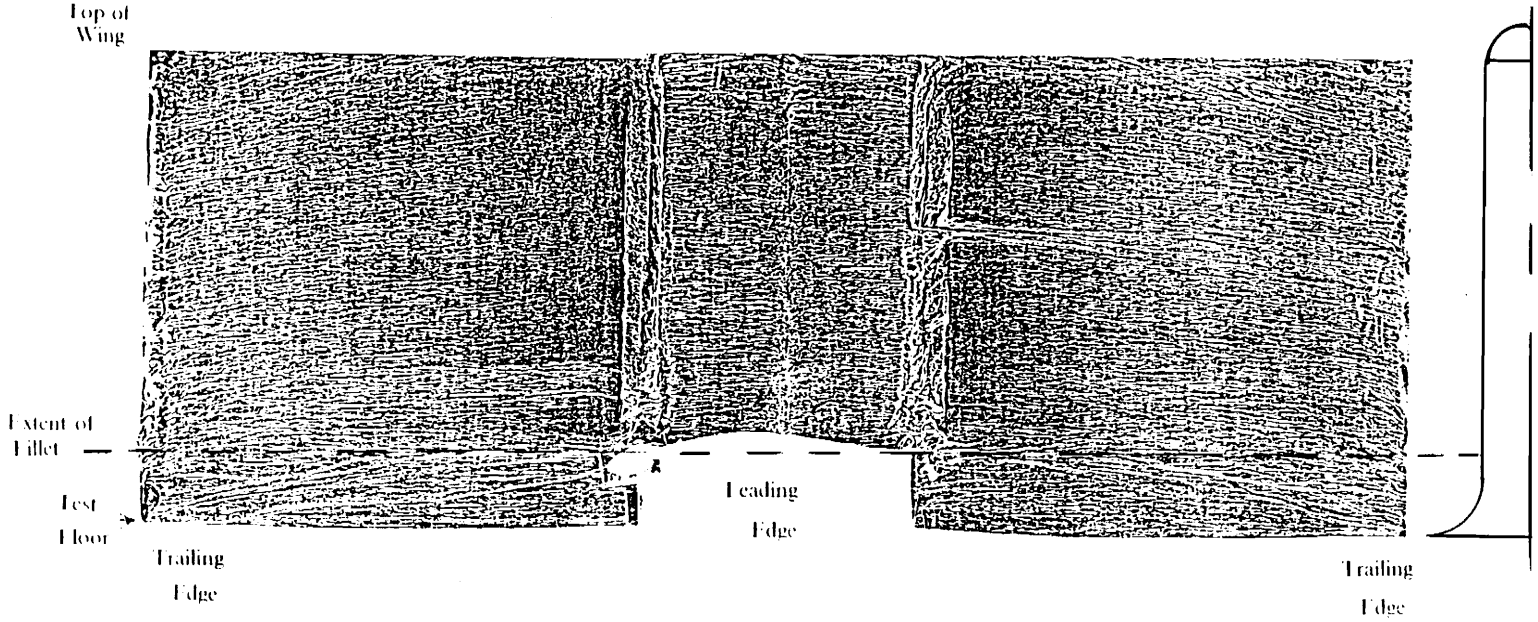

Figure 31. Oil-Flow Visualization on the Wing with Fillet at 0 Degrees Angle of Attack, Thin Boundary Layer, Stability Wind Tunnel.

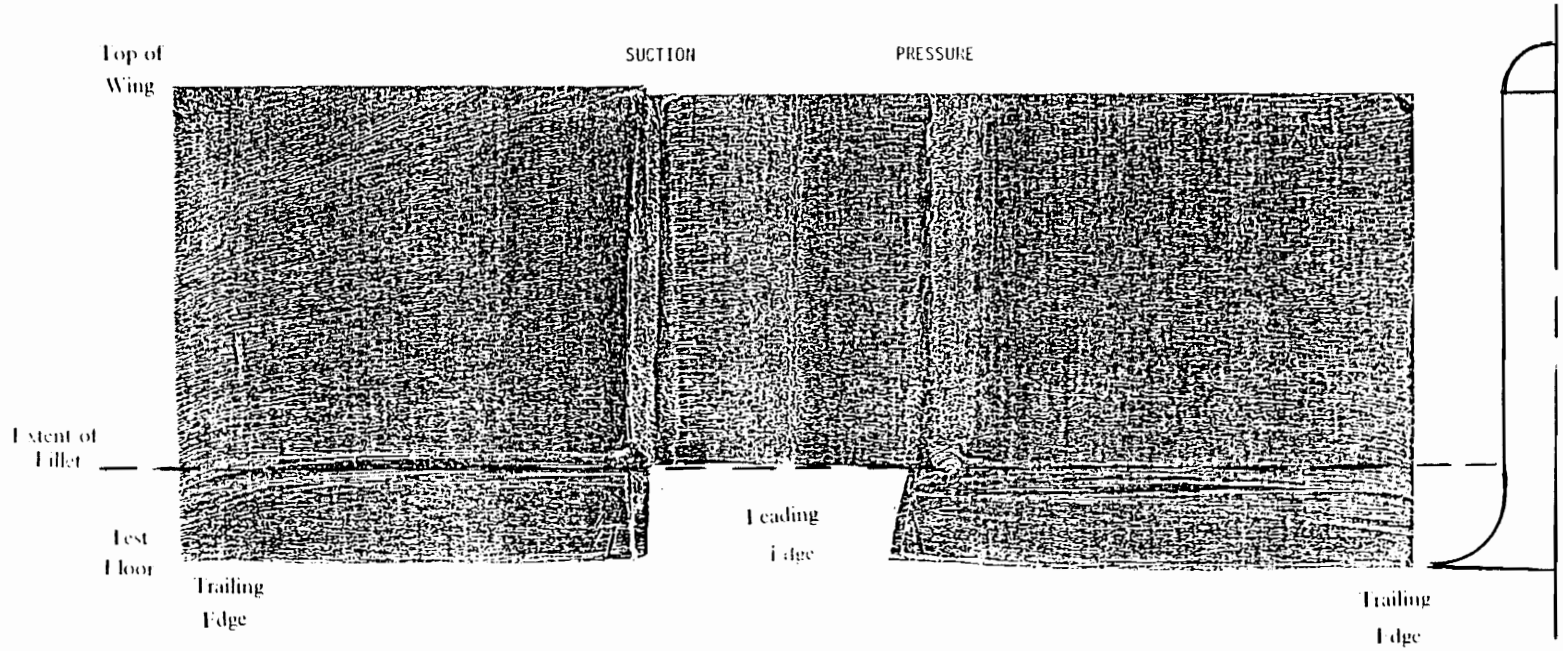

Figure 32. Oil-Flow Visualization on the Wing with Fillet at 6 Degrees Angle of Attack, Thin Boundary Layer, Stability Wind Tunnel.

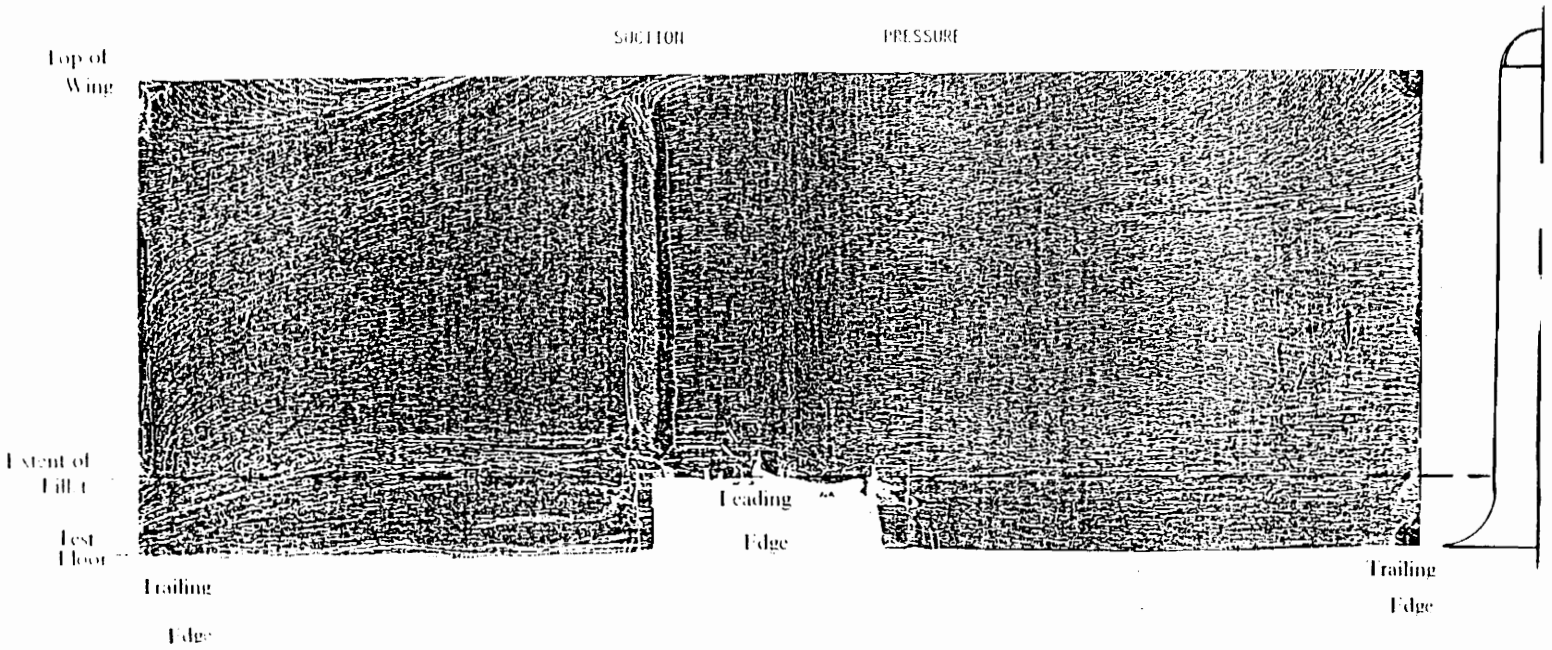

Figure 33. Oil-Flow Visualization on the Wing with Fillet at 12 Degrees Angle of Attack, Thin Boundary Layer, Stability Wind Tunnel.

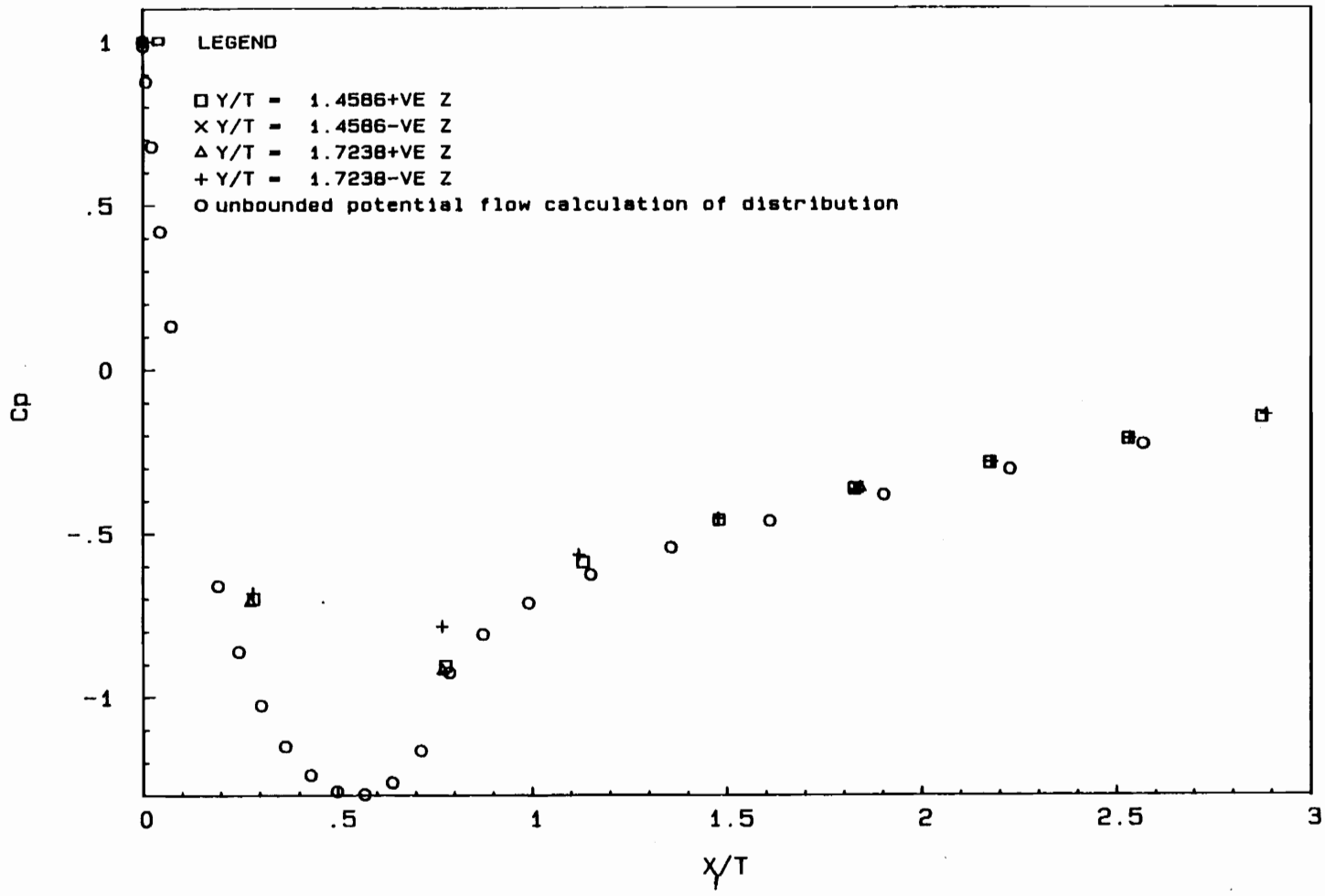

Figure 34. C_p Distribution on Baseline Wing at 0 Degrees Angle of Attack, Thin Boundary Layer, Boundary-Layer Tunnel.

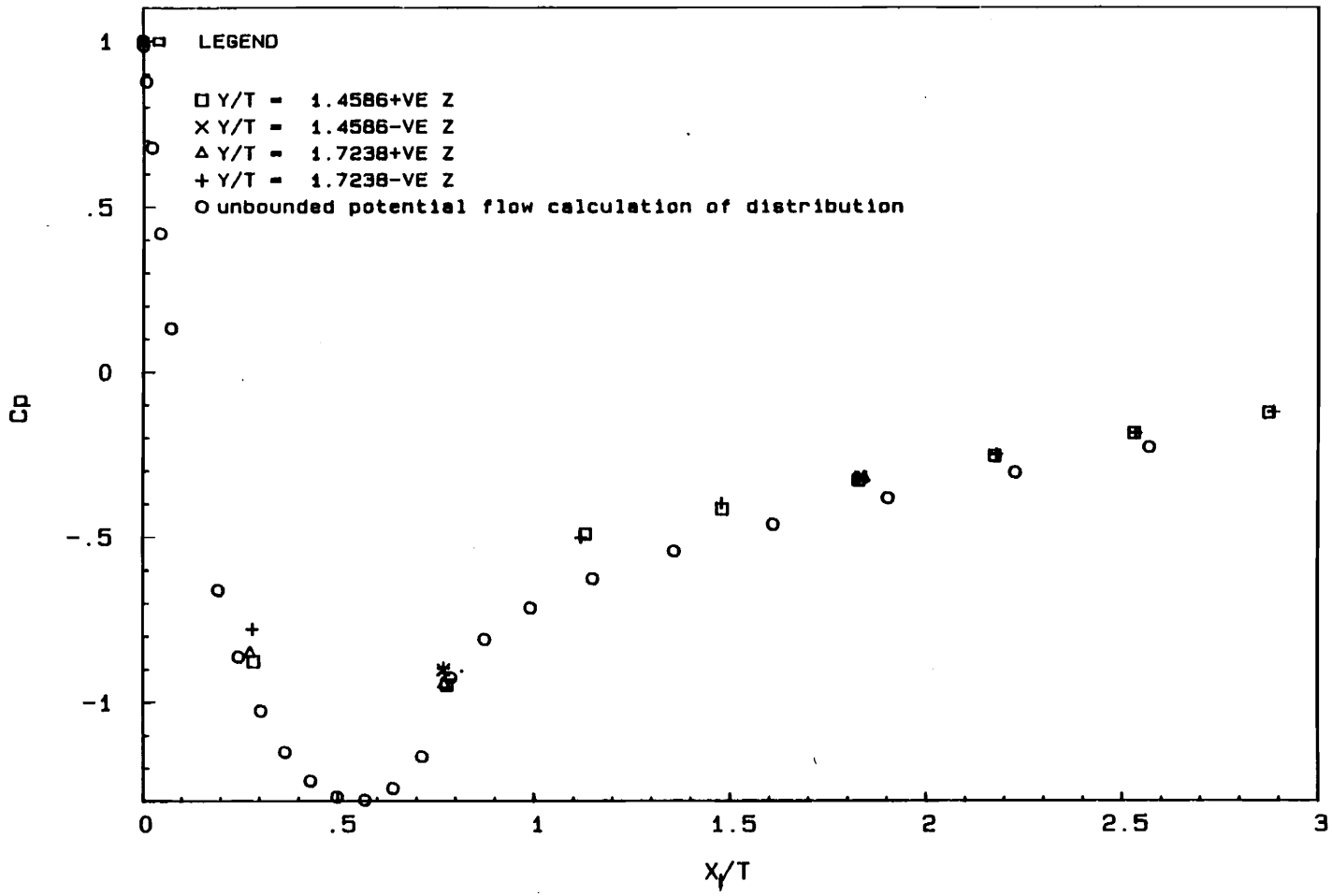

Figure 35. C_p Distribution on Baseline Wing at 0 Degrees Angle of Attack, Thin Boundary Layer, Stability Wind Tunnel.

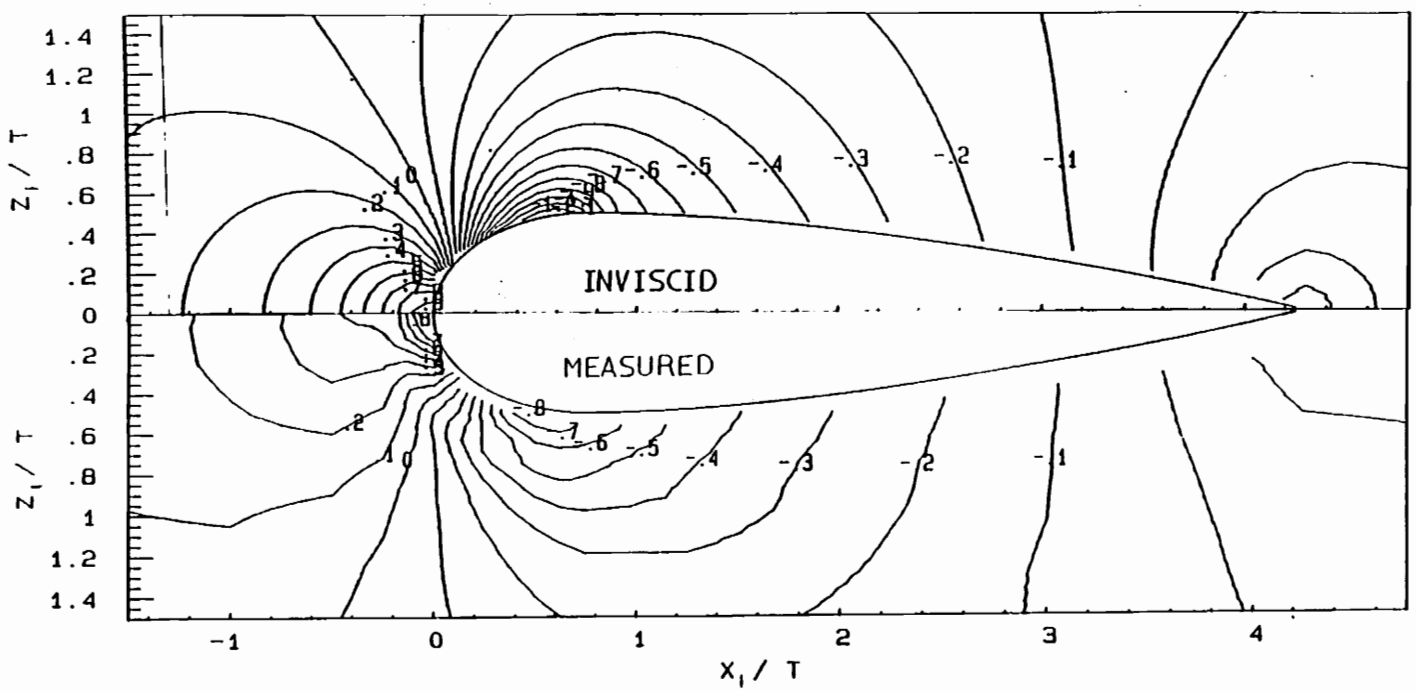

Figure 36. C_p Distribution on Floor Surrounding Baseline Wing and Unbounded Potential Flow Calculation of Distribution on Floor Surrounding Infinitely Long Baseline Wing at 0 Degrees Angle of Attack, Thin Boundary Layer, Boundary-Layer Tunnel.

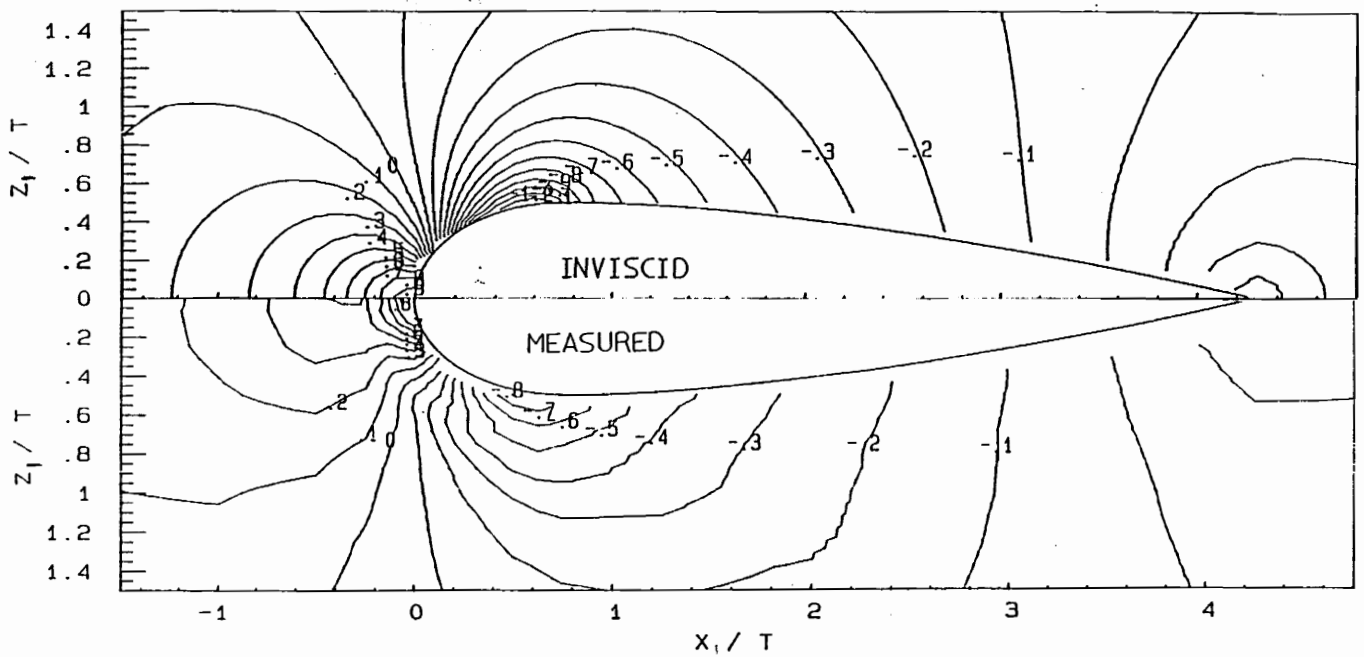

Figure 37. C_p Distribution on Floor Surrounding Baseline Wing and Unbounded Potential Flow Calculation of Distribution on Floor Surrounding Infinitely Long Baseline Wing at 0 Degrees Angle of Attack, Thin Boundary Layer, Stability Wind Tunnel.

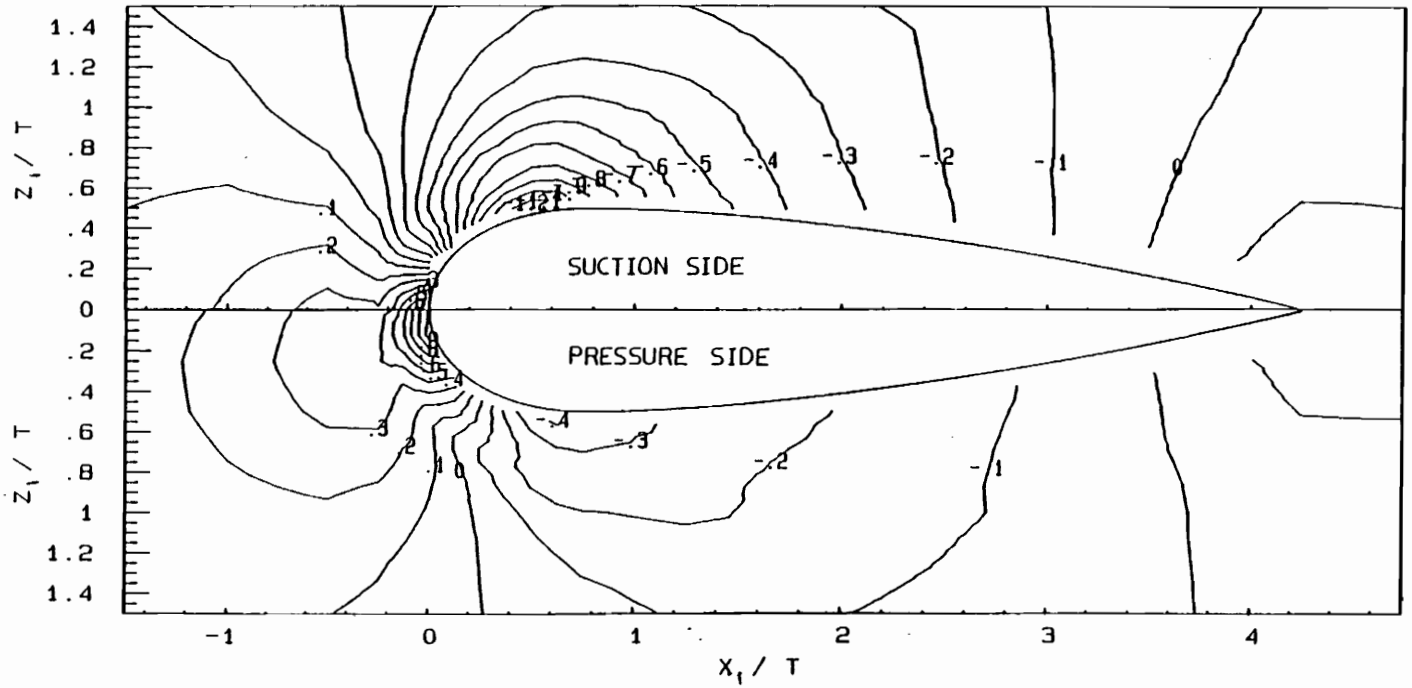

Figure 38. C_p Distribution on Floor Surrounding Baseline Wing at 6 Degrees Angle of Attack, Thin Boundary Layer, Stability Wind Tunnel.

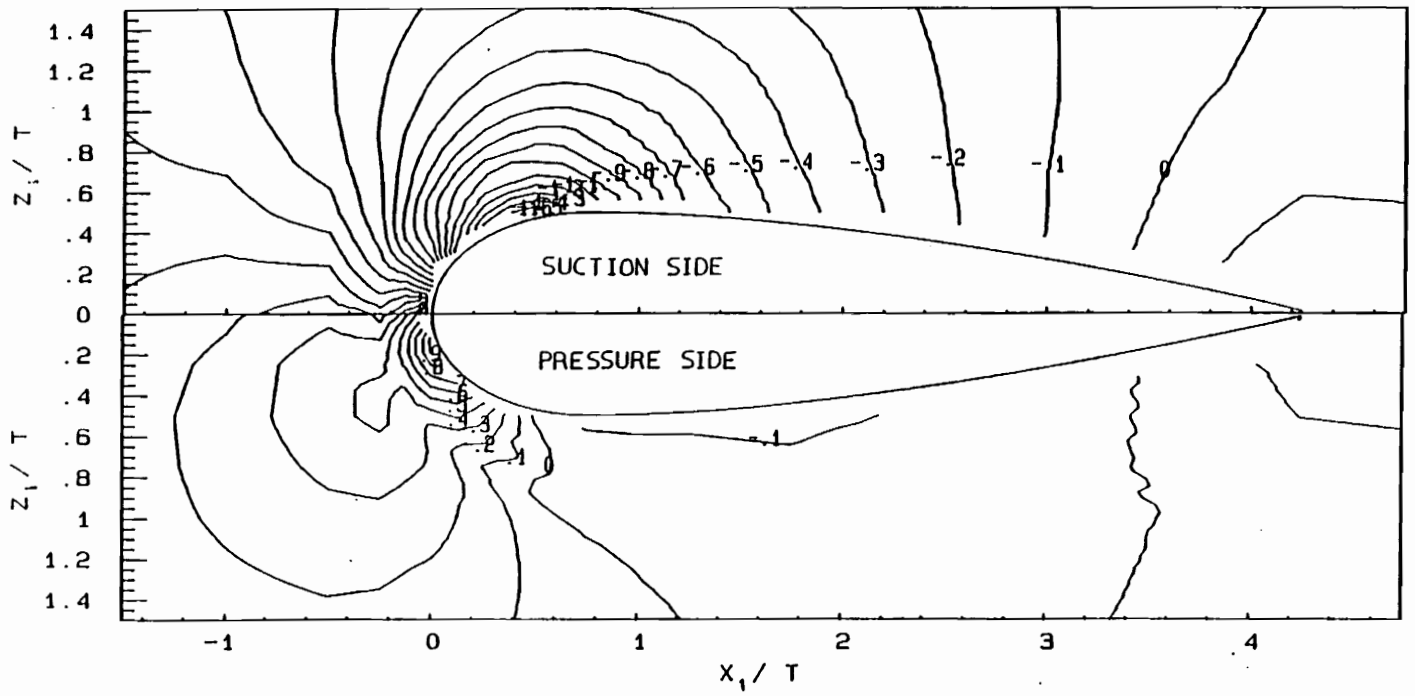

Figure 39. C_p Distribution on Floor Surrounding Baseline Wing at 12 Degrees Angle of Attack, Thin Boundary Layer, Stability Wind Tunnel.

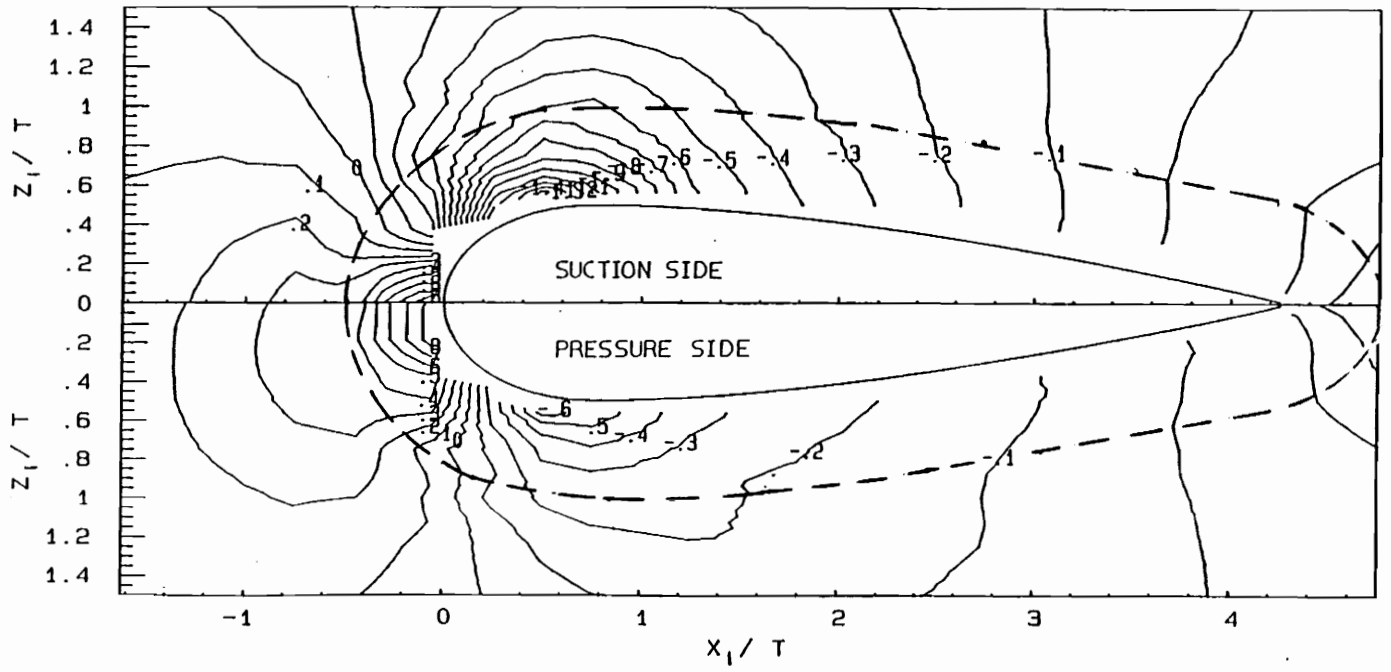

Figure 40. C_p Distribution on Floor Surrounding Wing with Fillet and Unbounded Potential Flow Calculation of Distribution on Floor Surrounding Infinitely Long Baseline Wing at 0 Degrees Angle of Attack, Thin Boundary Layer, Boundary-Layer Tunnel.

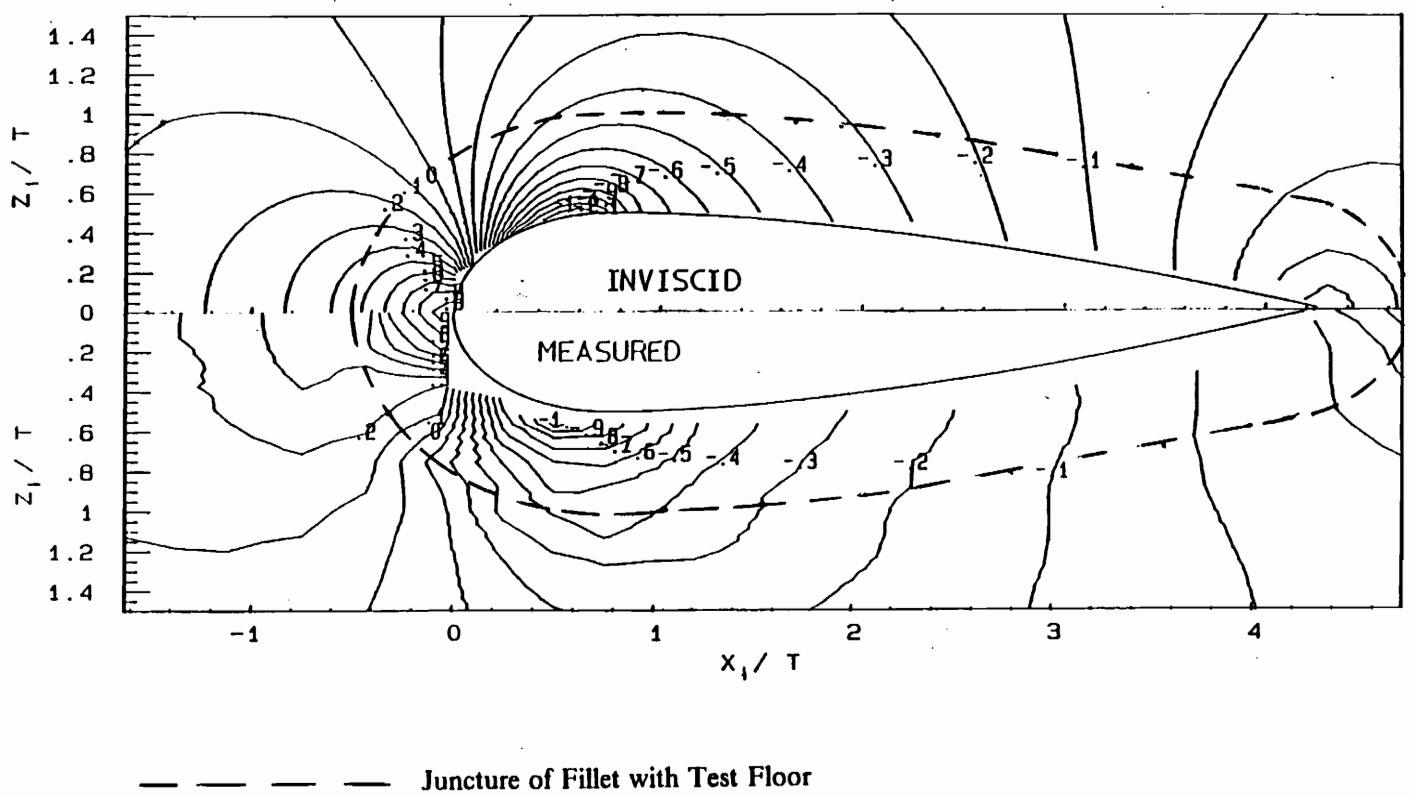

Figure 41. C_p Distribution on Floor Surrounding Wing with Fillet and Unbounded Potential Flow Calculation of Distribution on Floor Surrounding Infinitely Long Baseline Wing at 0 Degrees Angle of Attack, Thin Boundary Layer, Stability Wind Tunnel.

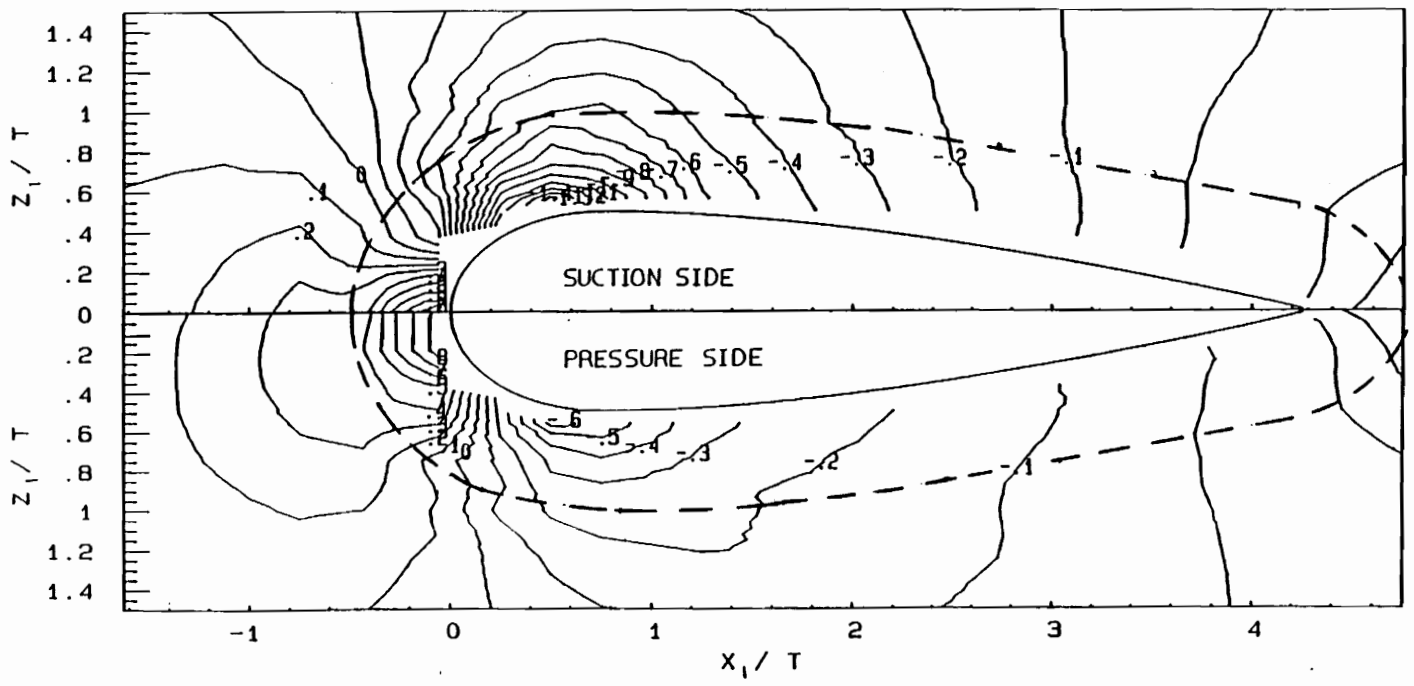

Figure 42. C_p Distribution on Floor Surrounding Wing with Fillet at 6 Degrees Angle of Attack, Thin Boundary Layer, Stability Wind Tunnel.

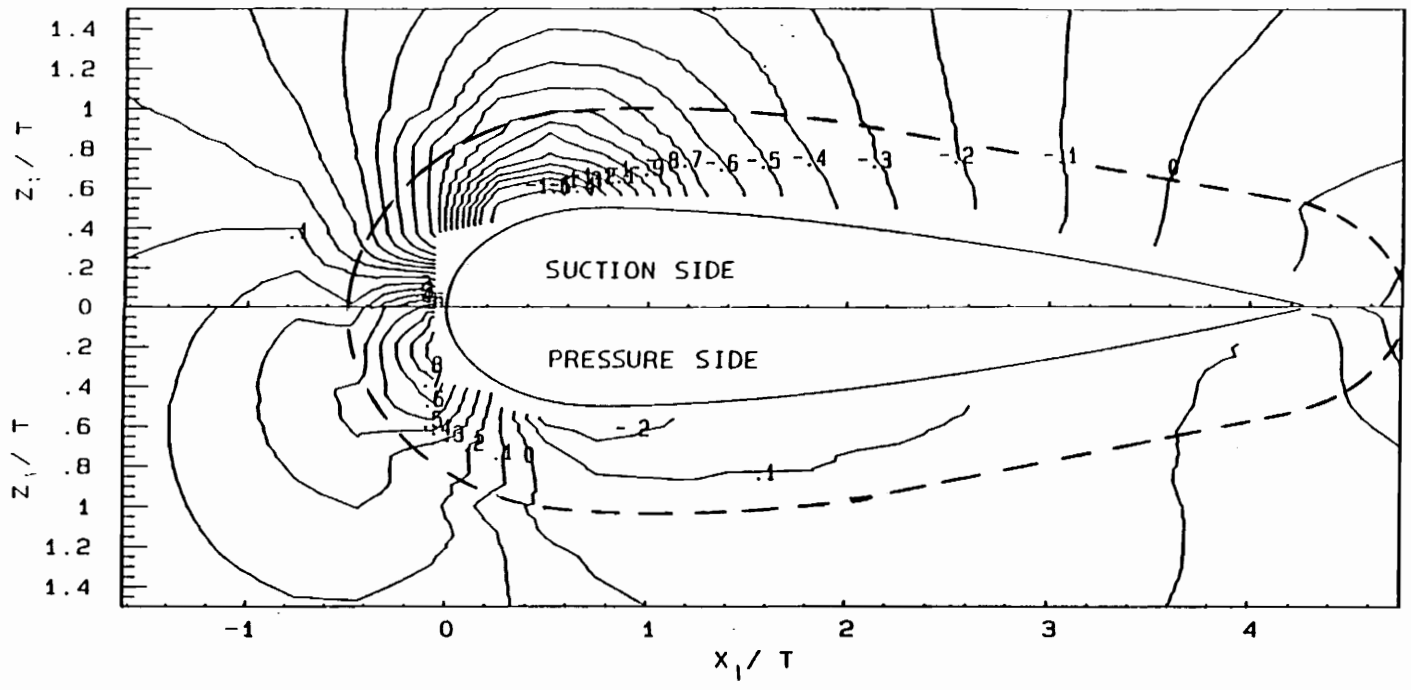

Figure 43. C_p Distribution on Floor Surrounding Wing with Fillet at 12 Degrees Angle of Attack, Thin Boundary Layer, Stability Wind Tunnel.

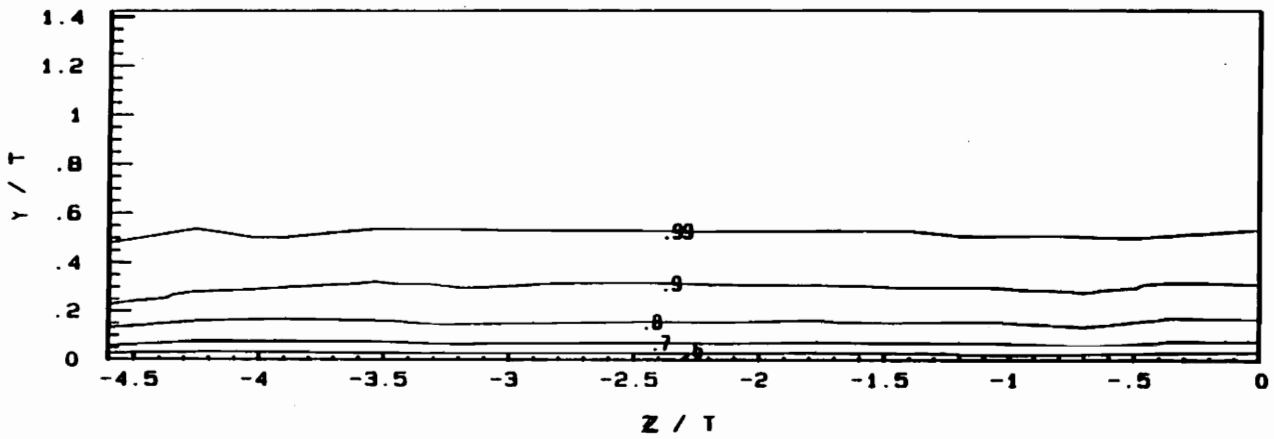

Figure 44. Contours of U/U_e at X/C=3, Empty Test Section, Thin Boundary Layer, Boundary-Layer Tunnel.

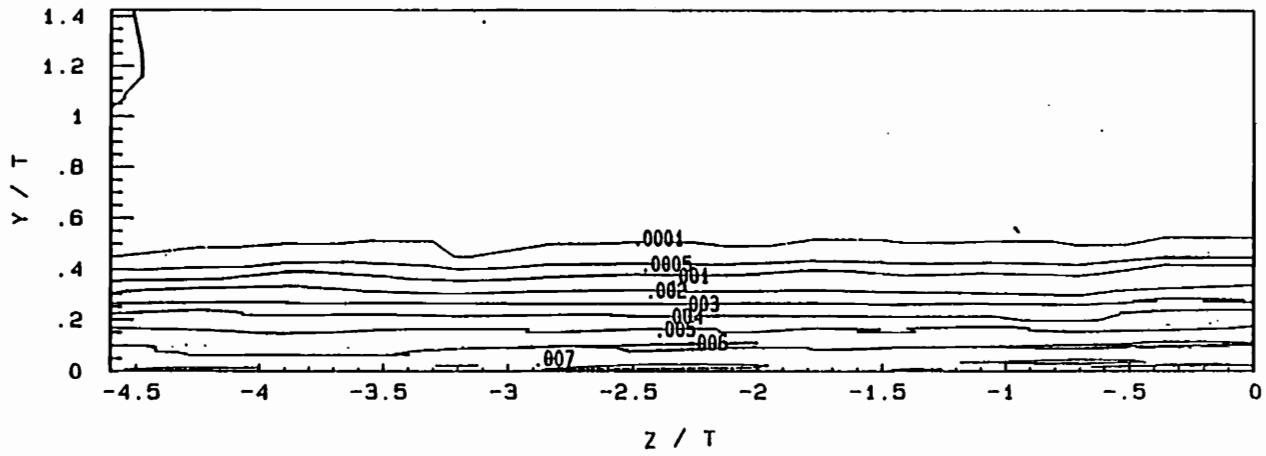

Figure 45. Contours of $\overline{u'^2}/U_e^2$ at X/C=3, Empty Test Section, Thin Boundary Layer, Boundary-Layer Tunnel.

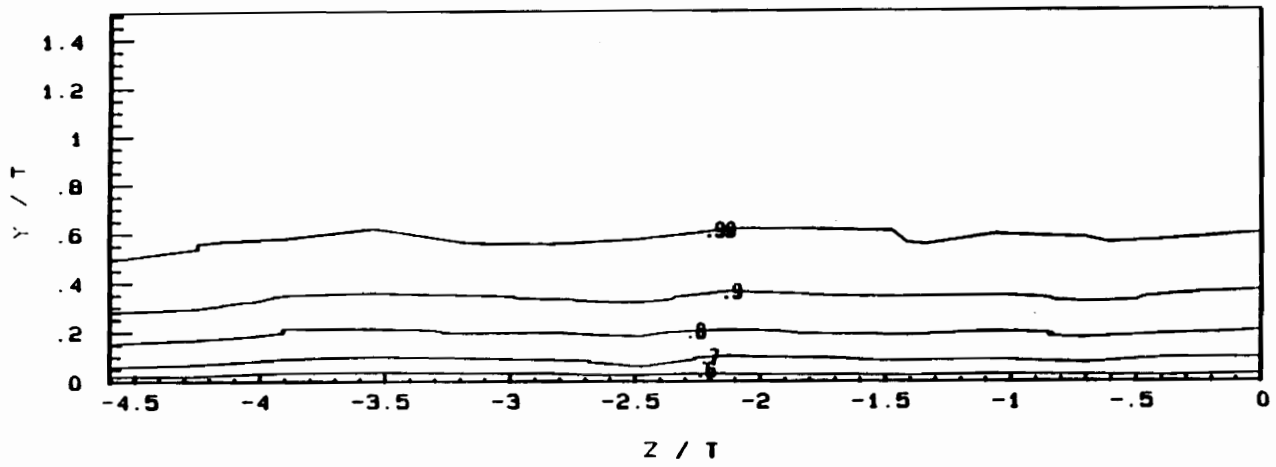

Figure 46. Contours of U/U_e at X/C=3, Empty Test Section, Thick Boundary Layer, Boundary-Layer Tunnel.

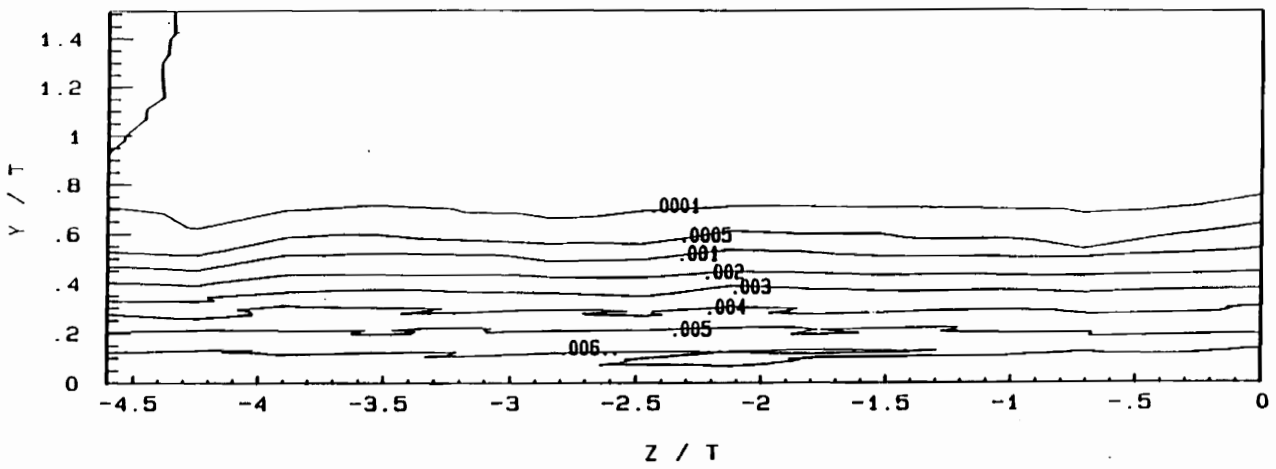

Figure 47. Contours of $\overline{u'^2}/U_e^2$ at X/C=3, Empty Test Section, Thick Boundary Layer, Boundary-Layer Tunnel.

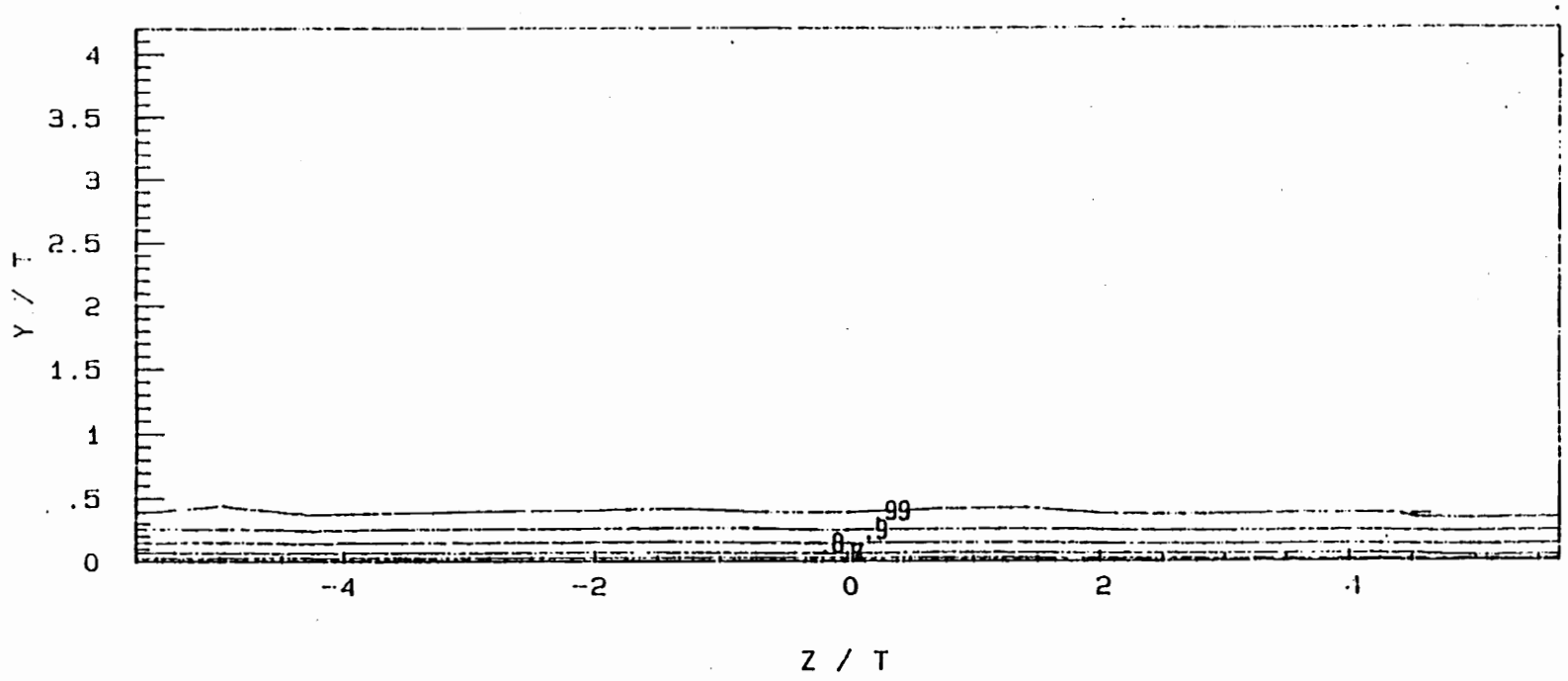

Figure 48. Contours of U/U_e at X/C=3, Empty Test Section, Thin Boundary Layer, Stability Wind Tunnel.

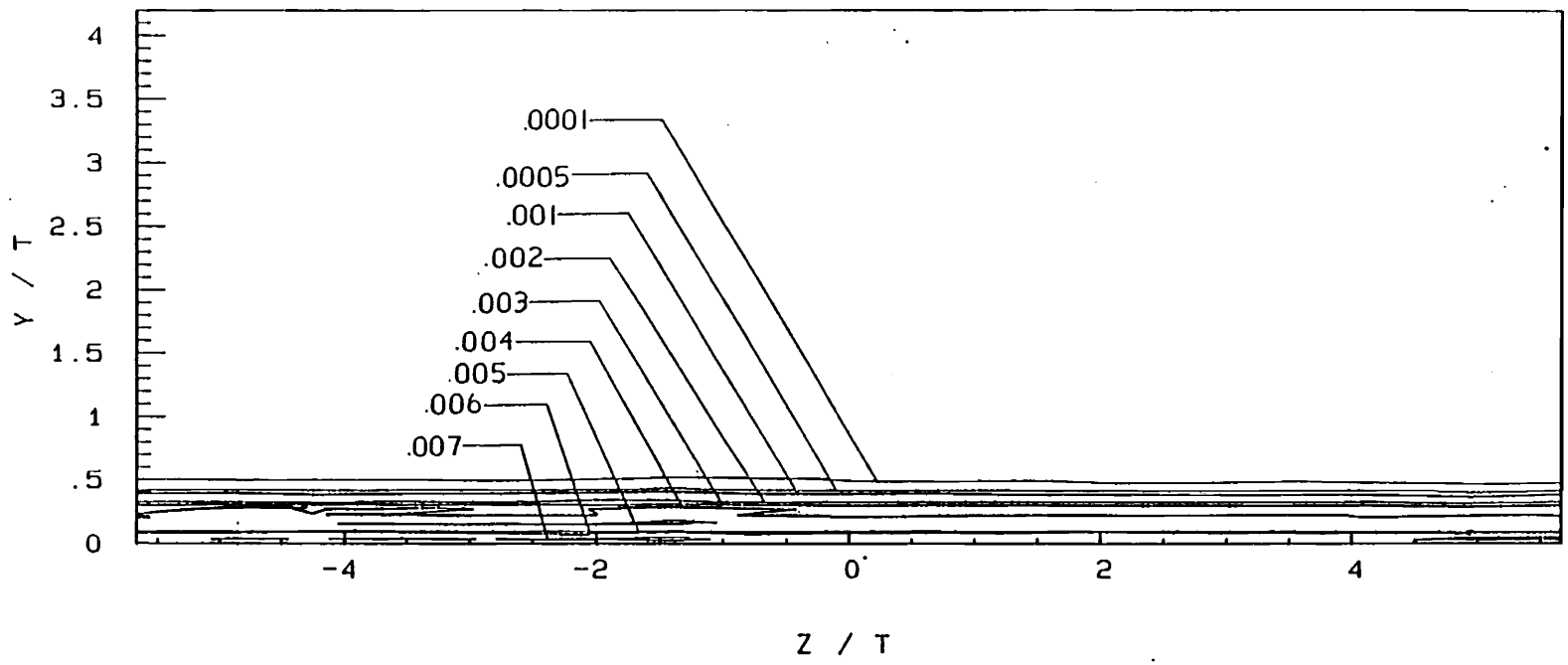

Figure 49. Contours of $\overline{u'^2}/U_e^2$ at X/C=3, Empty Test Section, Thin Boundary Layer, Stability Wind Tunnel.

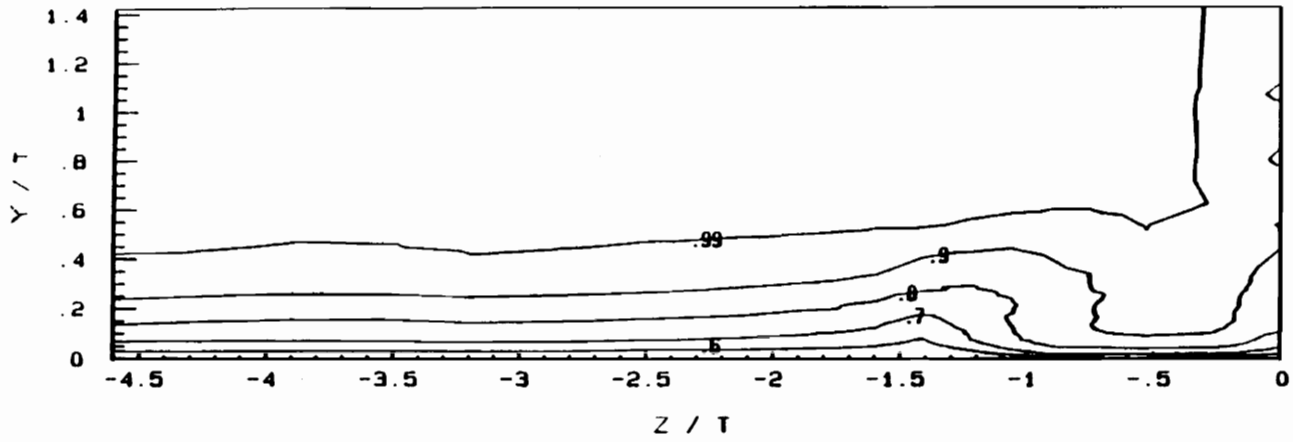

Figure 50. Contours of U/U_e at X/C = 3, Baseline Wing at 0 Degrees Angle of Attack, Thin Boundary Layer, Boundary-Layer Tunnel.

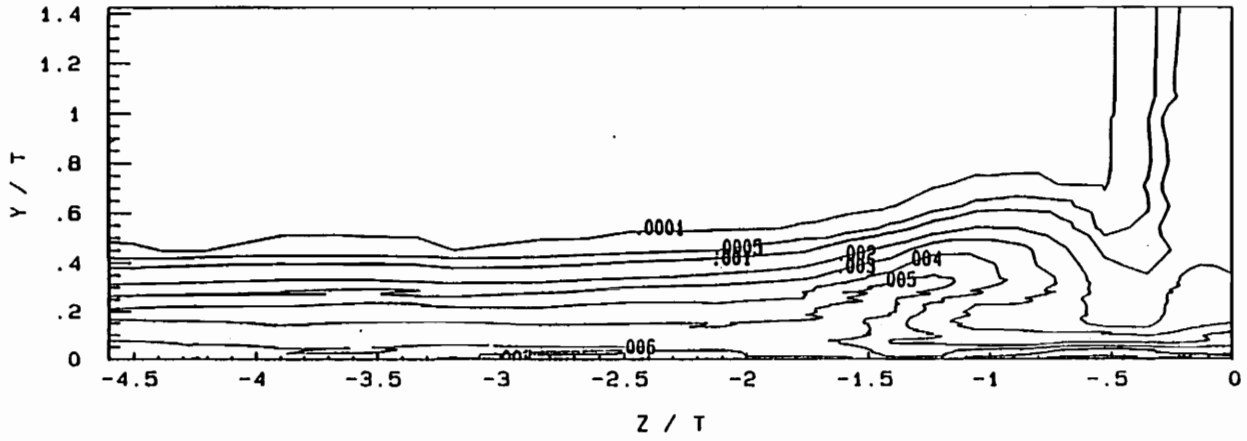

Figure 51. Contours of $\overline{u'^2}/U_e^2$ at X/C=3, Baseline Wing at 0 Degrees Angle of Attack, Thin Boundary Layer, Boundary-Layer Tunnel.

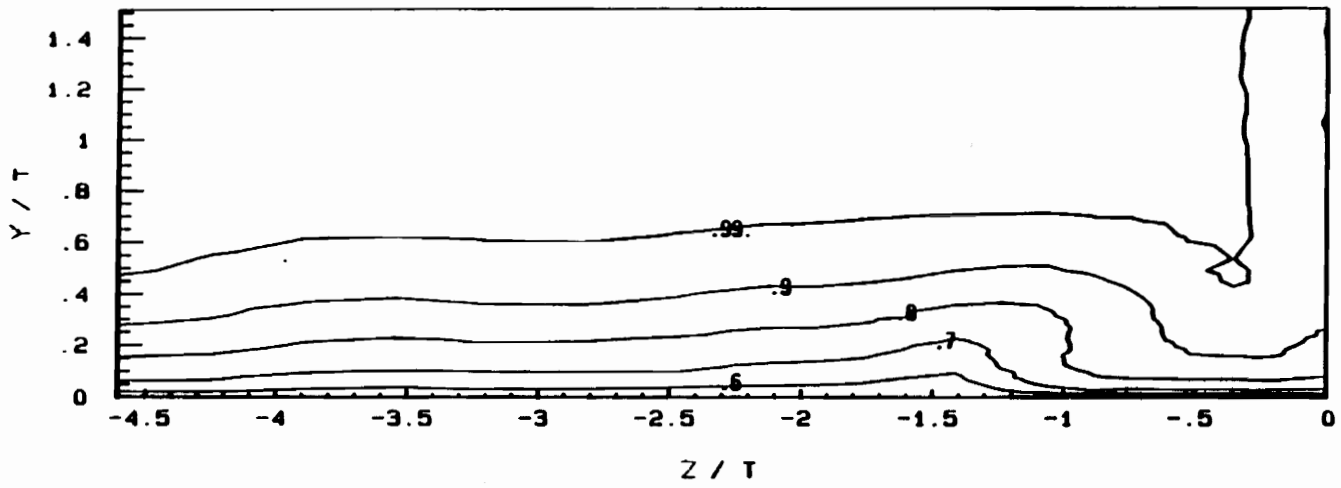

Figure 52. Contours of U/U_e at X/C = 3, Baseline Wing at 0 Degrees Angle of Attack, Thick Boundary Layer, Boundary-Layer Tunnel.

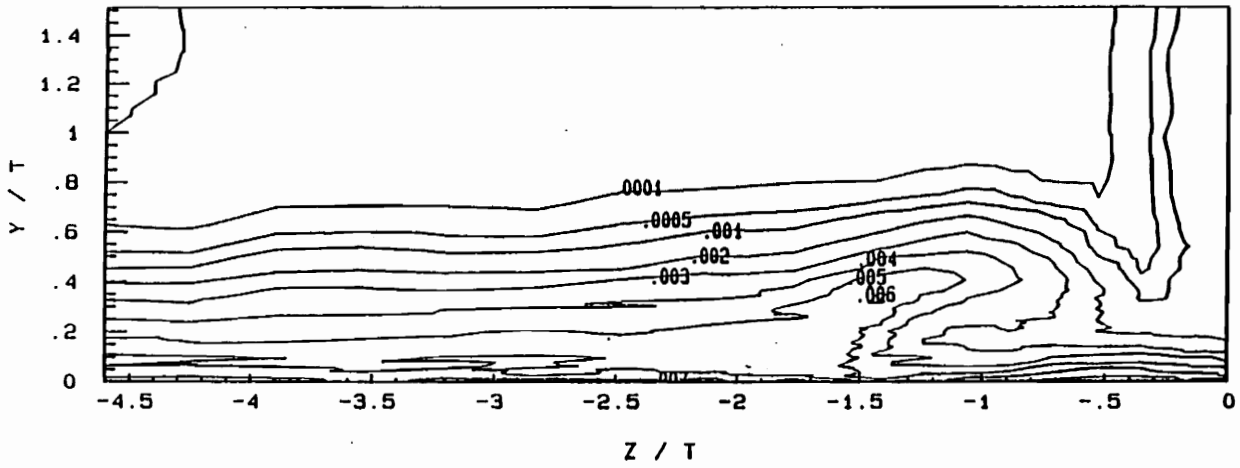

Figure 53. Contours of $\overline{u'^2}/U_e^2$ at X/C=3, Baseline Wing at 0 Degrees Angle of Attack, Thick Boundary Layer, Boundary-Layer Tunnel.

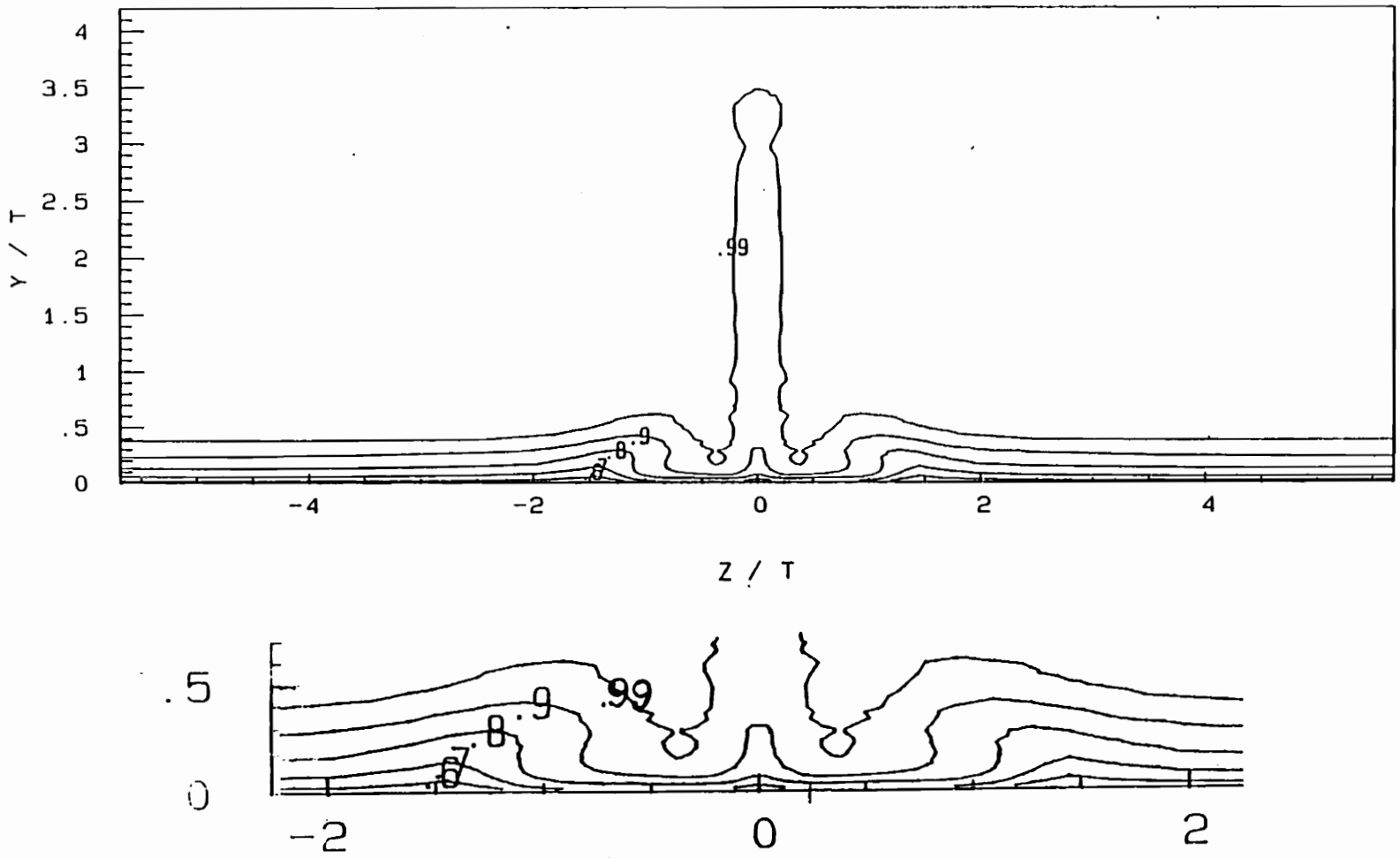

Figure 54. Contours of U/U_e at X/C = 3, Baseline Wing at 0 Degrees Angle of Attack, Thin Boundary Layer, Stability Wind Tunnel.

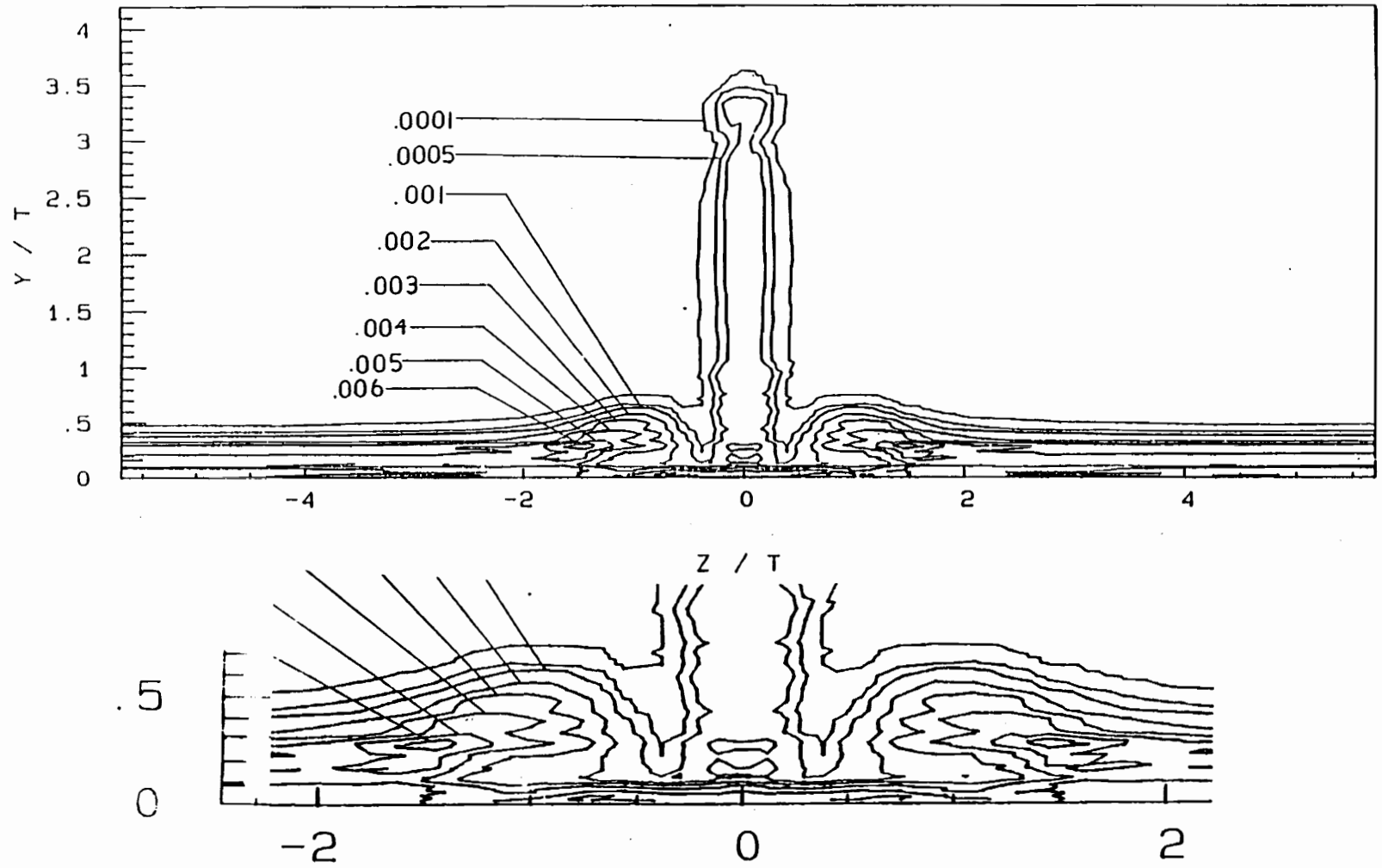

Figure 55. Contours of $\overline{u'^2}/U_e^2$ at X/C=3, Baseline Wing at 0 Degrees Angle of Attack, Thin Boundary Layer, Stability Wind Tunnel.

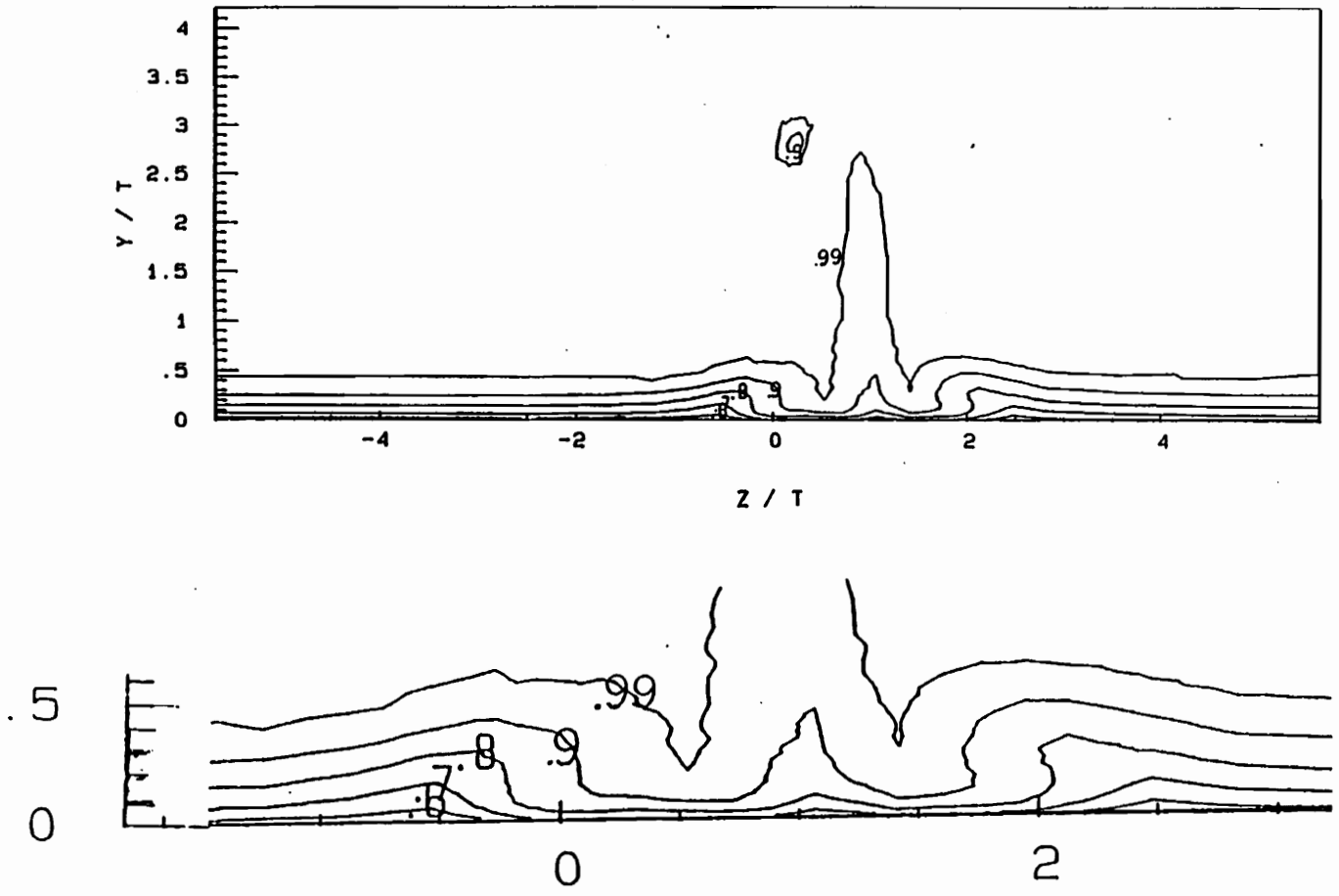

Figure 56. Contours of U/U_e at X/C = 3, Baseline Wing at 6 Degrees Angle of Attack, Thin Boundary Layer, Stability Wind Tunnel.

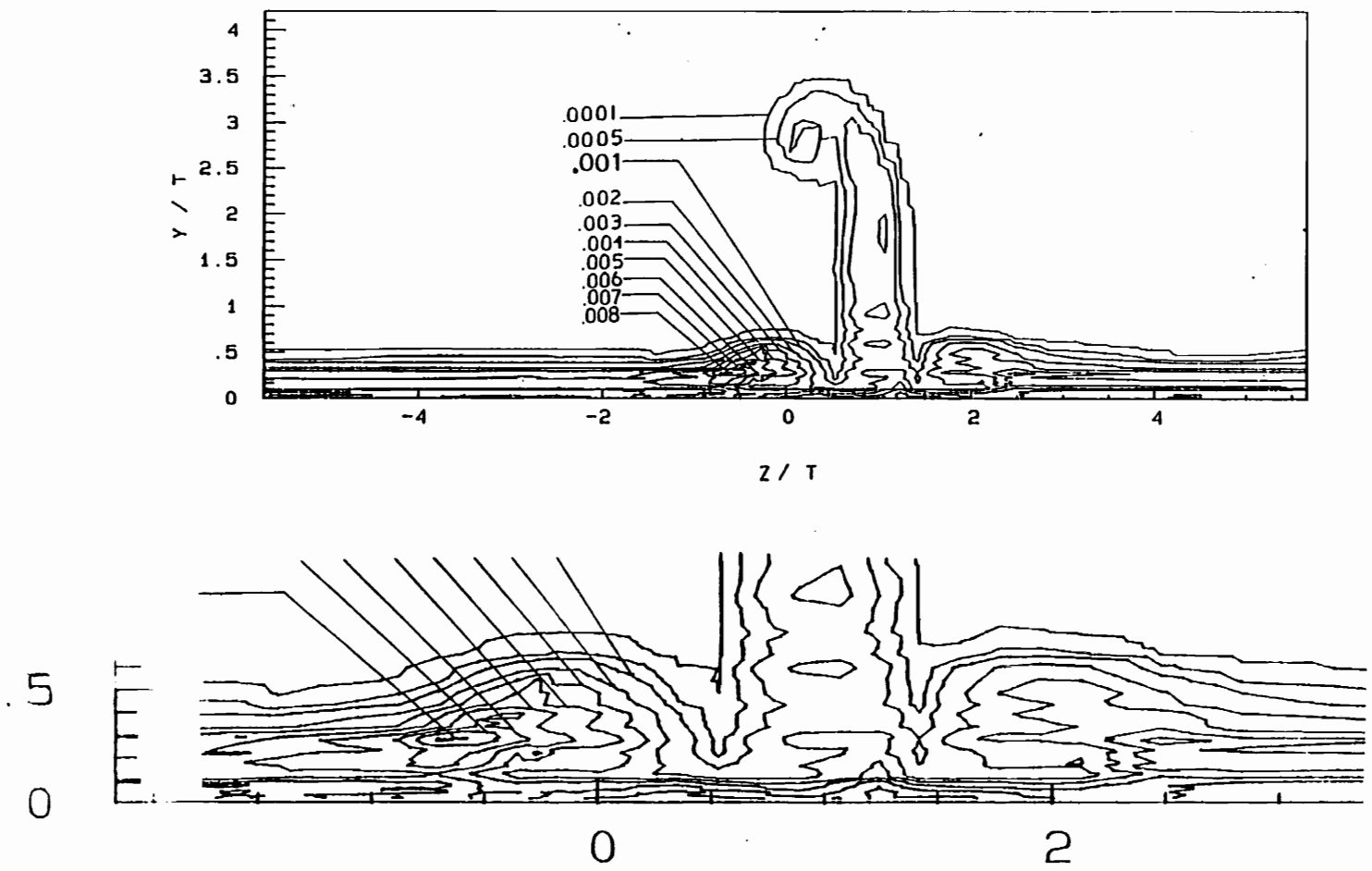

Figure 57. Contours of $\overline{u'^2}/U_e^2$ at X/C=3, Baseline Wing at 6 Degrees Angle of Attack, Thin Boundary Layer, Stability Wind Tunnel.

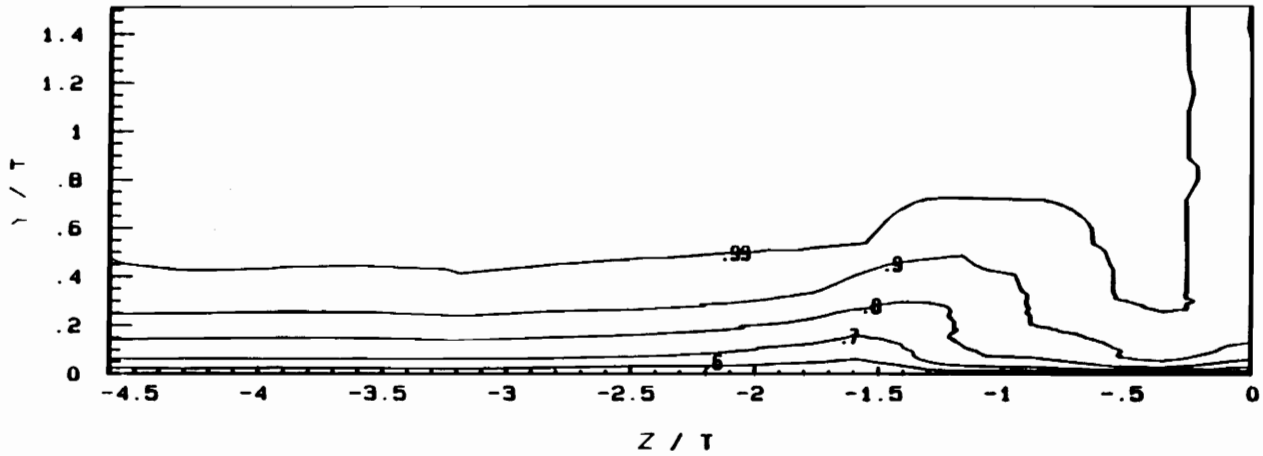

Figure 58. Contours of U/U_e at X/C=3, Wing with Fillet at 0 Degrees Angle of Attack, Thin Boundary Layer, Boundary-Layer Tunnel.

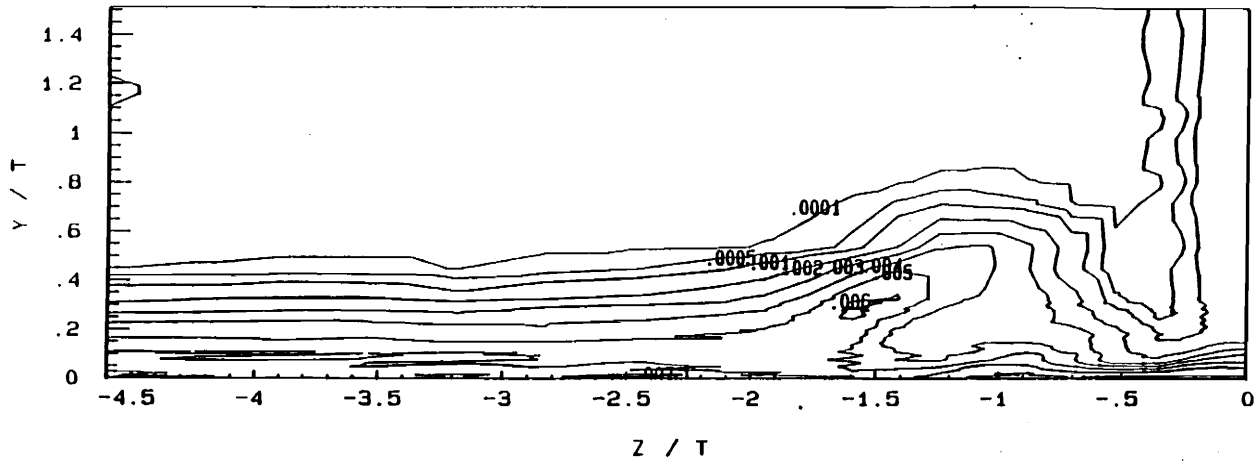

Figure 59. Contours of $\overline{u'^2}/U_e^2$ at X/C = 3, Wing with Fillet at 0 Degrees Angle of Attack, Thin Boundary Layer, Boundary-Layer Tunnel.

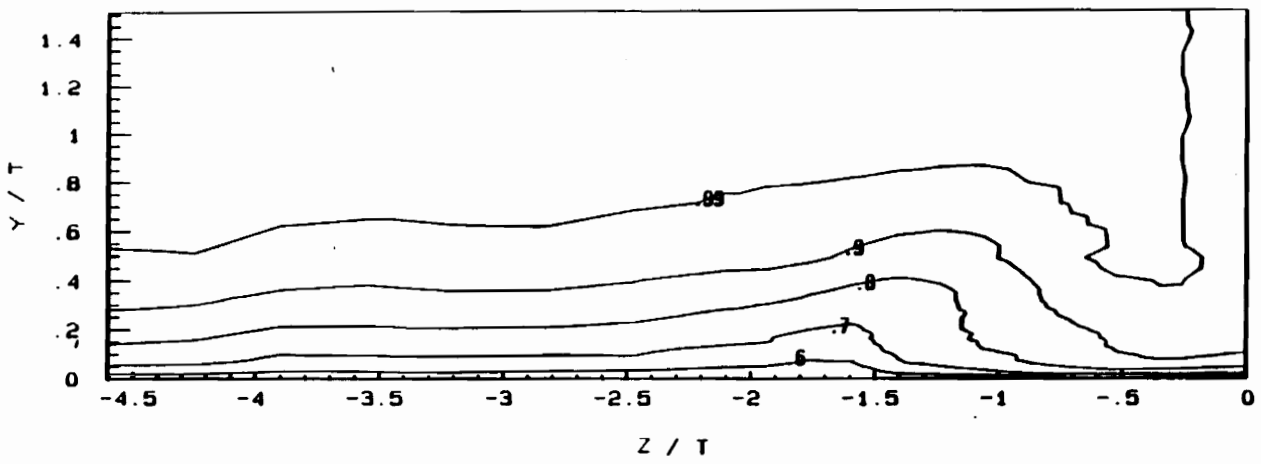

Figure 60. Contours of U/U_e at X/C=3, Wing with Fillet at 0 Degrees Angle of Attack, Thick Boundary Layer, Boundary-Layer Tunnel.

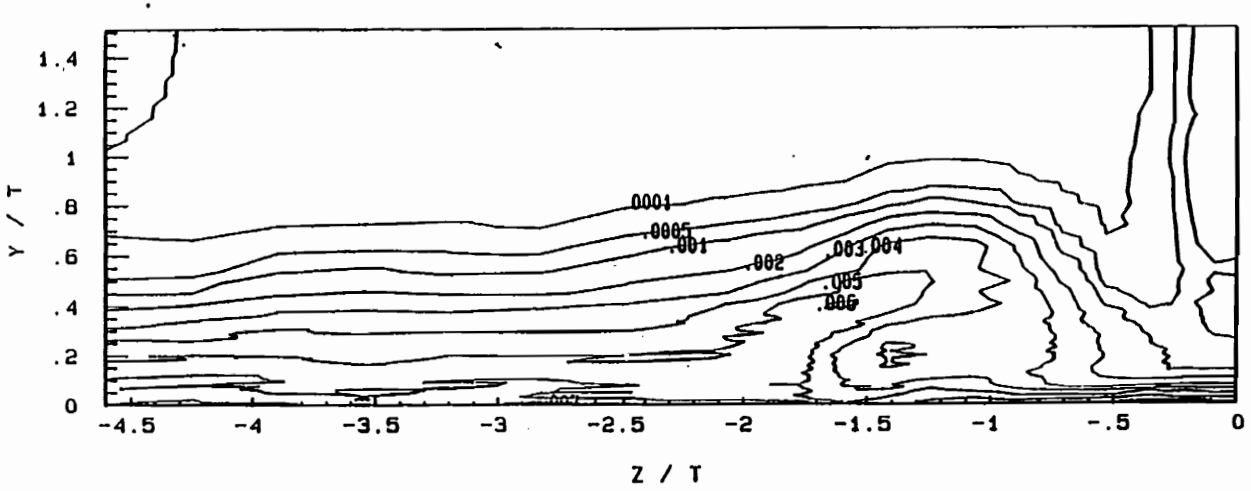

Figure 61. Contours of $\overline{u'^2}/U_e^2$ at X/C=3, Wing with Fillet at 0 Degrees Angle of Attack, Thick Boundary Layer, Boundary-Layer Tunnel.

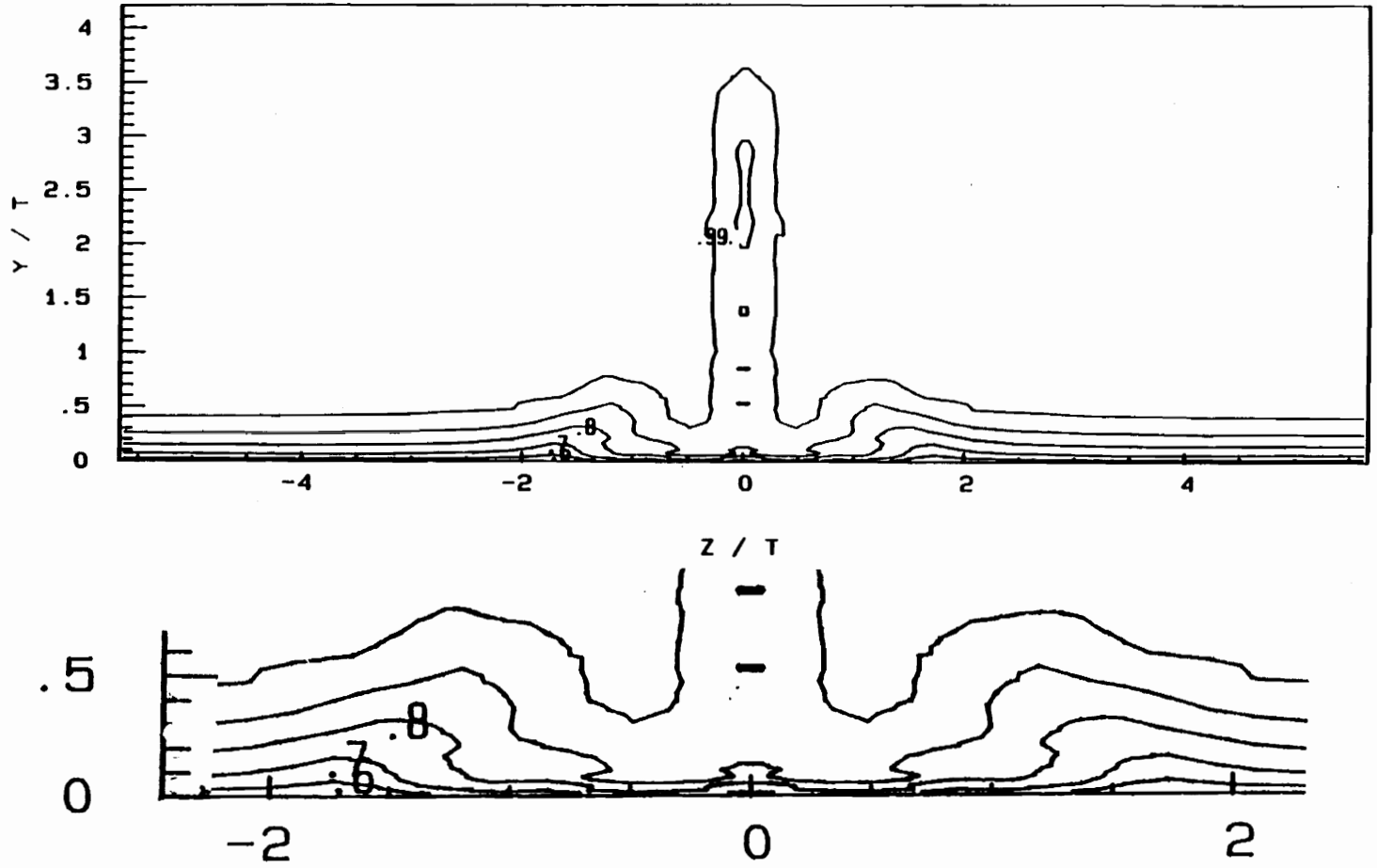

Figure 62. Contours of U/U_e at X/C=3, Wing with Fillet at 0 Degrees Angle of Attack, Thin Boundary Layer, Stability Wind Tunnel.

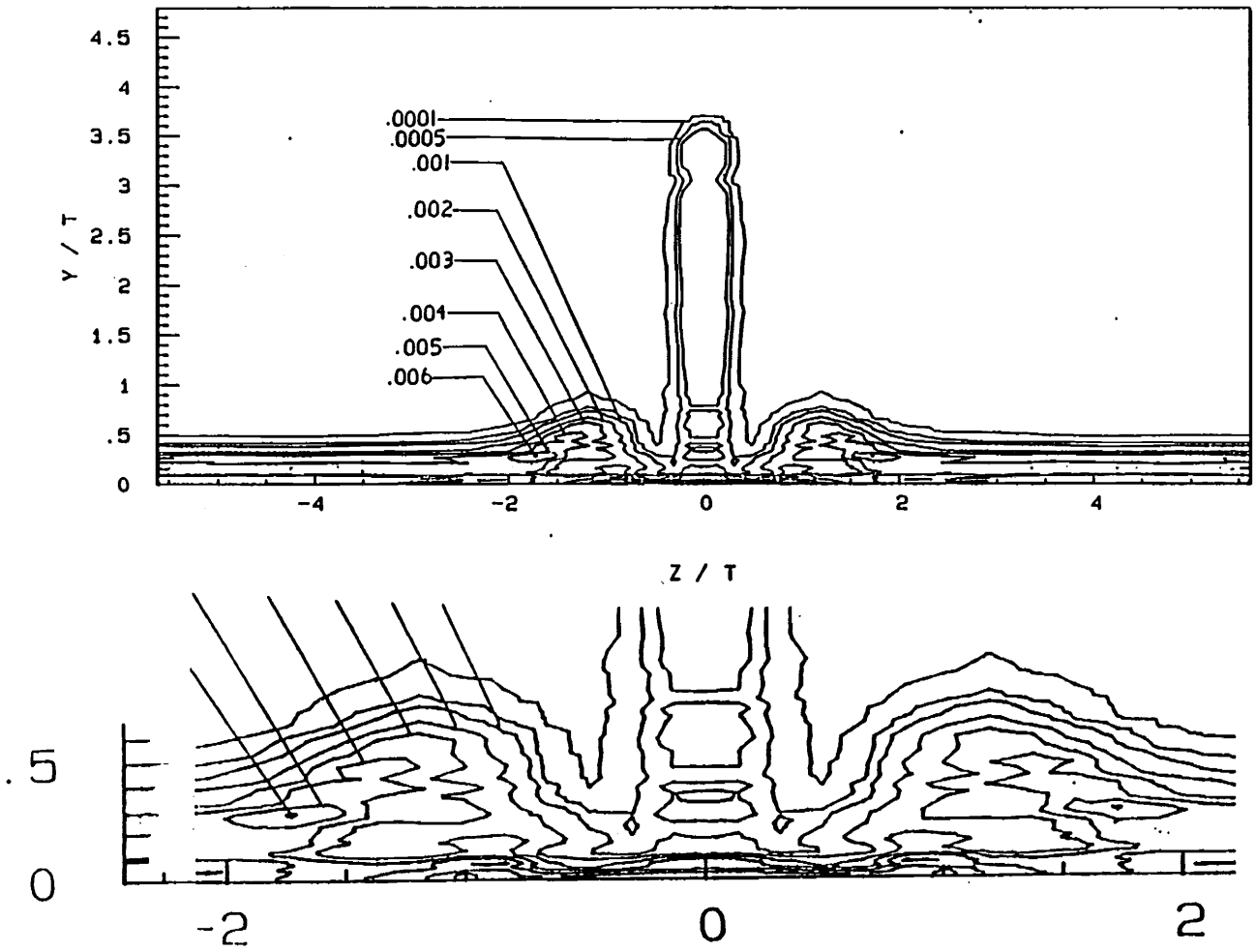

Figure 63. Contours of $\overline{u'^2}/U_e^2$ at X/C=3, Wing with Fillet at 0 Degrees Angle of Attack, Thin Boundary Layer, Stability Wind Tunnel.

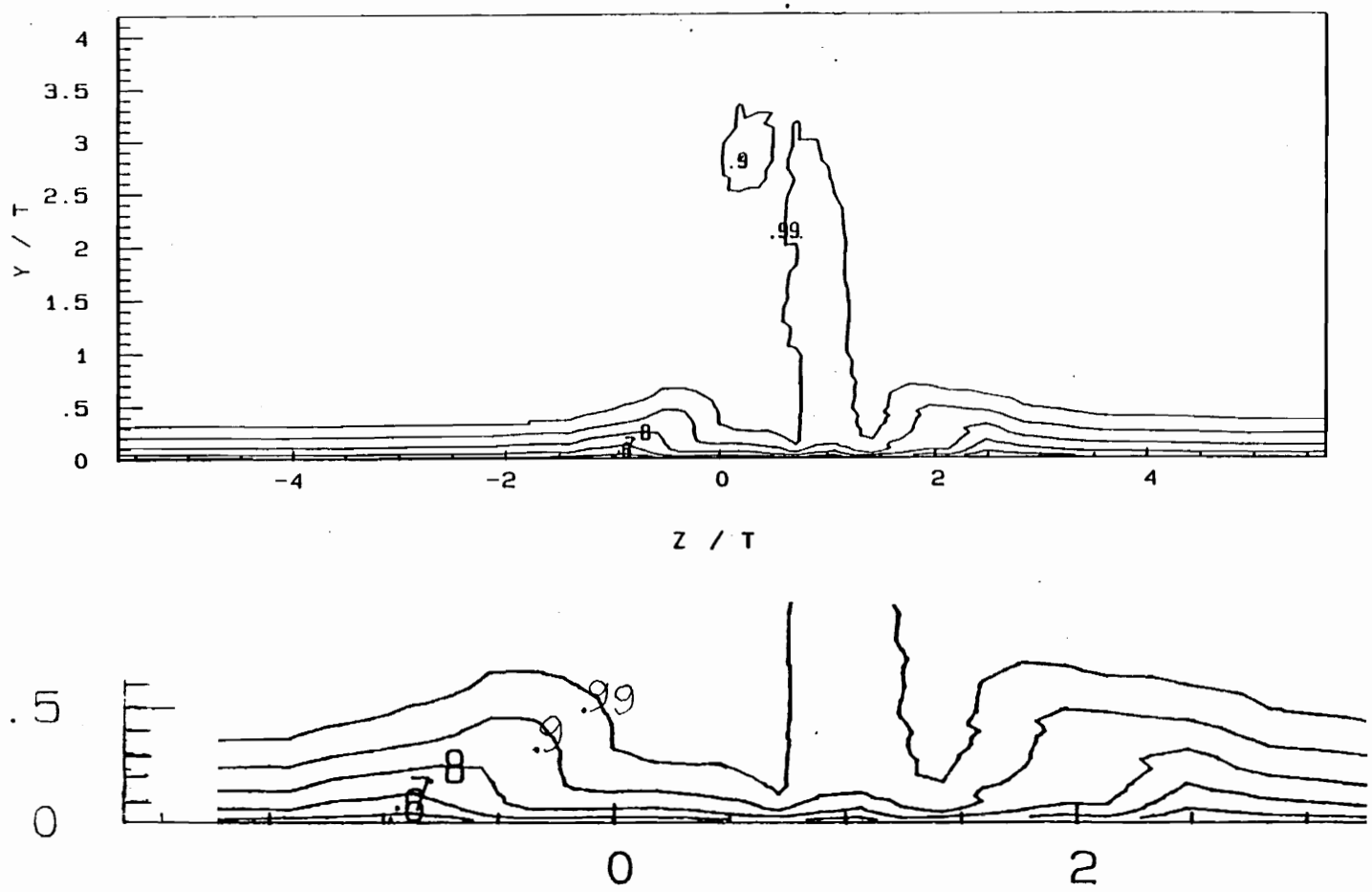

Figure 64. Contours of U/U_e at X/C=3, Wing with Fillet at 6 Degrees Angle of Attack, Thin Boundary Layer, Stability Wind Tunnel.

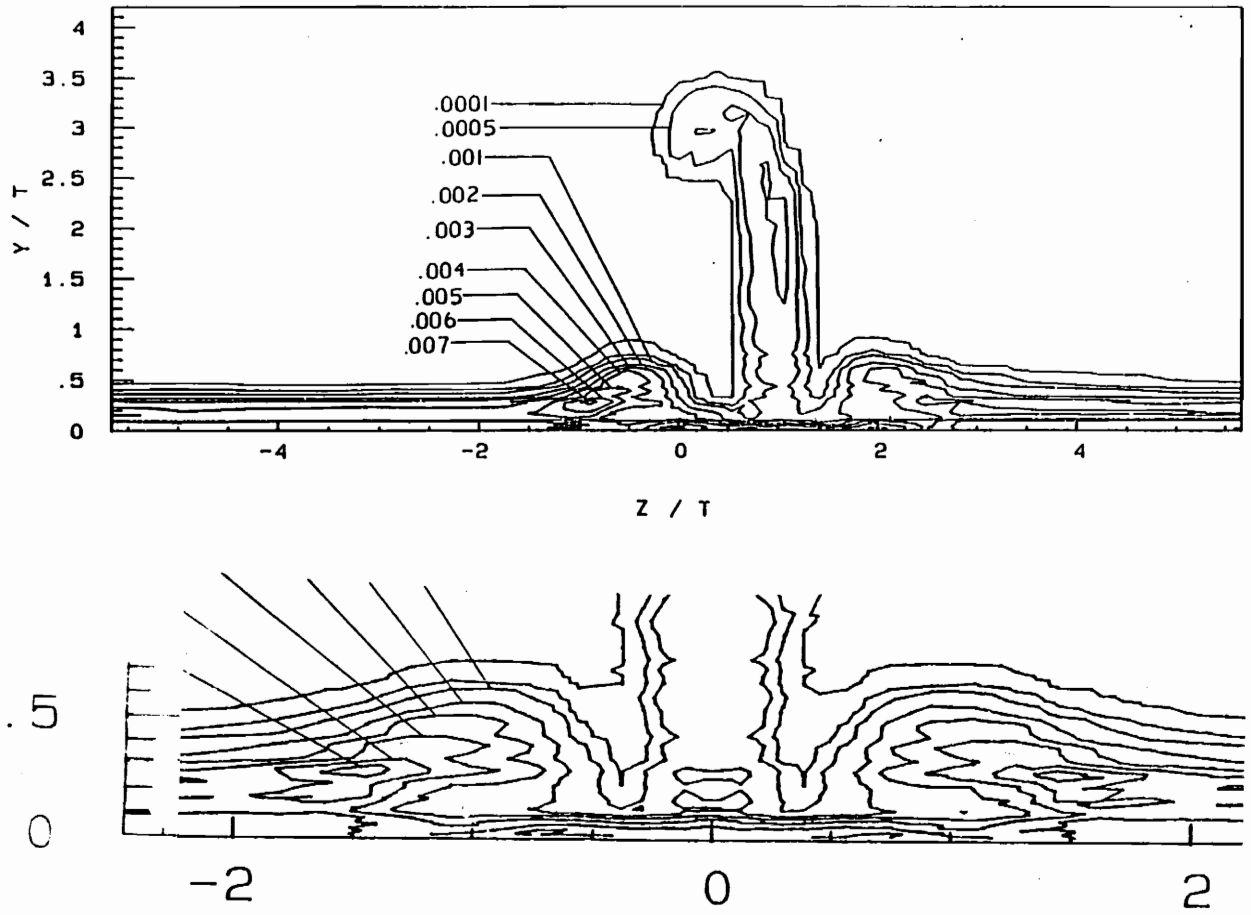

Figure 65. Contours of $\overline{u'^2}/U_e^2$ at X/C=3, Wing with Fillet at 6 Degrees Angle of Attack, Thin Boundary Layer, Stability Wind Tunnel.

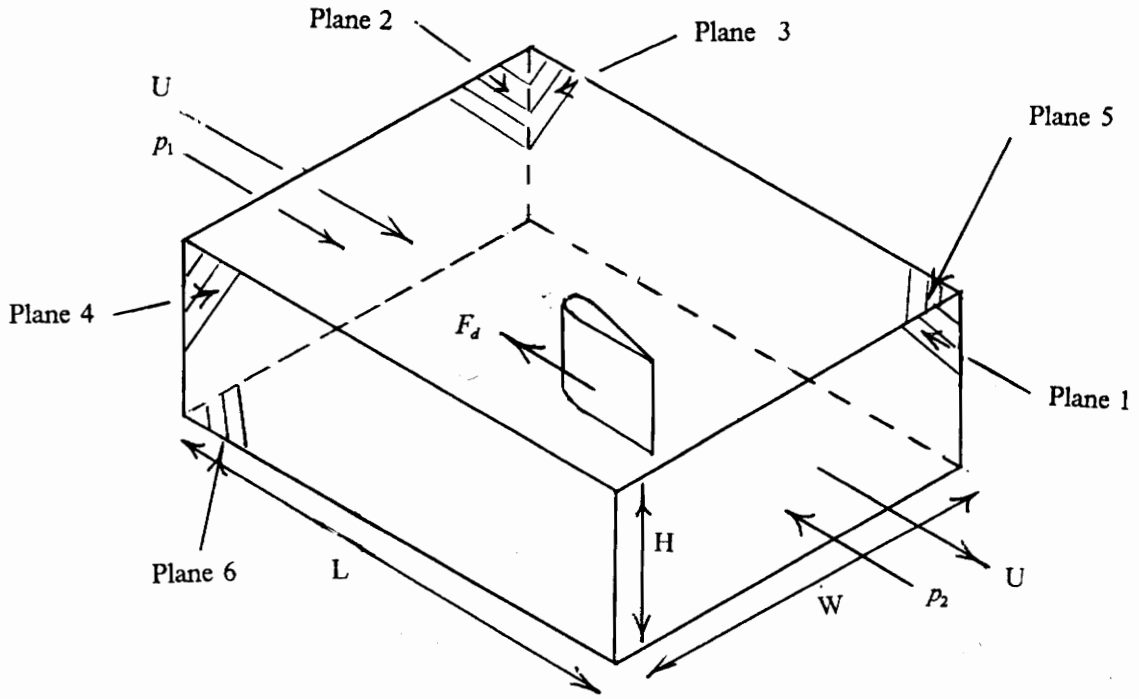

Figure 66. Control Volume Used in Drag and Entrainment Calculations.

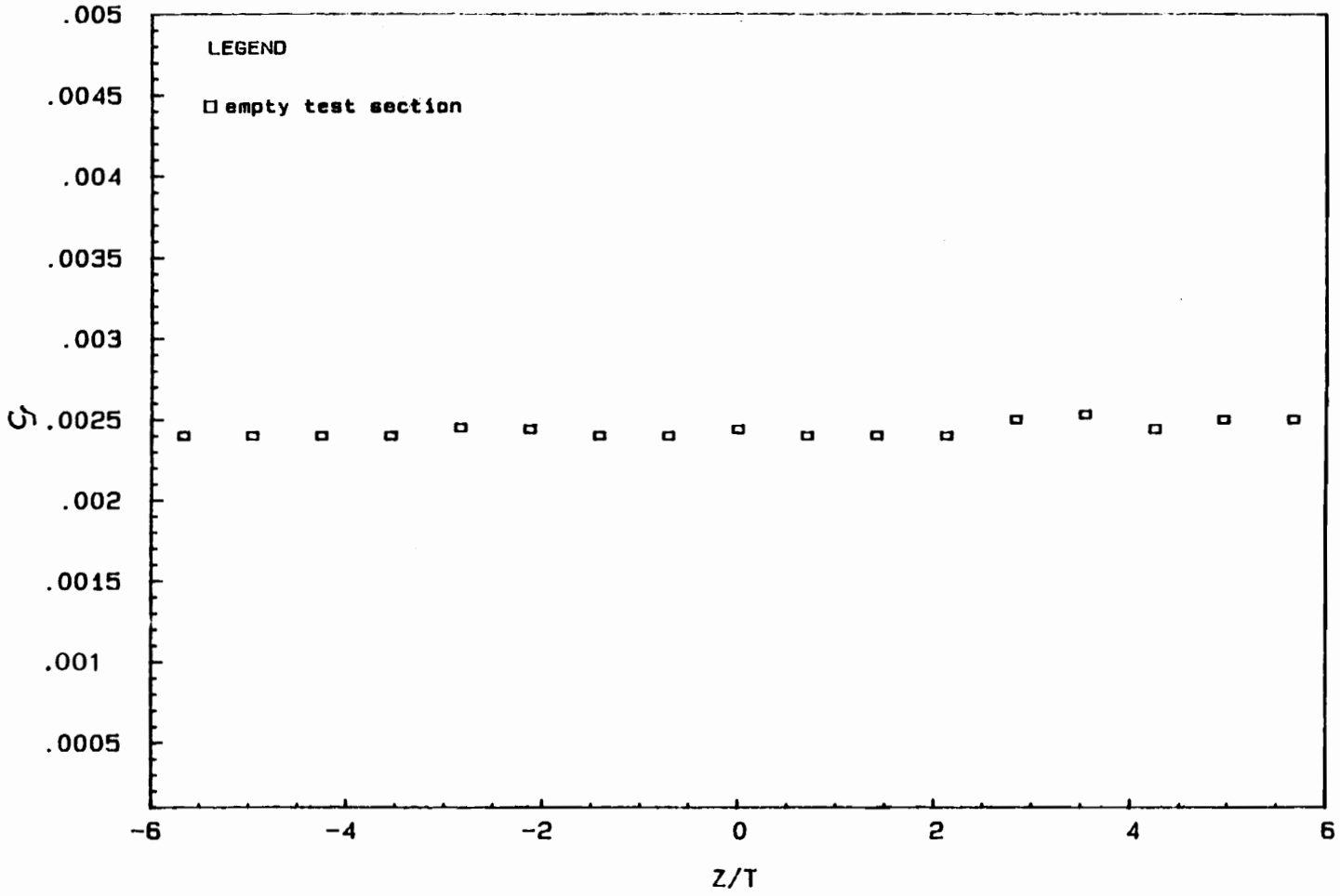

Figure 67. Spanwise C_f Distribution at X/C=3, Empty Test Section, Thin Boundary Layer, Stability Wind Tunnel.

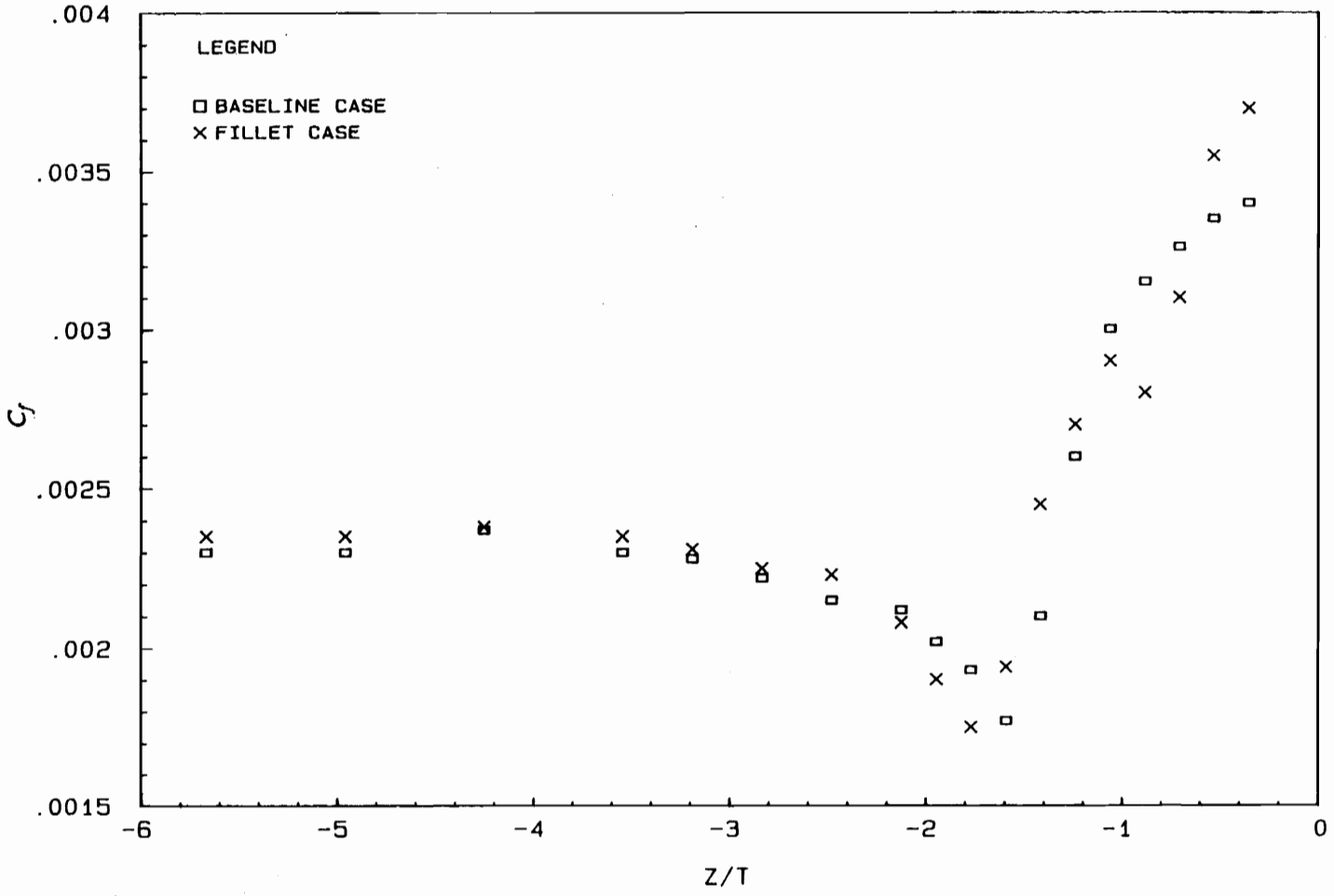

Figure 68. Spanwise C_f Distribution at X/C = 3, Wings at 0 Degrees Angle of Attack, Thin Boundary Layer, Stability Wind Tunnel.

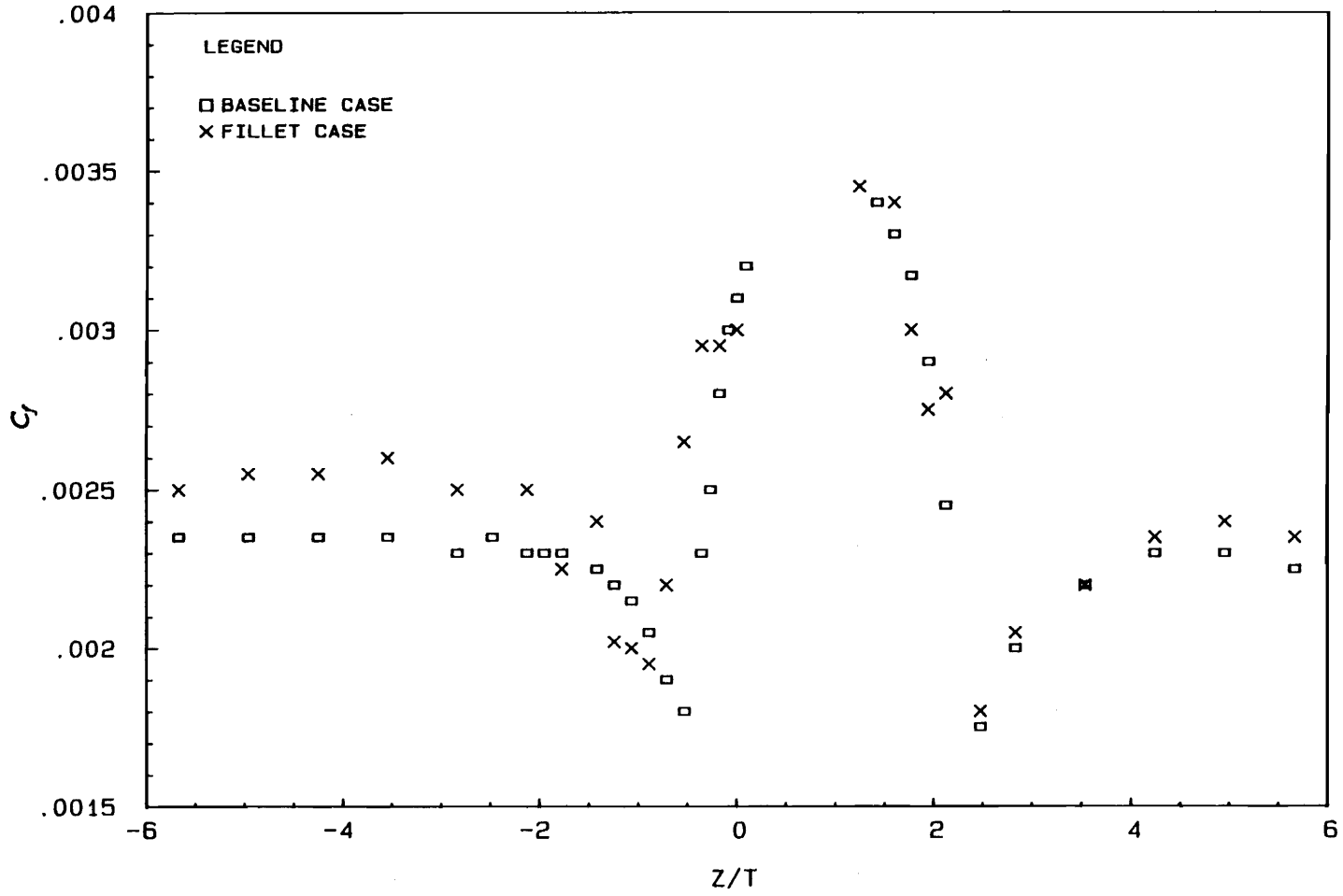

Figure 69. Spanwise C_f Distribution at X/C = 3, Wings at 6 Degrees Angle of Attack, Thin Boundary Layer, Stability Wind Tunnel.

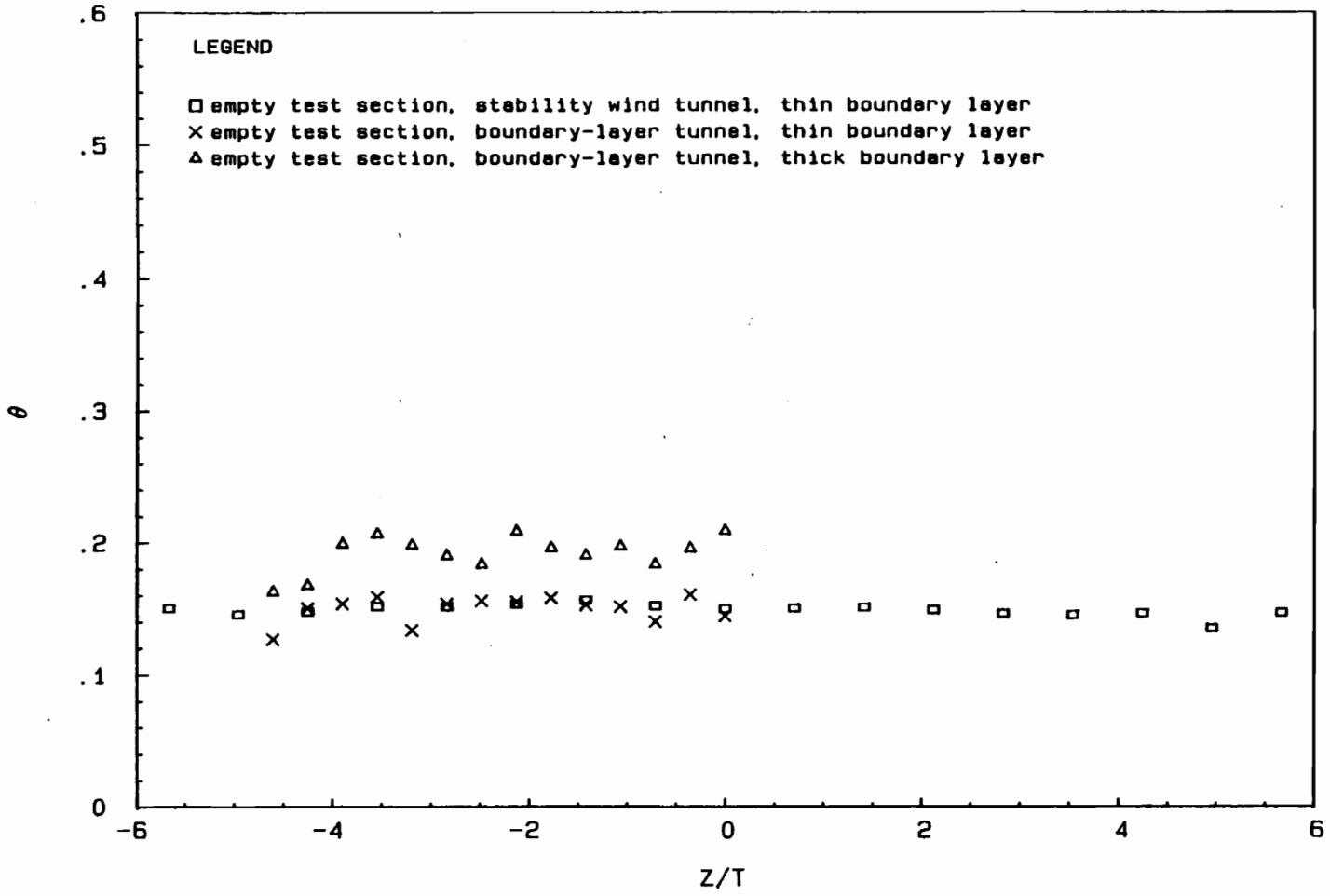

Figure 70. Spanwise Distribution of θ at X/C=3, Empty Test Section, Units are Inches.

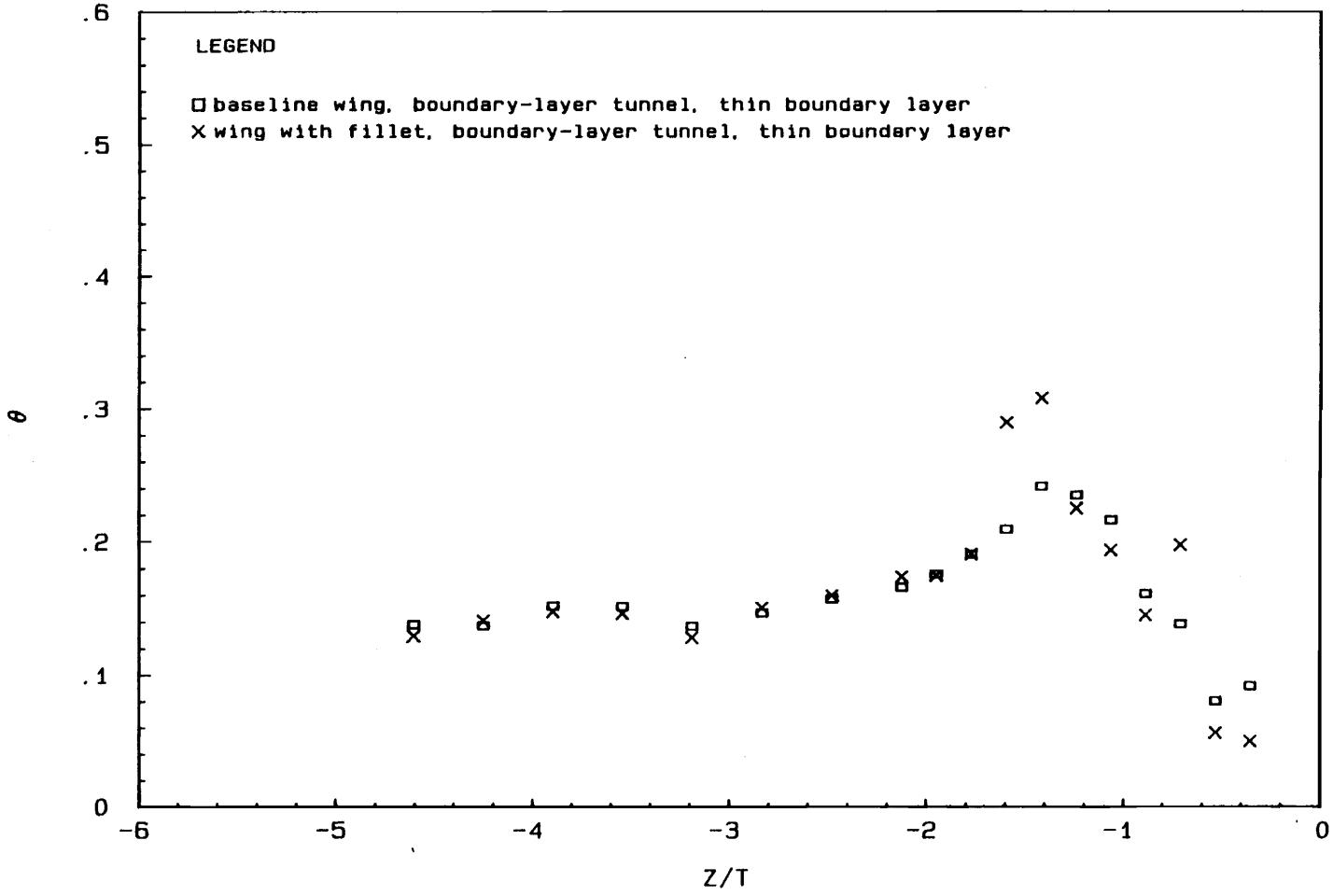

Figure 71. Spanwise Distribution of θ at X/C=3, Wings at 0 Degrees Angle of Attack, Thin Boundary Layer, Boundary-Layer Tunnel, Units are Inches.

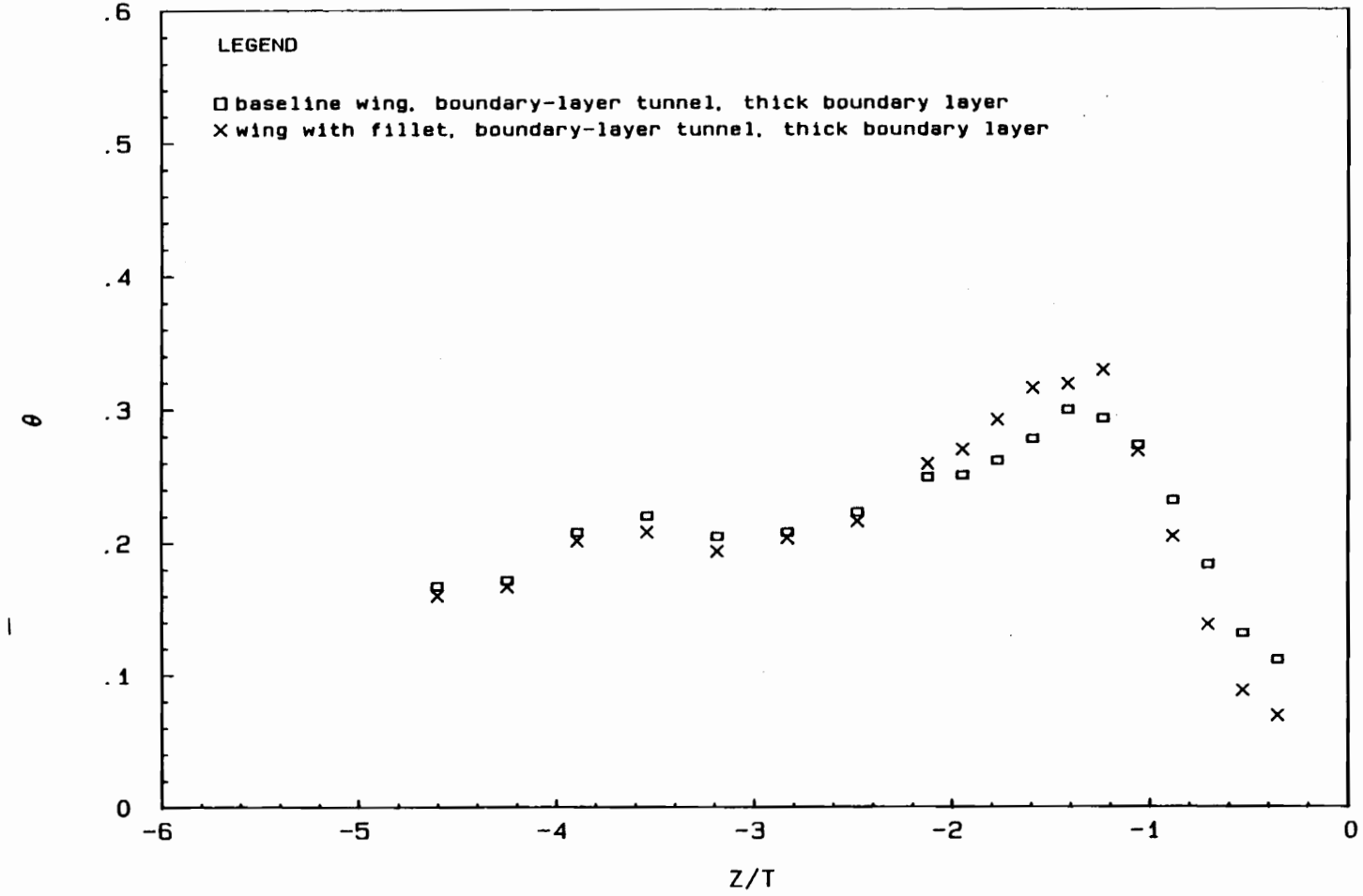

Figure 72. Spanwise Distribution of θ at X/C=3, Wings at 0 Degrees Angle of Attack, Thick Boundary Layer, Boundary-Layer Tunnel, Units are Inches.

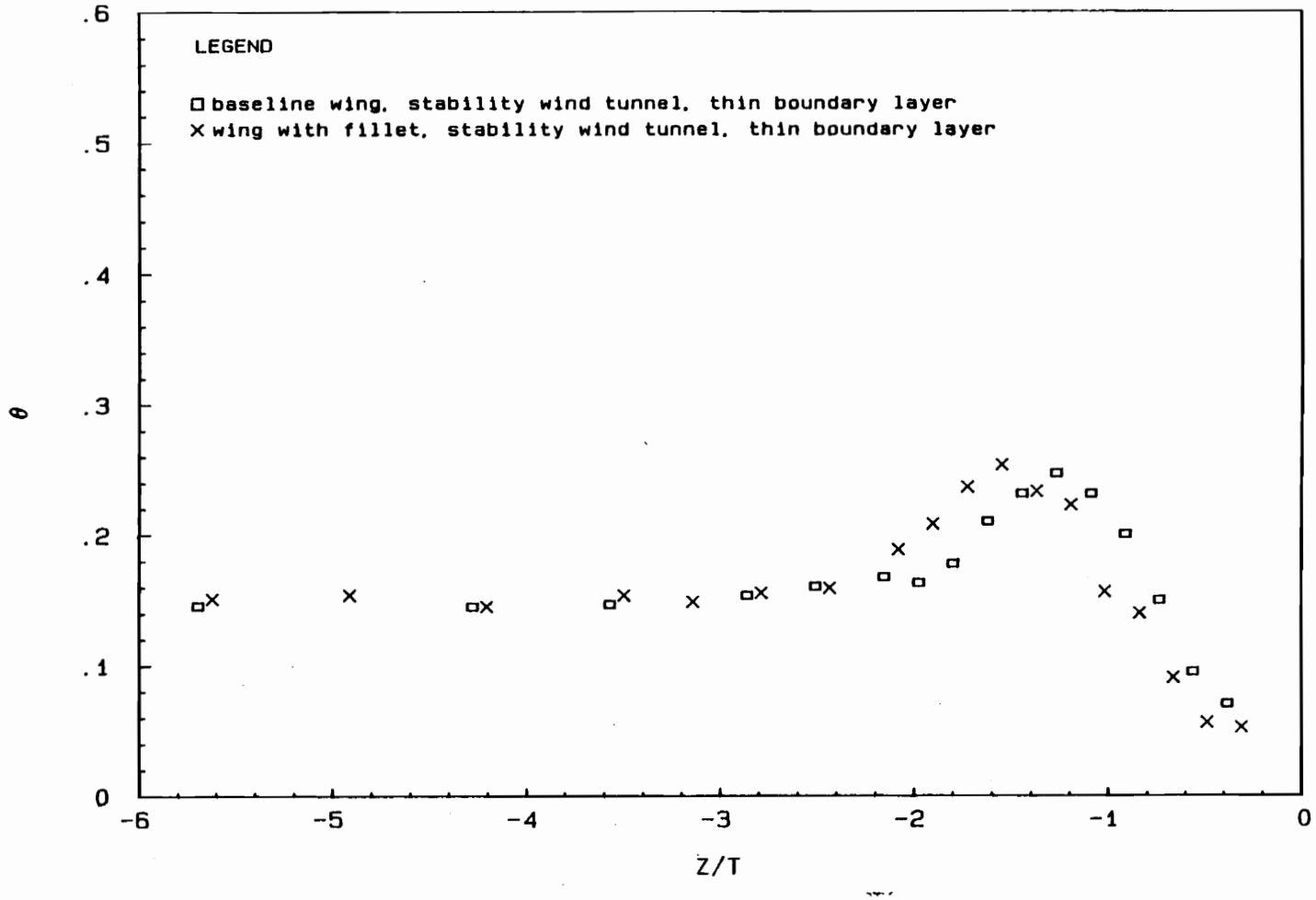

Figure 73. Spanwise Distribution of θ at X/C=3, Wings at 0 Degrees Angle of Attack, Thin Boundary Layer, Stability Wind Tunnel, Units are Inches.

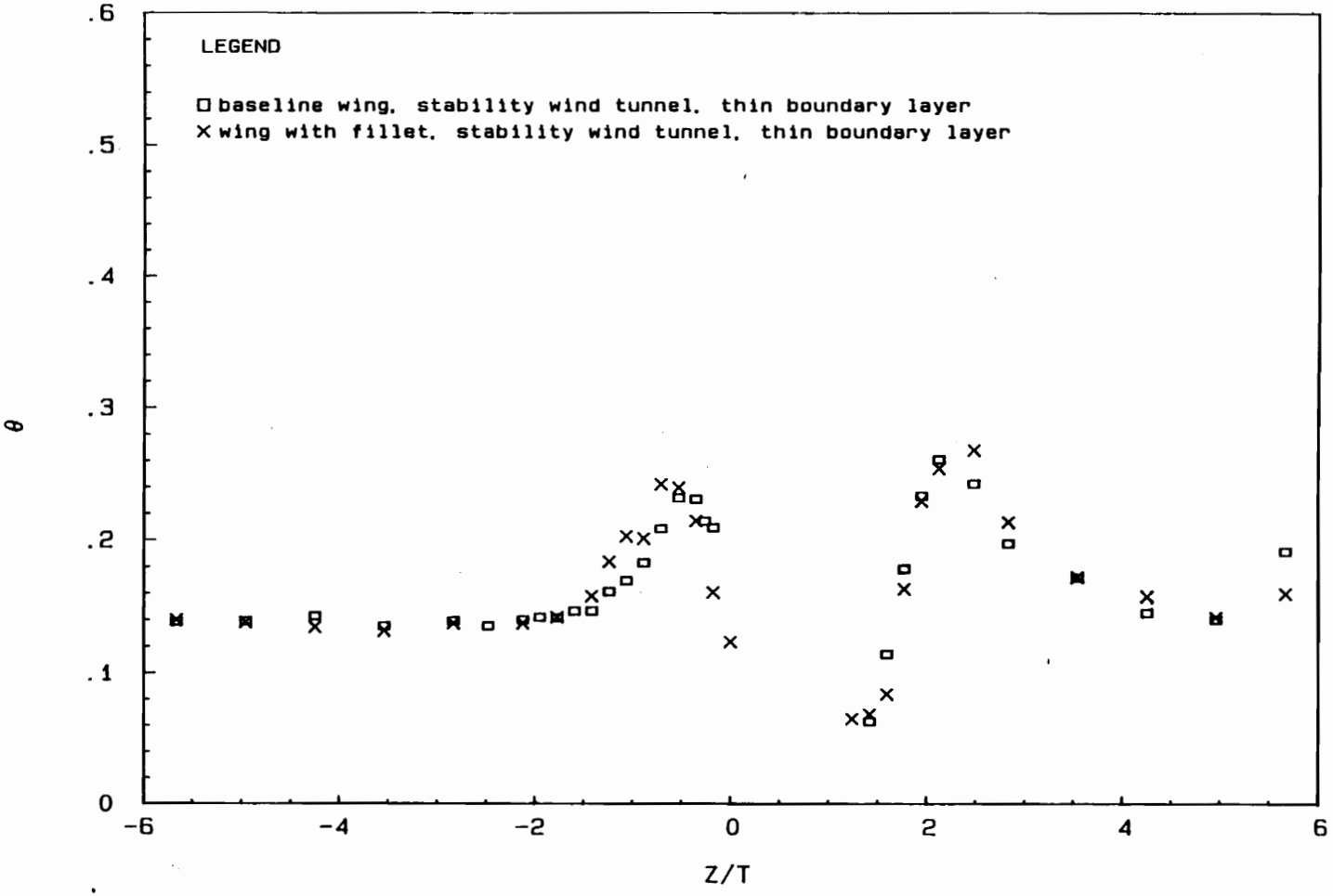

Figure 74. Spanwise Distribution of θ at X/C=3, Wings at 6 Degrees Angle of Attack, Thin Boundary Layer, Stability Wind Tunnel, Units are Inches.

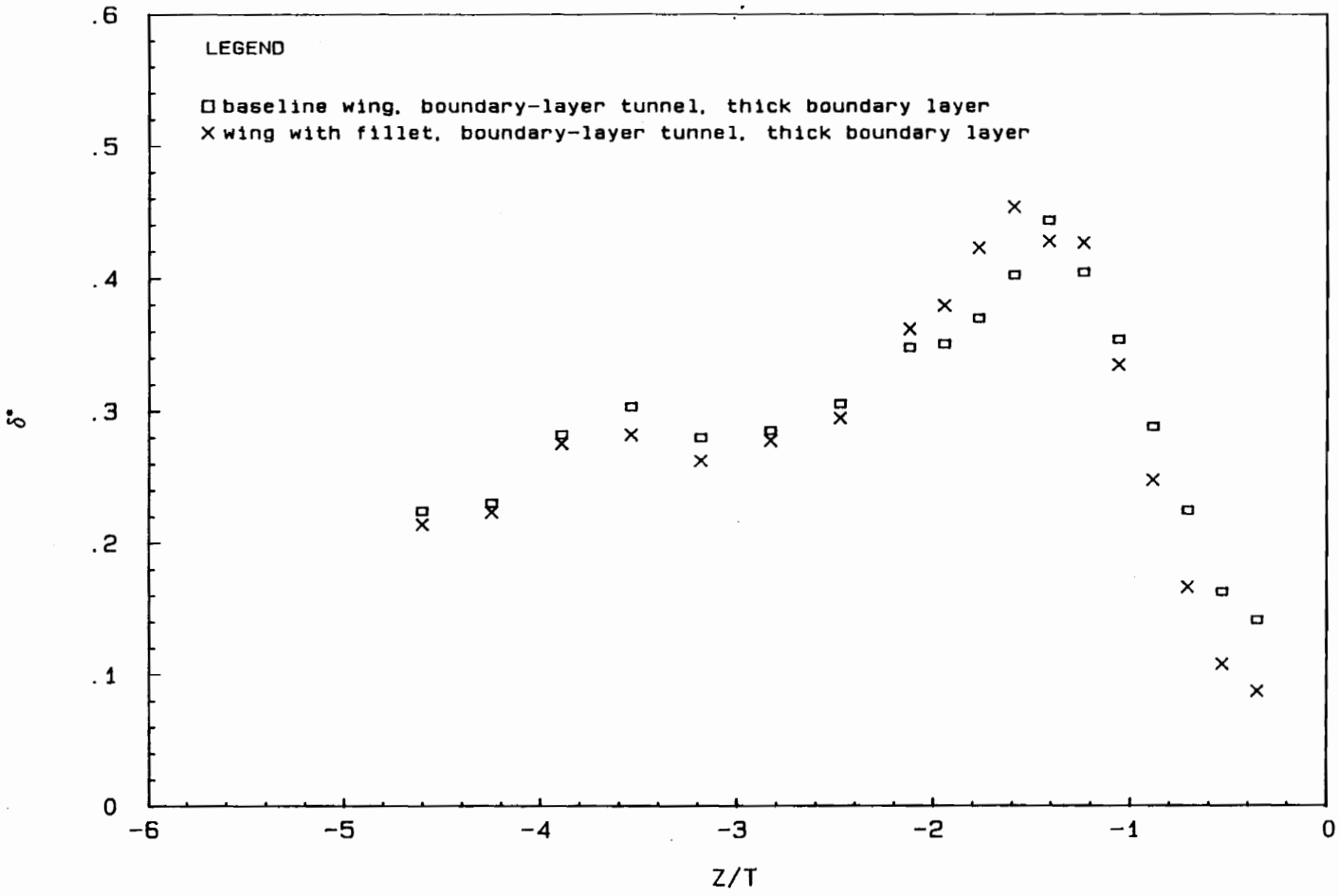

Figure 75. Spanwise Distribution of δ^* at X/C = 3, Empty Test Section, Units are Inches.

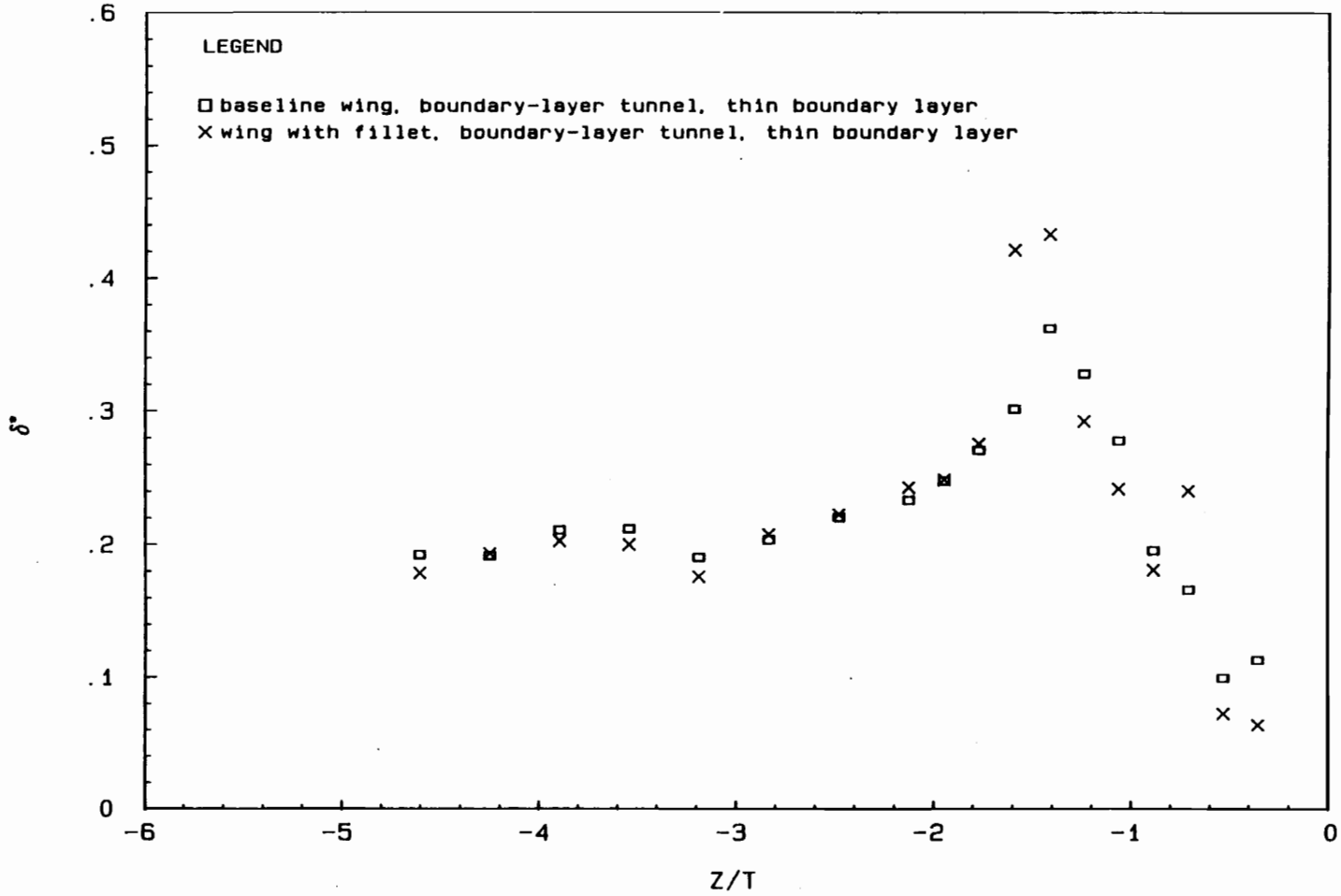

Figure 76. Spanwise Distribution of δ^* at X/C=3, Wings at 0 Degrees Angle of Attack, Thin Boundary Layer, Boundary-Layer Tunnel, Units are Inches.

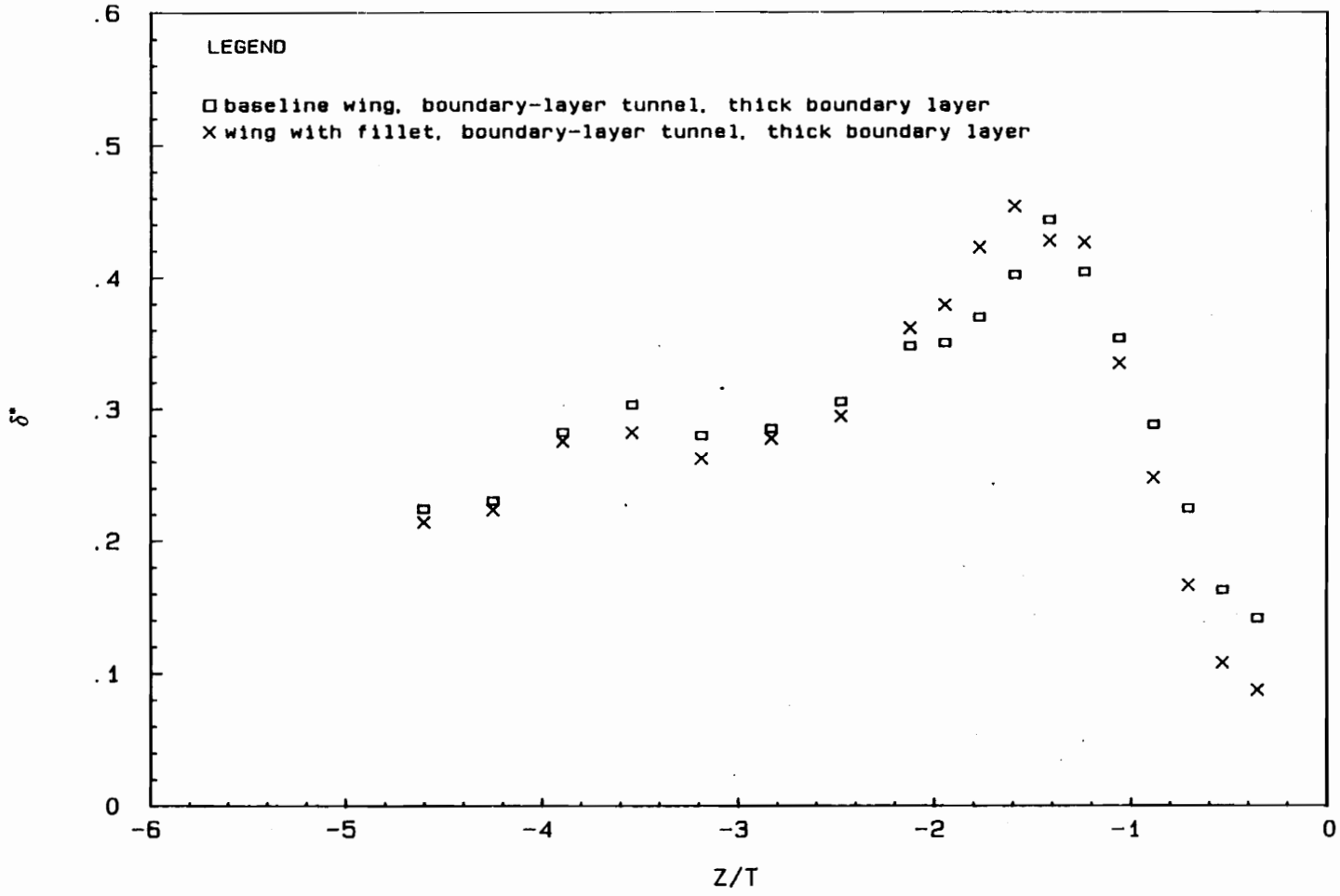

Figure 77. Spanwise Distribution of δ^* at X/C = 3, Wings at 0 Degrees Angle of Attack, Thick Boundary Layer, Boundary-Layer Tunnel, Units are Inches.

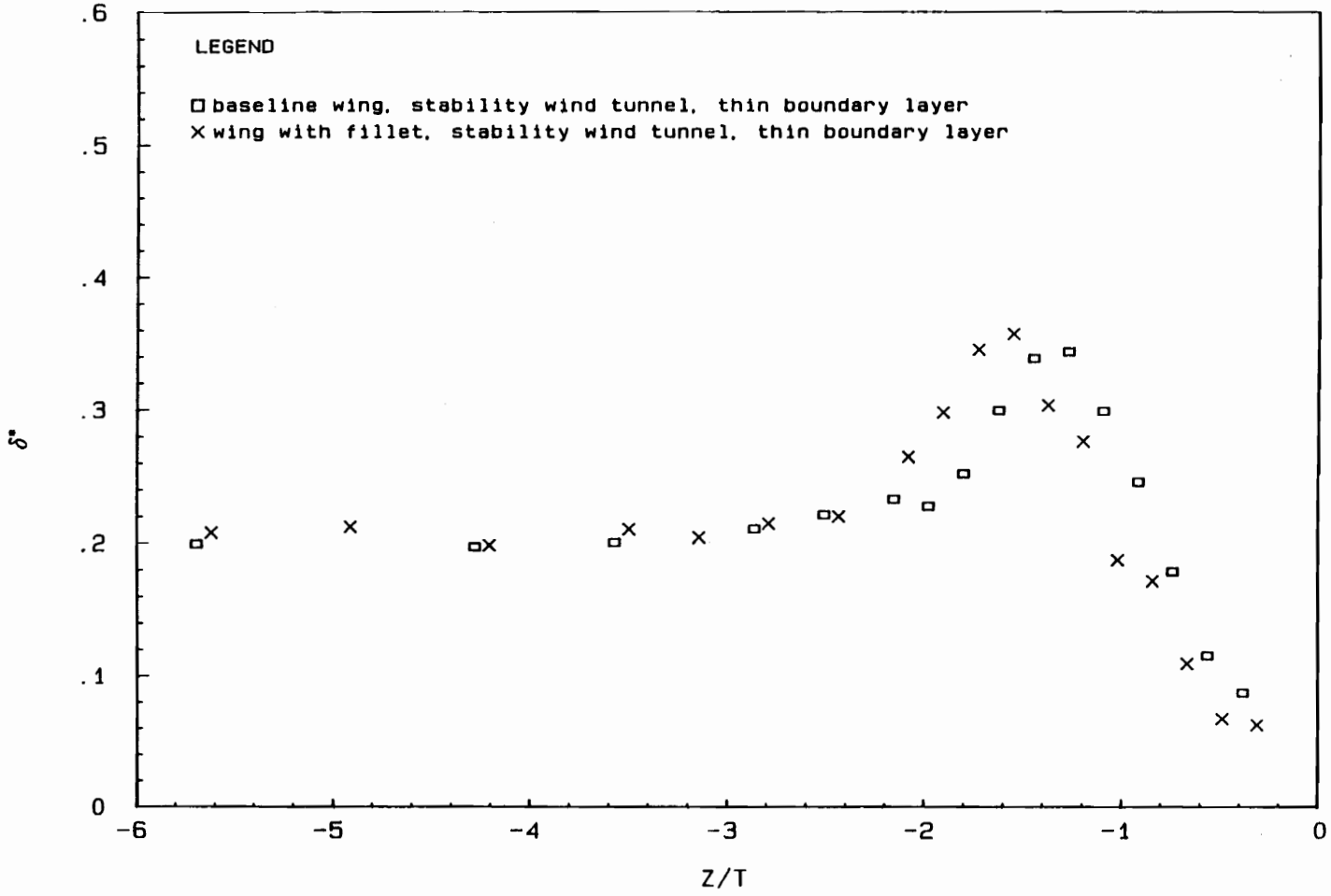

Figure 78. Spanwise Distribution of δ^* at X/C=3, Wings at 0 Degrees Angle of Attack, Thin Boundary Layer, Stability Wind Tunnel, Units are Inches.

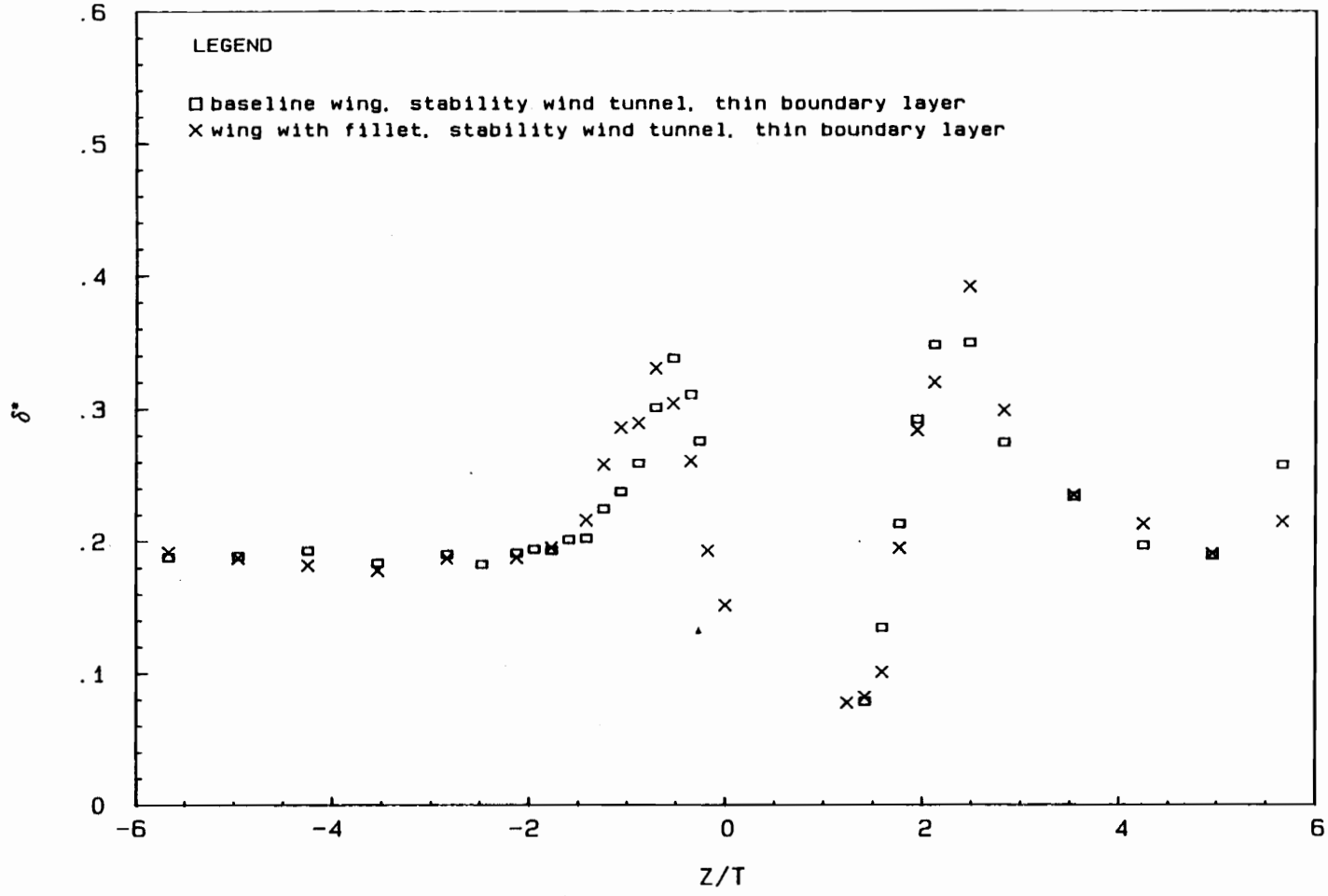

Figure 79. Spanwise Distribution of δ^* at X/C=3, Wings at 6 Degrees Angle of Attack, Thin Boundary Layer, Stability Wind Tunnel, Units are Inches.

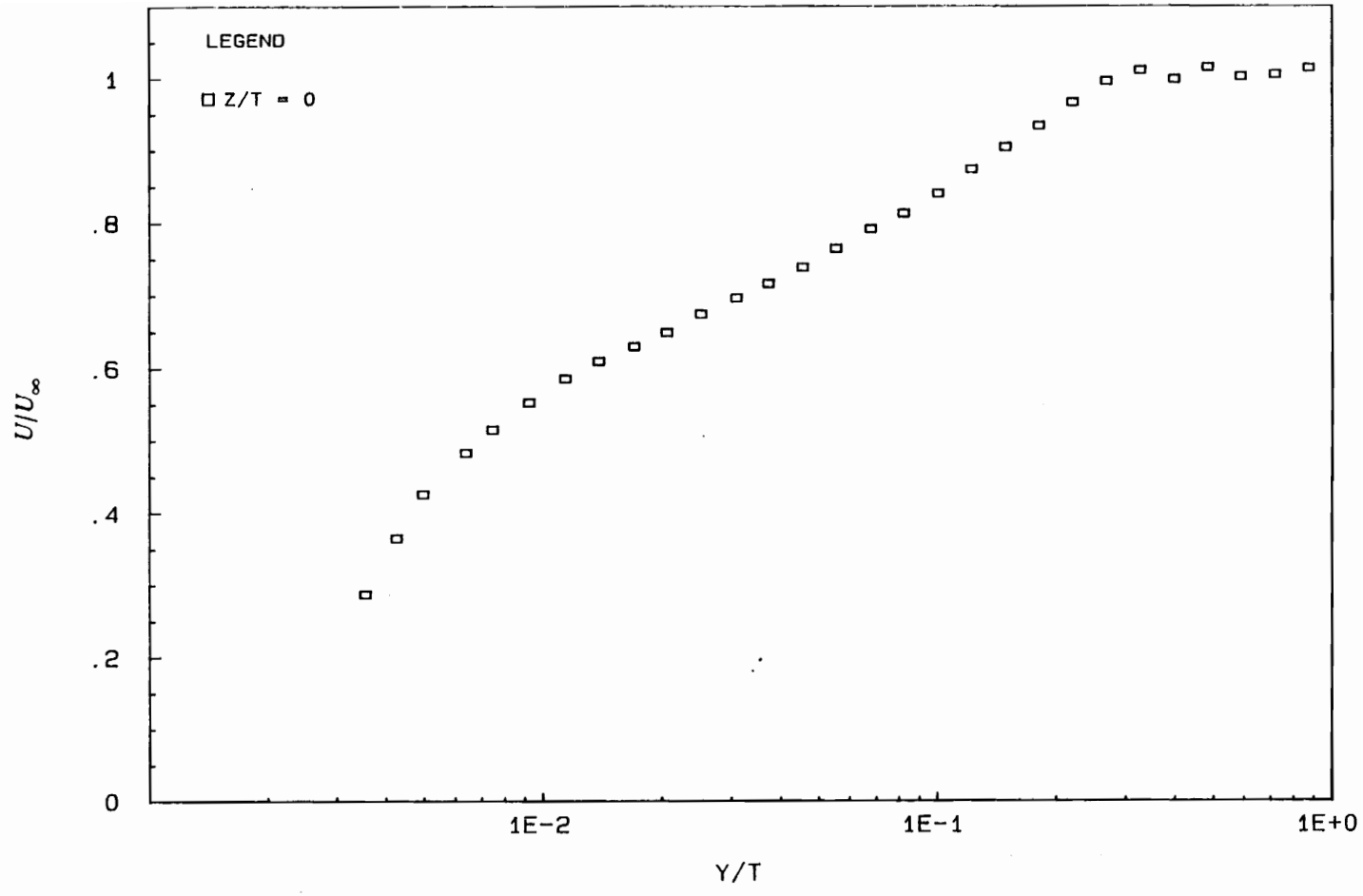

Figure 80. U/U_∞ Profile at X/T=-18.2, Thick Boundary Layer, Boundary-Layer Tunnel.

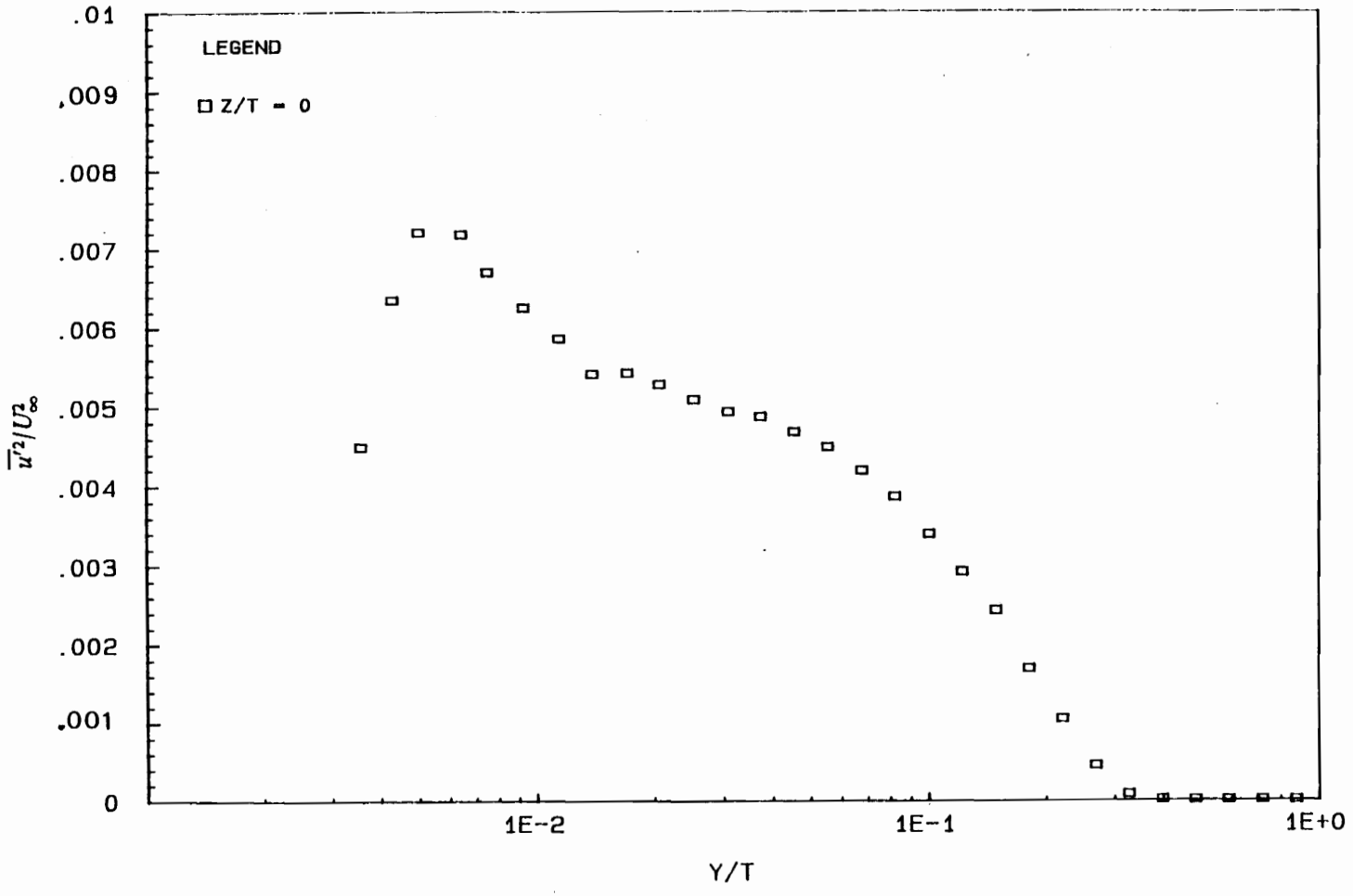

Figure 81. $\overline{u'^2}/U_\infty^2$ Profile at X/T=-18.2, Thick Boundary Layer, Boundary-Layer Tunnel.

Tables

Table 1. Uncertainties of Measured Data.

Mean Velocity	$U \pm 1.8$ percent.
Mean Square of velocity fluctuation	$\overline{u'^2} \pm 6$ percent.
Probe position in Boundary-Layer Tunnel	$y \pm 1.0 \times 10^{-1}$ mm.
	$z \pm 7.0 \times 10^{-1}$ mm.
Probe position in Stability Wind Tunnel	$y \pm 3.0 \times 10^{-1}$ mm.
	$z \pm 1.1$ mm.
Pressure Coefficient	$C_p \pm .8$ percent.
Momentum Thickness	$\theta \pm$ 10percent.
Displacement Thickness	$\delta^* \pm$ 10percent.
Drag coefficient	$C_d \pm$ 5percent.
Entrainment of Free-Stream Fluid	$\dot{m}_e \pm$ 5percent.

Table 2. Momentum Deficit in the Spanwise Plane at X/C = 3

Stability Wind Tunnel	
empty test section	0.0667571
baseline wing at zero degrees of attack	0.0734361
wing with fillet at zero degrees angle of attack	0.0771304
baseline wing at six degrees angle of attack	0.0814061
wing with fillet at six degrees angle of attack	0.0799667
Boundary-Layer Tunnel, Thin Boundary Layer	
empty test section	0.0674351
baseline wing at zero degrees angle of attack	0.0713127
wing with fillet at zero degrees angle of attack	0.0722429
Boundary-Layer Tunnel, Thick Boundary Layer	
empty test section	0.086427
baseline wing at zero degrees angle of attack	0.097238
wing with fillet at zero degrees angle of attack	0.0931089

Table 3. Values for the Drag Coefficient

Stability Wind Tunnel	
empty test section	0.0429591
baseline wing at zero degrees of attack	0.0496381
wing with fillet at zero degrees angle of attack	0.0533324
baseline wing at six degrees angle of attack	0.0576081
wing with fillet at six degrees angle of attack	0.0561687
Boundary-Layer Tunnel, Thin Boundary Layer	
empty test section	0.0360363
baseline wing at zero degrees angle of attack	0.0471601
wing with fillet at zero degrees angle of attack	0.0462299
Boundary-Layer Tunnel, Thick Boundary Layer	
empty test section	0.050009
baseline wing at zero degrees angle of attack	0.0566909
wing with fillet at zero degrees angle of attack	0.06082

Table 4. Non-Dimensionalized Volumetric Flow Rate of Turbulent Fluid at X/C = 3

Stability Wind Tunnel	
empty test section	0.1417141
baseline wing at zero degrees of attack	0.2172439
wing with fillet at zero degrees angle of attack	0.2272439
baseline wing at six degrees angle of attack	0.2383615
wing with fillet at six degrees angle of attack	0.2393798
Boundary-Layer Tunnel, Thin Boundary Layer	
empty test section	0.1437396
baseline wing at zero degrees angle of attack	0.1663964
wing with fillet at zero degrees angle of attack	0.173761
Boundary-Layer Tunnel, Thick Boundary Layer	
empty test section	0.1974924
baseline wing at zero degrees angle of attack	0.2121764
wing with fillet at zero degrees angle of attack	0.2245166

Table 5. Non-Dimensionalized Entrainment Rate of Free-Stream Fluid

Stability Wind Tunnel	
empty test section	0.092636
baseline wing at zero degrees of attack	0.1681658
wing with fillet at zero degrees angle of attack	0.178883
baseline wing at six degrees angle of attack	0.1892834
wing with fillet at six degrees angle of attack	0.1903017
Boundary-Layer Tunnel, Thin Boundary Layer	
empty test section	0.0999085
baseline wing at zero degrees angle of attack	0.1225653
wing with fillet at zero degrees angle of attack	0.1299299
Boundary-Layer Tunnel, Thick Boundary Layer	
empty test section	0.1078424
baseline wing at zero degrees angle of attack	0.1225264
wing with fillet at zero degrees angle of attack	0.1348666

The author was born on August 28, 1965 in Queens, New York. He attended Sanford H. Calhoun High School in Merrick, New York and graduated in 1983. He earned his B.S. degree in Aeronautical Engineering from Virginia Polytechnic Institute and State University, Blacksburg, Virginia in June 1987. Upon graduation, he went directly into the Graduate School at VPI&SU. He is currently a member of AIAA.

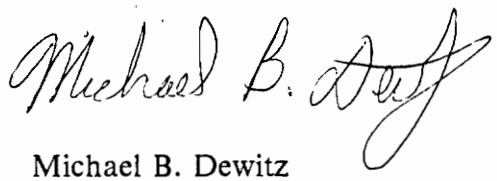

Michael B. Dewitz